Dimers, Trimers and their Superpositions in a Bose-Fermi Mixture

by

Alexander Chuang

Submitted to the Department of Physics
in partial fulfillment of the requirements for the degree of

DOCTOR OF PHILOSOPHY

at the

MASSACHUSETTS INSTITUTE OF TECHNOLOGY

September 2024

Authored by: Alexander Chuang
B.S. Engineering Physics, UC Berkeley, 2017
September 3, 2024

Certified by: Martin Zwierlein
Thomas A. Frank (1977) Professor of Physics, Thesis Supervisor

Accepted by: Lindley Winslow
Professor of Physics
Associate Department Head

Dimers, Trimers and their Superpositions in a Bose-Fermi Mixture

by

Alexander Chuang

Submitted to the Department of Physics
on September 3, 2024 in partial fulfillment of the requirements for the degree of

DOCTOR OF PHILOSOPHY

ABSTRACT

This thesis describes experiments on few- and many-body bound states in a Bose-Fermi mixture of ultracold ^{23}Na and ^{40}K atoms. We examine the formation of dimers and trimers in a balanced, thermal mixture and their evolution into strongly interacting Bose polarons with hybridized dimer and trimer character when we instead immerse an impurity concentration of K into a dense quantum bath of Na.

We report a novel direct observation of a heteronuclear halo trimer, consisting of two lighter Na atoms and one heavier K atom, alongside the familiar NaK Feshbach dimer, using radiofrequency (rf) spectroscopy. We find that in proximity to a Feshbach resonance, the trimer feature closely follows the dimer resonance across an order-of-magnitude variation in binding energy. We show that the measured binding energies are consistent with our theoretical model of the trimer as having the structure of a Feshbach dimer weakly bound to one additional boson.

We then study the fate of impurities interacting with a bosonic quantum bath, the paradigmatic Bose polaron scenario. By preparing an initial attractive polaron state, we probe previously inaccessible, highly-correlated Bose polaron states, again on the repulsive side of the Feshbach resonance. Deep within the condensate, the rf spectra no longer exhibit discrete dimer and trimer features as before, instead dominated by a single broad feature. We attribute this to the impurity-boson coupling becoming stronger than the dimer-trimer energy splitting, leading to hybridization of dimer and trimer states and, consequently, an effective level repulsion consistent with the spectra we observe. This experiment demonstrates the remarkable interplay between polaron physics and bound-state formation in a quantum environment.

Thesis supervisor: Martin Zwierlein
Title: Thomas A. Frank (1977) Professor of Physics

Acknowledgments

I would have never completed this journey without the support of the numerous wonderful people around me over the years. My gratitude cannot be fully expressed in words, but I will try here.

My advisor Martin has been a central part of my PhD. Martin sets by example an impeccable standard for scientific work, and his cheerfulness, drive, curiosity, and creativity know no bounds. Thank you for providing the opportunity for me to work on the Fermi1 team; it has been a formative experience that pushed me far beyond the previous boundaries of my capabilities.

When I first joined Fermi1, Zoe, Yiqi, Elisa, and Carsten welcomed me in. Zoe whizzed around in the lab, operating the machine with the dexterity of a master pianist, but she could also do theory and simulations at the drop of a hat. I admire her assertiveness and perseverance on tackling any challenge. Elisa and I worked together on what formed the ECDL section of this thesis, and if I am to be fair, a great deal of it was her showing me basic hands-on knowledge about optics. During my many years of overlap with Yiqi, it seemed like we always had something to laugh about. When things in the lab did not work as advertised, he showed the MIT spirit of treating debugging like a game, telling me that if I was stuck, I should just "play with it" some more. And of course, I must thank Yiqi and Carsten for laying the groundwork of exploratory rf measurements that eventually was refined and evolved into the scientific content of my thesis. Soon after I joined, Eric joined as well, and I often wish that we had been co-workers for longer. Eric is not afraid of getting his hands dirty to get the lab into a sparkling state, whether figuratively or literally, and he is a fantastic narrative writer (look no further than certain parts of the Fermi1 lab book).

Carsten has been a fantastic mentor. I remember vividly the lab tour during the MIT open house visit, when I first met Carsten. After briefly asking me about my previous research, he talked my ear off about how exciting Fermi1 would be (even though at that time I could not understand nor appreciate half the content of our conversation). I like to think that his loquaciousness and my lack thereof were wonderfully complementary in the lab, and despite this contrast, I always felt heard when I did have something to say. When it came to over-killing technical projects, Carsten taught me a great deal, and that helped broaden my perspective on what it meant to be a experimental physicist.

Huan and Yiming are currently my colleagues in Fermi1. I am quite lucky that I frequently have the feeling that they are both more capable than I am, despite my seniority! As Martin says, they are "wizards," able to quickly learn and execute whatever the lab demands of them. Huan has an unshakeable confidence that things in the lab "must work," but in my experience he is missing the conditional "when Huan is around." Yiming approaches his

projects with a level of professionalism that cannot be rivaled, and any attentive guest on a lab tour can easily spot his work. With this combination, I am sure they will fuel the future successes of Fermi1. I am humbled by the experience of mentoring several UROP students as well. It is my great honor to see both Xiaoyang and Derek mature as growing young physicists.

While I owe many of my successes to the Fermi1 team, I must also say that without them, I would never have overcome the times of adversity and struggle. I will never forget when Carsten and Yiqi led the Herculean repairs of the K oven chamber, when Eric and I acquired new expertise on handling alkali metal, when Yiming and I had to revive the machine after various shutdowns and repairs, and the grit of Yiming and Huan to make sure the show went on when I went on leave.

I am glad to have the chance to know many of my lab mates outside the lab as well. I will look back fondly at playing video games with Eric, Yiming, Yiqi, and Botond at the parties hosted by Carsten, even if some of them had to be virtual due to the pandemic. Huan is an absolute beast on the chessboard, and Yiming is a musical genius (especially in the instruments of arcade taiko drums and fiber phase noise analyzer). It's too bad that the lab AC is so loud now that we can no longer listen to "Rachmaninoff plays Rachmaninoff" on the lab loudspeaker without destroying our eardrums.

All the members of the Zwierlein and Fletcher groups are an absolute pleasure to hang out and chat with. The culture of regularly going to lunch together is a gem, and I hope it carries on well into the future. As senior students to me, Biswaroop and Cedric shared invaluable advice only attainable through life experience. Botond's ability to deliver ZGS emails, speaker introductions, and hot-takes are supremely entertaining, and somehow he always manages to drop by Fermi1 as I need a break. But on a more serious note, I am astounded by how fast Botond can formulate thought-provoking questions and engage with the speaker in scientific presentations. And Jared is the embodiment of having a humble, laid-back demeanor, while still achieving incredible things in the lab, that I think is just wonderful to have around in a high-intensity environment like the CUA.

Arthur Christianen did all the theory calculations supporting the scientific projects in this thesis, and I would have struggled greatly to make sense of what we measured without his insights. He is one of those people that just knows how to get things done, and our back-and-forth was always stimulating and motivating as we discussed the nitty-gritty details to see if theory and experiment matched.

I consider myself quite fortunate to be riding the wave of an era in the CUA where the interest in building robust experiments and automating their operation is high. I am indebted to Carsten for kickstarting the process of migrating the control stack to labscript. Hearing him talk about how he could remotely run his experiments in Bonn at near 100% uptime on the weekend was incredibly inspiring, given the wayward nature of the Fermi1 apparatus. He convinced me that it was not just some dream and trusted me to make it happen. A big thanks goes to Matt and Carter as well for answering my myriad of silly questions as I tried to figure out how to make it work. And to all the active folks in the labscript community around the world, I am so grateful this project gained a critical mass and helps to foster a collaborative spirit among the AMO community.

There were times when it felt like there were insurmountable obstacles in the PhD journey, and I am indebted to those who were willing to listen. Martin, I appreciate when you allowed

me the time and space to take a step back to get myself back on track. Yiming, thanks for lending an ear when I felt overwhelmed during the transitional period of becoming the senior student. Cathy Modica and Gaurav Jashnani gave me so much wonderful advice to navigate through the difficult times. And Mihir, Carsten, David, and Denis, thank you for giving me an opportunity to contribute to a budding organization and reinvigorate my scientific spirit.

I have a few folks to thank for helping me to take my mind off physics sometimes, in particular Josh for his spontaneous calls when he's in town, Elma for helping me play the tourist on her visits and indulging with me in silly YouTube videos when I'm home, and certainly Jinggang for helping me not feel so out of place as a Golden State fan in Boston. Jinggang, thank you for also getting me out of my comfort zone by signing up for 6.7900 with me.

There have been a few key influences in my pre-MIT education that helped me fuel my excitement for physics. I appreciate Hartmut's generosity and for making undergraduates a key part of his lab. His insistence on mentorship, both giving and receiving, being a key component of an education set the stage for a welcoming environment. Crystal was the first person who introduced me to the basic concepts of atomic physics, and she encouraged me to learn the basic ideas and present them at poster sessions with confidence. Erik, with a can-do attitude, led the construction of a new experiment and showed me that instead of searching for where to cast blame when things did not work as expected, to direct that energy towards blazing your own trail until they work. My AP Physics teacher Mr. Shapiro engaged students directly with memorable demos, and they left a lasting impression that the "awesomeness" of physics is best experienced not on paper but through tangible experiences.

Coming from a family that taught me to deeply value education has allowed me to push through the tough times. This has served as a cornerstone in my life, from my paternal grandparents in their retirement teaching me the basics of arithmetic, to my mother working tirelessly so that I could focus on studying without wanting for anything.

My father's undying passion for science inspired me to become a scientist. Working in his lab taught me that good research demands mastery of both the hands-on technical skills and sound experimental design. Even as our paths diverged, he reminded me to trust the pillars of clear thinking and dedicated effort, not just in the lab, but in life, no matter the many twists and turns.

Sam is the brightest source of light in my life[1]. As lonely and isolating the journey felt sometimes, I knew that I could always count on Sam to be a kind and caring partner. I am incredibly blessed by how willingly Sam has sacrificed for me, especially when it was debatable if I knew what I was doing. She has had the enduring patience to hear me talk about so much of this thesis work that I think she deserves some kind of an honorary degree. Her intelligence and charm have no match, and her laughter radiates joy into my life on the darkest days.

[1] I believe that is one of the highest compliments you can give as an AMO physicist.

Contents

List of Figures

List of Tables

Chapter 1

Introduction

The experiments in the field of atomic, molecular, and optical physics are a wonderful playground to explore the quantum mechanics of single, few and many-body systems. In such experiments, we have the ability to prepare extremely clean and ultracold atomic and molecular samples and to exquisitely manipulate and probe both their internal and external states as well as tune their interactions. The development of such experimental techniques can be relevant to the general physics community beyond those working in the AMO subfield. Because oftentimes we can draw parallels to other physical systems, our experiments can inform the understanding of phenomena that might otherwise be intractable to current theoretical, computational and experimental methods. More concretely, the atoms or molecules in our experiments can be, for example, be made to behave similarly to the electrons in a solid or the nucleons in an atomic nucleus. This is the idea of *quantum simulation* as first originated by Feynman in 1982[1] and continues to be a growing discipline today [2]. We must also point out, however, that these techniques have also enabled amazing applications and science in their own right, with the world's finest clocks [3], sensors [4], prototypes of quantum computers[5], [6], and fundamental physics probes [7] being fundamentally AMO experiments at heart.

A great deal of the pioneering work in this field has been performed with atomic systems, and molecular systems represent a new frontier with new capabilities but also more challenges. Unlike the relatively simple structure of atoms, molecules have ro-vibrational degrees of freedom to tame as well, which adds to the scale and complexity of the required experimental apparatus. This is apparent upon seeing the experimental apparatus described in this thesis (a.k.a. Fermi1)[1], which follows the bi-alkali STIRAP approach to creating ultracold diatomic Na-K molecules, inspired by the pioneering experiments at JILA [8], [9]. This is not the only method of creating samples of cold molecules, with the complementary approach of buffer gas and laser cooling of carefully chosen molecular species also proving to be quite successful[10], [11]. Despite the required technical complexity of molecule experiments, many are coming online around the world and they hold great promise as the next generation of experiments for sensing, timekeeping, fundamental physics, quantum information science, and quantum simulation, as well[12], [13]. Quantum simulation with molecules is one of the long-term goals of the Fermi1 experiment, so we discuss in further detail below

[1]We often joke that Fermi1 is the result of gluing together two atomic physics experiments and adding on a pair of (almost) state-of-the-art narrow-linewidth lasers.

the physics we hope to become accessible in such a system.

1.1 Ultracold molecules as an emerging platform for quantum simulation

Ultracold molecules are an attractive platform for quantum simulation [14]. The large internal state space of ro-vibrational degrees of freedom offers synthetic dimensions to explore [15], and even more tantalizing is, for the case of *dipolar* molecules (e.g., heteronuclear bialkalis, such as our favorite NaK), controllable long-range and anisotropic interactions. The form of interactions between two molecules (on the z-axis) with dipoles $\mathbf{d}_i$ and separation z is given by

$$V \propto \frac{1}{z^3}(\mathbf{d}_1 \cdot \mathbf{d}_2 - d_{1z}d_{2z}). \tag{1.1}$$

While there are certainly other experimental platforms offering some degree of overlap with these traits, e.g., those incorporating Rydberg atoms [16] or highly magnetic atoms such as erbium [17], dipolar molecules offer a reasonable compromise between strength of interactions[2] and lifetime of the rotational excitations[3] giving rise to the dipole moment underlying said interactions.

We can expect to study a wide range of rich physics using ultracold molecules both trapped in the bulk or in optical lattices. In the bulk, it has been predicted, for example, that the collective motion and thermalization of the ensemble crosses over from a so-called weltering motion to a hydrodynamic one [20]. In a lattice, for example, the effects of the itinerancy and dipolar interactions on spin dynamics has been explored in [21]. With the addition of high-resolution imaging, correlations at the single-particle level arising from Hanbury Brown-Twiss effect [22] and an effective XY spin-exchange Hamiltonian [23] have been observed as well.

As improvements in experimental techniques continue to drive us deeper into quantum degeneracy, we can hope to study previously unrealized physical models. In fermionic systems, it is predicted that topological superfluidity can be observed in the bulk [24], up to temperatures as high as $T/T_F \approx 0.14$ for NaK molecules dressed by microwaves [25]. Meanwhile, in a lattice, one can perform quantum simulations of the Fermi-Hubbard model, which is of great interest to the condensed matter community, as it is speculated to support exotic phases of matter such as high-temperature superconductivity [26]. Furthermore, with dipolar interactions, one can expand such studies to the extended Fermi-Hubbard model, which is predicted to host novel phases such as those with "ultralong-range" order [18].

1.2 Experimental motivations: a backstory

Now that we have motivated the pursuit of realizing a quantum degenerate Fermi gas of dipolar molecules in experiment, we must understand what are the current roadblocks. To

[2] up to ∼10 of kHz in a 532 nm lattice[18]

[3] for example, of several seconds in the excited $J = 1$ rotational state of NaK [19]

do so, we will review the progress of several other bi-alkali experiments in other groups and the status of the Fermi1 apparatus as well.

The achievement of high phase-space densities of molecules in this class of experiments is largely due to the maturity of techniques such as laser cooling and evaporative and sympathetic cooling of alkali atoms, to prepare low-entropy dual species atomic mixtures, where double degeneracies of 60% condensate fraction for the bosons and $T/T_F = 0.2$ for the fermions are routinely possible [27]. The subsequent inefficient steps of associating weakly or non-interacting atoms into weakly-bound Feshbach molecules and coherently transferring them into the ground state through a Raman process is where a great deal of the damage occurs, bringing the sample back out of degeneracy[4]. This can be understood intuitively in the sense that inefficiencies are essentially uncontrolled losses in the system that increase entropy, poking holes in the resulting Fermi sea. In the Fermi1 experiment, the historical records for conversion efficiency of associating atoms into Feshbach molecules has been $\sim$ 10% [28] (relative to the minority species) and the single-pass STIRAP efficiency 75% [29]. This is shown schematically in figure 1.1b.

We can realistically expect to improve the STIRAP efficiency in Fermi1 with reasonable technical upgrades. Other experiments have shown STIRAP efficiencies exceeding 90%, for example the Rb-Cs experiment at Durham with an efficiency of $> 98\%$ [30]. Both technical improvements on the laser sources to reduce phase noise[30] and careful selection of the intermediate excited state [31] can make a significant impact. The Na-K experiment in Munich has shown that is possible to achieve efficiencies of $> 80\%$ using the combination of 804 and 567 nm transitions we are currently using [32], and my colleague Yiming Zhang is currently implementing and testing a new laser system[5] towards this pursuit.

The low conversion efficiency in the Feshbach association step is indeed a major bottleneck of our experiment to achieving degeneracy, conceptually[6]. We will primarily focus our discussion on performing this procedure in a bulk trap, since this is most relevant given the capabilities of the Fermi1 apparatus. The method that we currently use is rf association, as first demonstrated in our experiment in [33], where we apply an rf pulse that resonantly connects scattering states of atoms into the Feshbach dimer state. The limitation of this procedure are two-fold. First, the atoms must be well overlapped in (real) space, and mismatches in the density profile mean that atoms will have trouble "finding a partner" of the opposite species to form a molecule. The necessity of working with a Bose-Fermi mixture, since we want to study fermionic molecules, means that even their inherent quantum statistics can cause the spatial profiles to become mismatched as the atomic mixture is cooled to quantum degeneracy[7]. Second, the rf pulse applied consists of a single frequency and therefore can only address an even smaller subset of atoms with relative momentum given by the resonance condition, imposing a condition in momentum space as well. To deal with this problem of momentum space overlap, transitioning to using an adiabatic sweep procedure

[4]The excitation of mechanical motion, due to photon recoil of the Raman state transfer or the differential forces acting on the various atomic and molecular states we work with, can also pose technical difficulties.

[5]to replace the historic but aging M2 TiSa and Coherent dye lasers that both struggle to remain locked to the high-finesse cavity

[6]without further cooling of the molecules once they are produced

[7]For a striking demonstration of this with lithium isotopes, Truscott et. al show condensation in the bosonic isotope and a "fluffy" Fermi gas for the fermionic isotope [34].

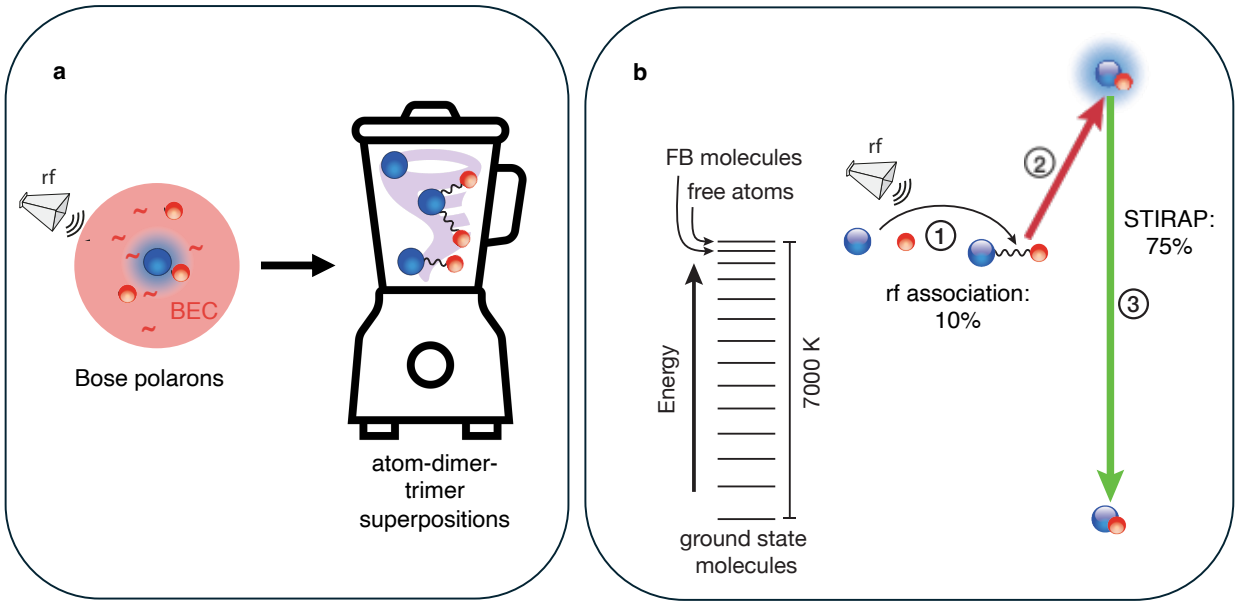

Figure 1.1: Red (blue) spheres represent Na (^{40}K) atoms. (a) A cartoon representation where Bose polarons are prepared and then undergo rf association into even more deeply-bound polaron states with atom, dimer and trimer character. (b) The conventional pathway as described in [29], [33] used to make ground state molecules, with conversion efficiencies labeled. The work depicted in subfigure **a** is in part motivated by the low efficiencies in the rf association step.

may be beneficial, as we describe in the final outlook chapter.

Clearly, the mismatch between the spatial profiles of the two species in the atomic mixture is a hurdle to be overcome. During the completion of this thesis work, other bi-alkali experiments that form Feshbach molecule in the bulk demonstrated techniques that tailor to the properties of each individual species to combat this mismatch. For example, in the JILA ^{40}K^{87}Rb and USTC Na^{40}K experiments a small condensate is immersed in a degenerate Fermi sea with a small boson to fermion number ratio [35], [36]; meanwhile, in the Munich NaK experiment, a a 3:1 K:Na mixture was prepared in a highly species dependent 785nm trap that confines K more tightly than Na [37]. A brief survey of how close these methods (and others, such as evaporation in the presence of external fields) take us to the holy grail of deep quantum degeneracy will be covered in the outlook.

1.2.1 An attempt to use interspecies interactions to boost efficiency

Our approach is unique and complements these approaches, since we instead make use of many-body physics to combat the mismatch in spatial profiles. That is, we exploit *attractive* interatomic interactions, through an interspecies Feshbach resonance, a tool commonly used in AMO experiments to tune the effective attraction/repulsion between atoms, to first build

up an atomic mixture with strong correlations between Na and K atoms before attempting to bind them for transfer into the ground molecular state (see figure 1.1a). We will consider the limit of an impurity concentration of K atoms immersed in a bosonic Na bath. At weak interspecies interactions, we can intuitively see that the mean-field potential of Na will attract the K atoms to where it is densest and most favorable for forming molecules, as shown in figure 1.2. At higher interaction strength, the impurities become dressed by the bosonic bath into strongly interacting Bose polarons, quasiparticles with a well-defined binding energy, lifetime, and strong impurity-bath correlations, as we have characterized in previous experiments [38]. The polarons realized in our experiment were conceptualized originally by Landau and Pekar to describe an electron interacting with an ionic crystal lattice in a solid[39], [40].

By preparing Bose polarons, we can skip the Feshbach association procedure altogether prior to STIRAP, as was shown in Yiqi Ni's thesis work [41], or attempt to form Feshbach molecules from them. The latter actually produces admixed states that can be thought of including both a dimer and intrinsically unstable trimer component, as discussed in Chapter 5.

However, we must acknowledge that to achieve a strong interspecies coupling necessary to form Bose polarons, a dense medium of Na (a condensate) must be used. Even with unity conversion of the impurity species, a large fraction of atoms in the condensate remain unconverted. Both the near-threshold dimer-trimer admixture states (see Chapter 5) and electronic ground state [41] molecules immersed in the remaining condensate have short[8] $1/e$ lifetimes of $\sim$100 μs at the densities used in our experiments[9].

1.2.2 The story of trimers in the Fermi1 experiment

Despite the challenges of using this method to directly populate a long-lived, degenerate Fermi gas of molecules (Feshbach dimers, in this thesis), a careful analysis and interpretation of our experiments instead led us to the discovery of weakly-bound trimers of Na_2K in our experimental system. Although this thesis will be presented in the appropriate pedagogical order, first introducing our spectroscopic measurements detecting trimers (Chapter 4), and then explaining the influence of these few-body bound states as we go into the realm of many-body physics (Chapter 5), this is precisely the opposite of the chronological order of these experiments. In fact, we first took the many-body spectra in the Bose polaron regime that showed a unresolved feature with significant weight at energies below the dimer binding energy. This alerted us to the possible existence of trimers lurking nearby, and motivated the experiments carried out in the balanced, thermal regime, where we did indeed resolve the additional trimer feature in addition to the familiar dimer feature.

The presence of a trimer state near the dimer in our Bose-Fermi mixture has significant implications for the production of ground state molecules. Our observation suggest that it is quite likely that the commonly used technique of sweeping the magnetic field across

[8] relative to how fast we can produce the molecules and remove the condensate from the trap

[9] For Feshbach dimers, this is due to three-body recombination mechanisms, such as relaxation into deeper Na-K bound states, whereas the ground state molecules can undergo the chemical reaction $Na + NaK \rightarrow Na_2 + K$. Both of these processes release potential energy causing the molecules to become lost from the trap.

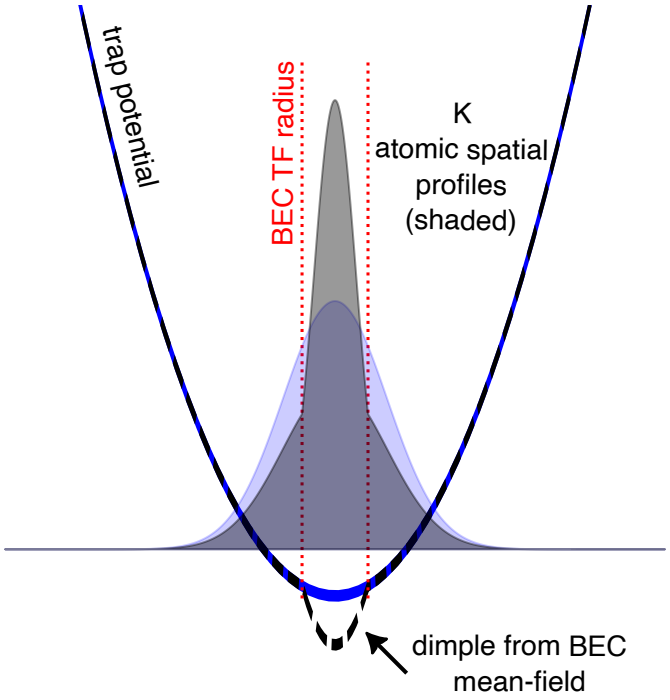

Figure 1.2: A cartoon to illustrate how the mean-field potential of the BEC can attract the K atoms (grey shaded profile) towards where Na atoms are densest. This is in comparison to the atomic profile under only the influence of the harmonic optical potential (blue shaded).

a Feshbach resonance not only creates dimers (which we want for ground state molecule production), but also trimers (which we do not want, because they intrinsically decay quite quickly)[10]. This had previously only been demonstrated in a single-species experiment [42], and in fact the existence of a resolvable trimer state in our mass-imbalanced Bose-Fermi system came as a bit of a surprise, which we will discuss in Chapter 2.

1.3 Outline of this thesis

We will first cover some basic theoretical aspects of molecular states in the halo regime and the Bose polaron problem (Chapter 2). Then, we will discuss the details of our experimental apparatus (Chapter 3). This is followed by an account of the main scientific projects of this thesis (Chapters 4, 5) and the migration of the lab software stack to the labscript-suite (Chapter 6). We will conclude with an outlook on future possibilities in the Fermi1 lab (Chapter 7), and include several appendices on the R&D of lab instrumentation, including kHz linewidth diode lasers, characterization of optical components, and resonant free-space EOMs operating at GHz frequencies.

[10]Therefore, to avoid this, we should avoid working with excessive boson density when forming Feshbach molecules with this technique, since the rate of dimer/trimer formation scales linearly/quadratically with boson density.

Chapter 2

Theory

In this chapter, we will introduce some basic theoretical concepts to describe the two- and three-body molecular bound states we study experimentally in Chapter 4. These bound states are quantum halos, with binding energies extremely close to the dissociation threshold and much larger in spatial extent than what semiclassical physics would predict. We will also motivate the connection between these dimer and trimer states to the attractive Bose polarons studied in Chapter 5.

2.1 Molecular states in the quantum halo regime

The molecular states we study in this thesis are extremely weakly bound, with binding energies of $\sim h \times 10 - 100$ kHz, in contrast to the electronic ground states, which lie deep in the inter-atomic potential well (one billion times deeper, with binding energies of $\sim h \times 100$ THz). This means that the typical semiclassical picture we have of molecules, two atoms connected by a spring of bond length on the scale of ~ 100 pm, that are internally rotating or vibrating (at the GHz and THz energy scales, respectively) is not suitable for describing our experiments.

In fact, to experimentally study these weakly bound states while avoiding detrimental thermal effects such as thermal dissociation, we are immediately taken to the ultracold regime, where quantum mechanical concepts such as the role of partial waves in scattering is important. The temperature scale set by the binding energies is $h \times (10\text{kHz})/k_B \approx 500$ nK, and at these temperatures, we are well below the centrifugal barrier for atoms colliding with nonzero angular momentum. As such, the quantum statistics of the atoms participating in the collision is of paramount importance, and s-wave scattering dominates. Additionally, the thermal deBroglie wavelength is much greater than the length scales of the scattering potentials, so a good fraction of the relevant physics can be described by a zero-range pseudopotential which reproduces the correct asymptotic form of the wavefunction at large separations.

Both the familiar Feshbach dimers and the discovered trimers described in this work have spatial extent far beyond the van der Waals range of their interatomic potentials, and instead are much better described by their s-wave scattering length (typically for us ~ 1000 a_{Bohr}). Using a term first coined in nuclear physics to describe states of nuclei much larger

than their semi-classical radius [43], both of these molecular states are in the "halo" regime. Solving the quantum three-body problem in such a system yields fantastic phenomena such as the famous Efimov effect [44]. We will briefly review such results below, but we will also refrain from dubbing our trimers as "Efimov" trimers. This is because we neither observe a second bound state with the predicted geometric scaling factor (as was done using loss resonances in [45]–[48], for example) nor directly examine the spatial structure of our bound state (with the Coulomb explosion imaging technique in [49]). In fact, there is not a clear agreement in the literature as to what defines an Efimov state, as discussed in section 4.5 of [50].

2.1.1 Dimers

We briefly quote a few well-known results about shallow two-body bound states. As discussed before, we will only consider s-wave scattering. To gain some intuition about the relationship between the s-wave scattering length a and bound states near the scattering continuum, we can solve the finite square well potential with variable depth, as done in section 5.2 of [51]. The essential result is that as the depth is tuned such that a new bound state becomes supported, the scattering phase shift approaches $\pi/2$, the bound state has wavefunction $\exp(-r/a)$ for large separations r and energy $-\hbar^2/(2\mu a^2)$ (where μ is the reduced mass), and a formally diverges.

We can explore similar phenomena in the two-channel problem, as discussed in section 5.3 of [51]. In the absence of coupling between channels, we can vary the energy of the scattering state in one channel to bring it near resonance with a bound state in the other. Near the resonance condition, coupling between the two channels gives rise to a dramatic variation in the phase shift and scattering length, and again the bound state properties will be as previously described.

The phenomena in the coupled two-channel problem discussed is that of a Feshbach resonance, which is thoroughly reviewed in [52]. The idea that we have differential tuning between the two scattering channels is far from a simple academic exercise, and this idea can be realized in experiments with condensed matter [53] and, of relevance to us, in cold atoms. In atomic systems, since the two channels have different magnetic moments (the electrons are in a singlet or triplet state), we can therefore tune near a resonance condition by the precise application of an external magnetic field. Furthermore, there is nonzero coupling between channels, coming from each atom's internal hyperfine structure. Altogether, this makes the use of Feshbach resonances an everyday tool in our experiment, and it allows us to tune the binding energy of the shallow bound states we would like to study, as well as the scattering length between colliding atoms, as schematically shown in figure 2.1.

2.1.2 Trimers

Now that we have discussed how resonance phenomena can lead to shallow two-body bound states extending on the scale of the s-wave scattering length (which can be tuned to diverge), we will summarize some key results in the analogous three-body problem, as reviewed in [50] and thoroughly covered in [54]. We will assume that we have three resonantly interacting identical bosons in a symmetric state. We can then mathematically capture the effect of their

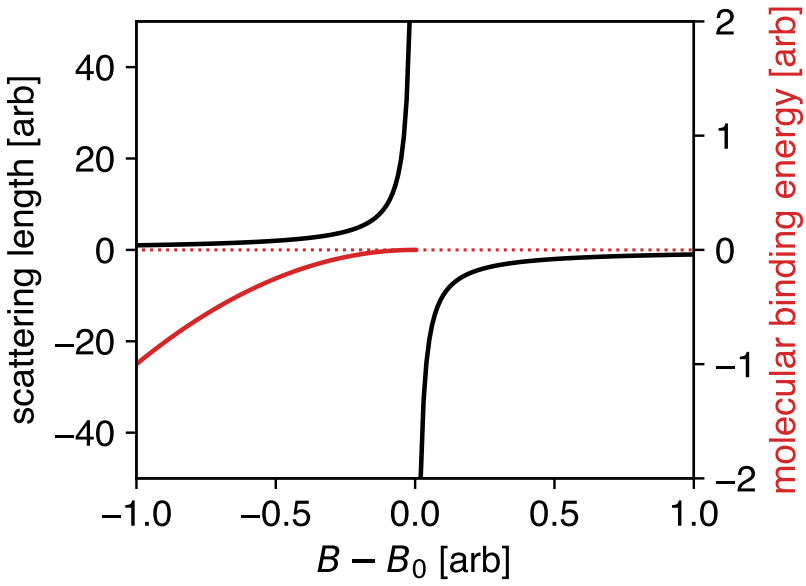

Figure 2.1: Near a Feshbach resonance at magnetic field B_0, both the scattering length and molecular binding energy depend strongly on the magnetic field B. The approximate scalings are energy $\propto -1/a^2$ and scattering length $a \propto 1/(B - B_0)$.

interactions by enforcing the Bethe-Peirels boundary condition on (many-particle) wavefunction Ψ when any two particles come into contact, i.e., $-(1/r\Psi)\partial_r(r\Psi) \to 1/a$ for vanishing separation, $r \to 0$. It is most convenient to apply this boundary condition when solving the free Schrodinger equation using Jacobi coordinates, and the problem simplifies to a set of 1D Schrodinger equations in the hyper-radial coordinate R. The hyper-radius essentially gives the size of the three-body bound state, and it satisfies $R^2 = (2/3)\sum r_{ij}^2$, where the sum is over all pairs of particles. This set of equations is indexed by n, corresponding to the roots of the equation $-s_n \cos(s_n\pi/2) + (8/\sqrt{3})\sin(s_n\pi/6) = 0$, and has solutions given by the hyper-radial function F_n satisfying

$$\left(\partial_R^2 + V_n(R) - k^2\right)\sqrt{R}F_n(R) = 0. \tag{2.1}$$

We have an imaginary root $s_0 \approx \sqrt{-1}$ for $n = 0$, and for $a \to \infty$, this results in an effective Efimov attraction potential

$$V_0 = -\frac{|s_0|^2 + 1/4}{R^2}. \tag{2.2}$$

The effective long-range potential arising from short-ranged two-particle interactions is a key result. We can gain some intuition for this effect by considering an analogous problem in a different regime, with two heavy particles and one light. This is known as the Born-Oppenheimer regime, and in this picture we can also get an $1/R^2$ potential as the light particle's rapid motion can mediate the interaction between the two heavy particles [55]. Strictly speaking, this does not apply for the original problem of three equal masses and is only a rough analogy.

There is a glaring problem with the $1/R^2$ potential discussed above. It exhibits continuous scale-invariance; that is, given a solution F_0 with energy E, we can rescale the original solution for a new one such that

$$R \mapsto \lambda R, E \mapsto \lambda^2 E. \tag{2.3}$$

Since λ can be an arbitrary scalar, bound states of infinitely deep energies are permitted, and in principle imply that such systems should undergo Thomas collapse[1][56]. This is a physically unrealistic prediction, and in particular between atoms there is a strong short-range repulsive interaction that prevents the system from collapsing. This can be modeled by an extra hard-core boundary condition at short-range, and this is one way of implementing a new length scale in the problem known as the three-body parameter. In this simple zero-range picture, choosing the three-body parameter is done by matching the predictions of this model to measured physical observables, such as the spatial structure or energy of a bound state. A surprising consequence of this is that we still have a discrete scale invariance describing an entire family of solutions, such that the scaling parameter λ is no longer arbitrary but instead determined by the masses, interparticle scattering, etc, as shown in figure 2.2. For three equal masses resonantly interacting, $\lambda = \exp(\pi/|s_0|) \approx 22.7$, but this can vary dramatically for imbalanced masses, going as low as ≈ 5 for Li + Li + Cs trimers (mass ratio $\sim 1:20$) [47], [48], and calculated to be ≈ 100 in our trimers of Na + Na + K (mass ratio $\sim 2:1$).

This family of trimer bound states exists on both sides of the Feshbach resonance, as schematically shown in figure 2.3. Going to the side where $a < 0$ and no two-body bound states exist near the threshold, we find the so-called "Borromean" states that become less deeply bound until they cross the three-atom scattering continuum. [2] On the other side where $a > 0$ and a shallow dimer state exists, we find that as a decreases, both the dimer and trimer states become more deeply bound, but the trimer state eventually crosses with the dimer-atom scattering continuum.

This energy landscape of dimers and trimers near a Feshbach resonance has important experimental implications for the detection of trimer bound states. The merging of the trimer states with the scattering continuum (three free atoms and atom-dimer for positive and negative scattering lengths, respectively) results in loss resonances, which can be detected experimentally. An alternative is the technique we will describe in this thesis, where we directly populate the dimer and trimer bound states via an rf drive.

The results from the universal zero-range theory serve as an excellent starting point for understanding the physical phenomena we expect to see in our experiment, but to accurately reproduce the binding energies and scaling factors measured in experiment, the details of the scattering potentials must be accounted for as well. For instance, in numerical calculations of the binding energy and wavefunctions, one of our theory collaborators Arthur Christianen uses model potentials not only matching the two-body scattering lengths, but also the van der Waals range [57]. The theoretical question of whether additional details (such as the

[1] and therefore release infinite amounts of energy!

[2] The existence of Borromean states is perhaps one of the simplest examples of competition in a many-body system, between the zero-point kinetic energy which delocalizes a system versus pairwise interactions holding the system together. For N particles, the former scales as N while the latter scales as N^2, and in crossing over from two to three particles we find the latter scaling begin to dominate.

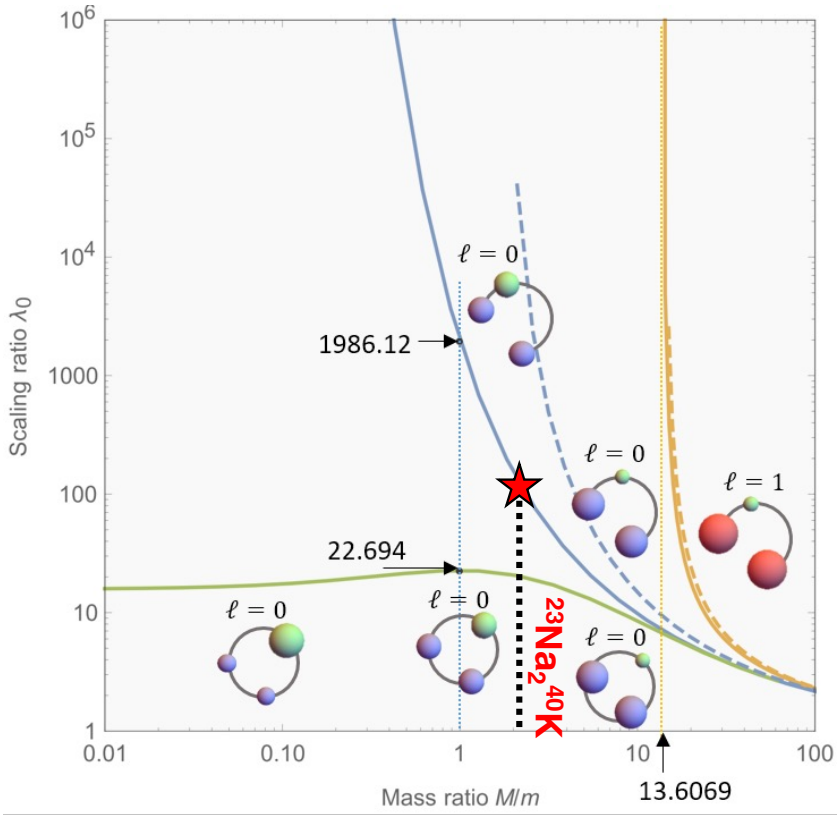

Figure 2.2: The scaling ratio depends on both the mass ratio and the strength of pairwise interactions. The green curve shows three resonant interacting pairs, while the blue shows two resonant pairs and one non-interacting. The black dashed line gives the mass ratio for our trimer, and the Na-Na interaction is weakly repulsive. The red marker roughly our experiment on this plot, with $\lambda \approx 100$. Reproduced and adapted from [50].

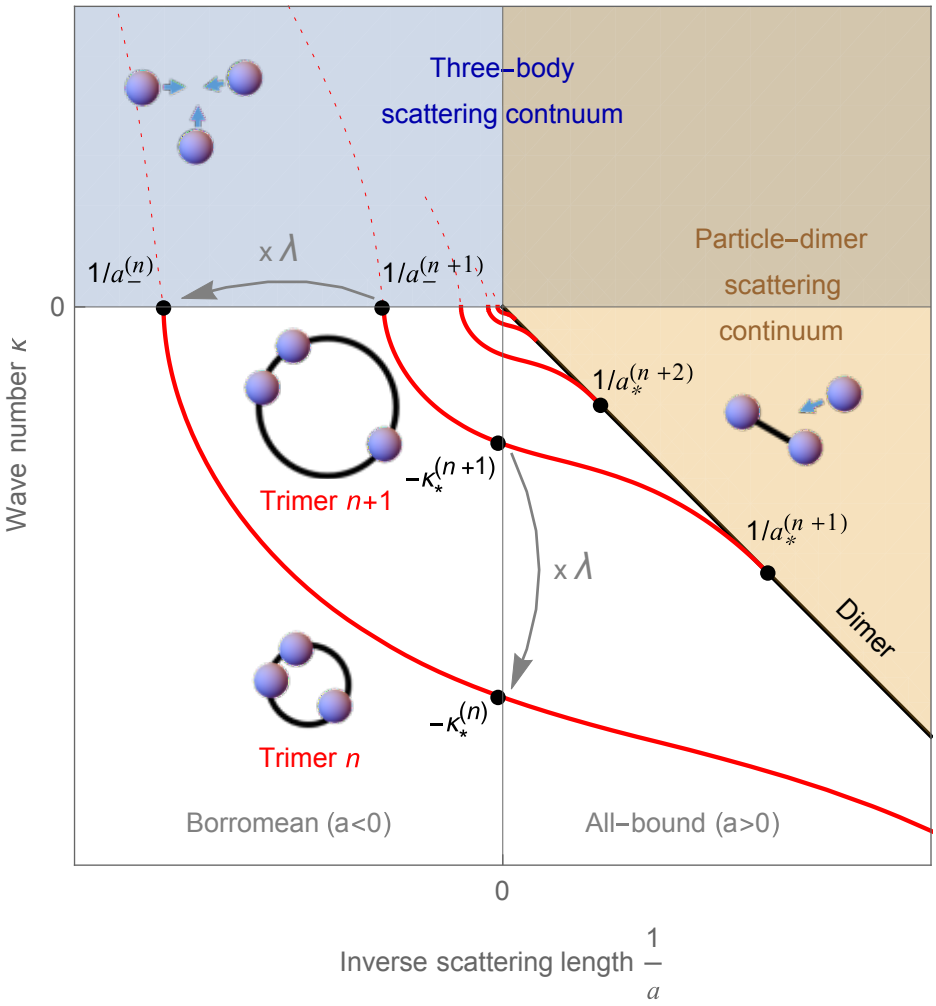

Figure 2.3: The energy landscape of the Feshbach dimer and Efimov trimers vs inverse scattering length $1/a$. The wavenumber $\kappa = \sqrt{m|E|}/\hbar$ associated with particles of mass m energy E is plotted on the vertical axis. The experiments described in this thesis are in the "All-bound" regime, where the trimer and dimer binding energies approach each other as one moves away from the resonance at $1/a = 0$. Reproduced from [50].

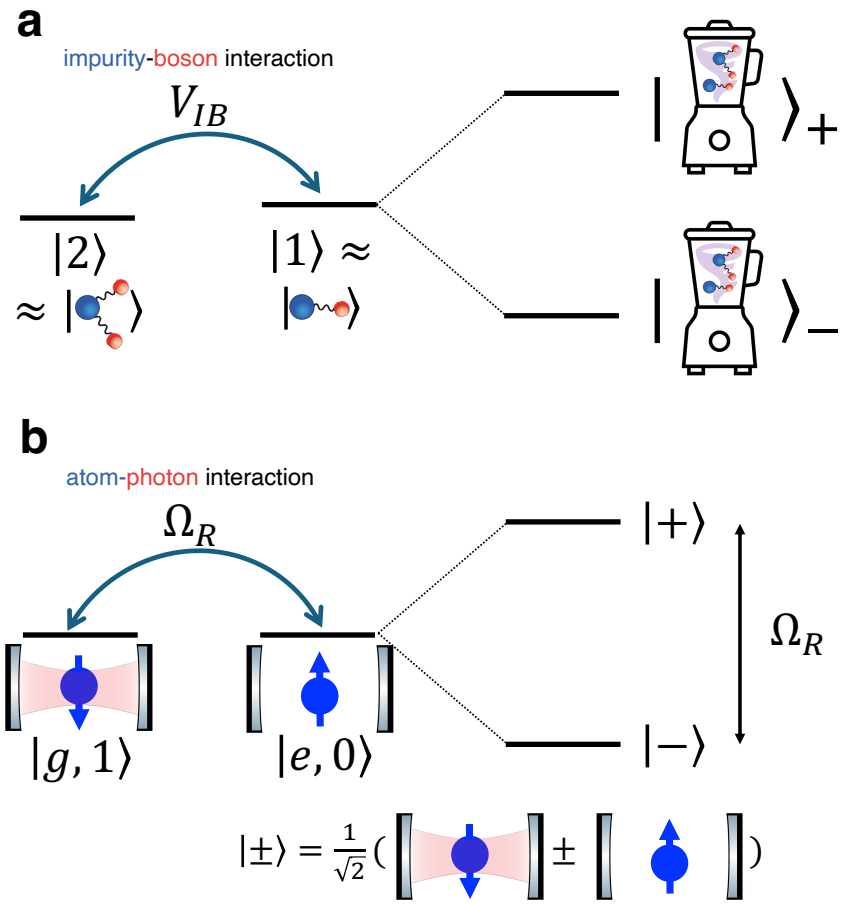

Figure 2.4: Both (a) the dimer and trimer states dressed by a BEC and (b) the atom-photon product states from cavity QED undergo admixing to form new eigenstates which exhibit level repulsion. See equations 2.8 for definition of $|1\rangle, |2\rangle$ in (a). In (a), we have omitted the repulsive polaron branch ($|0\rangle$ of equations 2.8) in this schematic representation.

properties of the specific Feshbach resonance being used) can further improve the accuracy of calculations is in fact under active investigation [58].

2.2 Hybridization of dimers and trimers

So far, we have formulated the problem of solving for dimer and trimer bound states in systems with fixed particle numbers (either two or three). This is appropriate to describe experiments carried out with sufficiently dilute gases, as in Chapter 4. However, some of our experiments (as described in Chapter 5) are carried out with K impurities strongly interacting with a Bose-Einstein condensate. This is the Bose polaron scenario, where an impurity interacts with and is dressed by a bosonic bath. Here, the BEC can be thought of as a reser-

voir of particles in a coherent state that interact with the impurity atom, much like how one might describe photons in a laser field interacting with an (atomic) emitter in the language of quantum optics, as shown in figure 2.4. In cavity QED, strong coupling between the photon field and an atom results in dressed eigenstates that exhibit level repulsion. Analogously for us, in a sufficiently dense BEC, strong mixing between the dimer and trimer bound states and the corresponding level repulsion provides a simple picture for understanding the energy scales in our experimental observations. In this scenario, there is no reason to believe that the eigenstates of the system are described by states with a definite particle number, just as the dressed eigenstates in cavity QED do not have definite photon number.

We will briefly state a few of the key highlights regarding the theoretical modelling of the Bose polaron problem, drawn from the thesis [57] which has several chapters relevant to describing our experiments. For simplicity, we will assume a single impurity immersed in a spatially homogeneous BEC. The Hamiltonian describing this system has three terms; first, we have for the BEC its background energy, excitations, and interboson repulsion terms, respectively,

$$H_{\mathrm{BEC}} = -E_{bg} + \int_{\mathbf{k}} \left(\frac{\hbar^2 k^2}{2m} - \mu \right) \hat{b}_k^\dagger \hat{b}_k + \frac{1}{2} \iint_{\mathbf{r},\mathbf{r}'} V_{BB}(\mathbf{r} - \mathbf{r}') \hat{b}_{\mathbf{r}}^\dagger \hat{b}_{\mathbf{r}'}^\dagger \hat{b}_{\mathbf{r}} \hat{b}_{\mathbf{r}'}, \tag{2.4}$$

for bosons at positions $\mathbf{r}, \mathbf{r}'$ of mass m, chemical potential μ, annihilation operator $\hat{b}$, and interboson repulsion V_{BB}. We will note that even though the interboson repulsion is rather weak in our system relative to the impurity-boson coupling, with scattering lengths of $\sim 50, 1000 a_{\mathrm{Bohr}}$ respectively, the inclusion of its effect is necessary, to avoid a collapse of the entire bath onto the impurity, e.g., [59]. For the impurity we have its kinetic energy,

$$H_{\mathrm{impurity}} = \frac{\mathbf{P}^2}{2M}, \tag{2.5}$$

for momentum $\mathbf{P}$ and mass M. Finally, we have the interaction term between the impurity at position $\mathbf{R}$ and the BEC,

$$H_{\mathrm{interaction}} = \int_{\mathbf{r}} V_{IB}(\mathbf{r} - \mathbf{R}) \hat{b}_{\mathbf{r}}^\dagger, \tag{2.6}$$

where V_{IB} is the interaction potential. Both the Bose-Bose repulsion V_{BB} and the impurity-bath potential V_{IB} are approximated using Gaussian potentials with parameters chosen to match the known effective range and scattering length (see equation 7.1 and 6.16 of [57], respectively).

To approximate the ground state energy of this system, we consider states where we add excitations "deforming" the BEC due to impurity-boson correlations. As an example, we can use what we call the "double-excitation" ansatz,

$$\psi_{\mathrm{DE}} = \left(1 + \int_{\mathbf{r}} \beta(\mathbf{r}) \hat{b}_{\mathbf{r}}^\dagger + \iint_{\mathbf{r},\mathbf{r}'} \alpha(\mathbf{r}, \mathbf{r}') b_{\mathbf{r}}^\dagger b_{\mathbf{r}'}^\dagger \right) |\mathrm{vacuum}\rangle_{\mathrm{BEC}}, \tag{2.7}$$

while varying the functions α, β. For $\alpha = 0$, this corresponds to the Chevy ansatz which describes the complementary Fermi polaron (impurity interacting with a Fermi sea) problem

quite well [60], since Pauli blocking suppresses higher-order correlations. In the bosonic case, it is even possible to consider ansatz parametrizing an infinite series of excitations, for instance, by applying a operator exponential to $|\text{vacuum}\rangle_{\text{BEC}}$, e.g., the Gaussian states discussed in Ch. 3 of [57].

We find, however, that we can reproduce the energy scales measured in experiment by considering our problem in a simple three-level model, spanning the basis of three states of the form given in equation 2.7. The (uncoupled) basis we use is given by the conditions

$$|0\rangle \in \{\psi_{\text{DE}} : \alpha = \beta = 0\}, \tag{2.8}$$

$$|1\rangle \in \{\psi_{\text{DE}} : \alpha = 0\}, \tag{2.9}$$

$$|2\rangle \in \{\psi_{\text{DE}} : \beta = 0\} \tag{2.10}$$

and from each subspace a basis state is chosen to be variationally minimized with respect to the Bose polaron Hamiltonian $H = H_{\text{BEC}} + H_{\text{impurity}} + H_{\text{interaction}}$. These states, in the limit of a dilute bath, correspond to the free, dimer and trimer states of fixed particle numbers, discussed in a previous section. The coupling between the chosen basis states is given by the matrix elements of H. In our experiment, the difference between the bare energies of $|1\rangle$ and $|2\rangle$ are small compared to this coupling, and therefore the we have strong mixing between these two states. This is essentially the same mechanism as Rabi splitting in a two-level system from quantum optics, except instead of a laser field providing coupling, we have a BEC! A graphical representation of this argument is shown in figure 5.1, and the comparison to experiment is shown in 5.3. This simplified picture, however, cannot fully describe the spectrum measured in experiment, since using discrete levels inherently neglects the continuous spectrum of low-energy excitations of a BEC (e.g., phonons).

While the story of mixed states and level repulsion provides an energy scale matching the width of the spectra measured in experiment, a measurement of energies on its own does not strongly demonstrate either the admixture or coherence of these superposition states. One hint of their admixed nature is through the careful experimental study of their lifetimes. Given that our "bare" states both have finite but different decay lifetimes, as they are coupled, the admixture of each in the new eigenstates results in their lifetimes becoming more similar. We can model this using a non-Hermitian Hamiltonian with detuning Δ between the uncoupled states, decay rates of Γ_1, Γ_2 , and coupling Ω and solving for its eigenenergies $E_\pm$,

$$\begin{bmatrix} -\Delta/2 + i\Gamma_1 & \Omega/2 \\ \Omega/2 & \Delta/2 + i\Gamma_2 \end{bmatrix}. \tag{2.11}$$

Plotting the imaginary component of these energies $\Gamma_\pm \equiv \text{Im}\{E_\pm\}$, we find that $\Gamma_+ \to \Gamma_-$ as $|\Omega/\Delta| \to \infty$, as shown in figure 2.5. Our measurements are consistent with this as well. Experimentally verifying the coherence of such states, however, is less trivial, and we briefly discuss some ideas along these lines in Chapter 7.

Thus far, we have not discussed the effect of finite temperature in such an experiment. Whether or not the phenomena described in Chapter 5 survive in the presence of thermal dephasing may also provide insight into how crucial of an ingredient quantum coherence is for explaining our observations. Furthermore, the study of the Bose polaron problem at finite temperatures is non-trivial from a theoretical standpoint, e.g., see [61], [62]. This is a

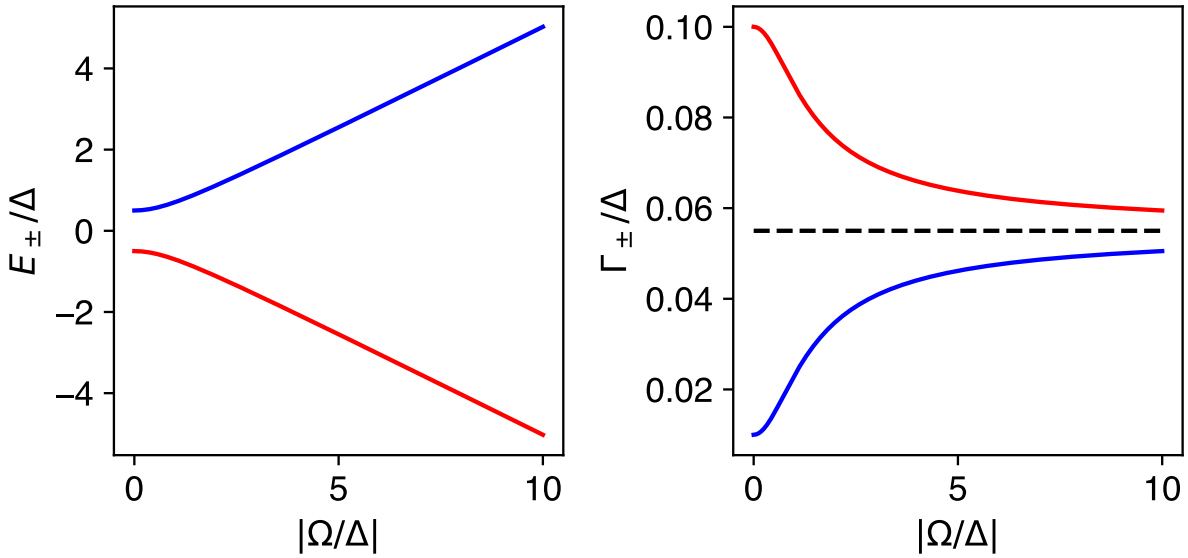

Figure 2.5: An model (diagonalizing equation 2.11) of how coupling two states with different lifetimes creates a new state inherits the lossy character of each individual state. We plot the real (left) and imaginary (right) parts of the eigenenergies as a function of the coupling strength. The dashed line is the arithmetic mean of the two decay rates.

question ripe for exploration from both experimental and theoretical viewpoints which we will leave for future work.

Chapter 3

Experimental apparatus

In this chapter, we document various details on characterizing and improving the experimental apparatus performed over the course of my degree[1]. The procedure of preparing samples of ultracold Na-K atomic mixtures for performing the experiments in Chapters 4, 5 are largely the same as described in Yiqi Ni's thesis [41].

For a historical account of how the machine was built from the ground up, see the previous theses from members of Fermi1 [28], [63], [64].

3.1 Trapping potentials

Almost all the scientific experiments we carry out are with a trapped sample of atoms or molecules, which allows us to hold, prepare, and probe samples over timescales of ~ 10 s. The trap is generated through the careful application of a combination of magnetic and optical forces to prevent the particles from freely expanding and falling under the influence of gravity. Additionally, for both the purpose of studying Bose-Fermi and molecular physics, overlapping the ^{40}K and Na ensembles in space is crucial[2]. In this section, we discuss in detail the properties of the trap (both in theory and what we measure) to achieve these goals.

3.1.1 Three forces to consider

The various forces discussed are shown in figure 3.1.

Gravity

^{23}Na and ^{40}K have different atomic masses, therefore they have different weights $m_{Na}g$, m_Kg.

[1]The work described here would not have been possible without my colleagues in the lab: Zoe Yan, Carsten Robens, Yiqi Ni, Eric Wolf, Huan Bui and Yiming Zhang.

[2]While we will not directly address the forces acting on the molecular states we work with in Fermi1, many of these ideas are relevant there as well, to avoid inadvertently exciting undesired motion of Feshbach/ground state molecules after they are produced.

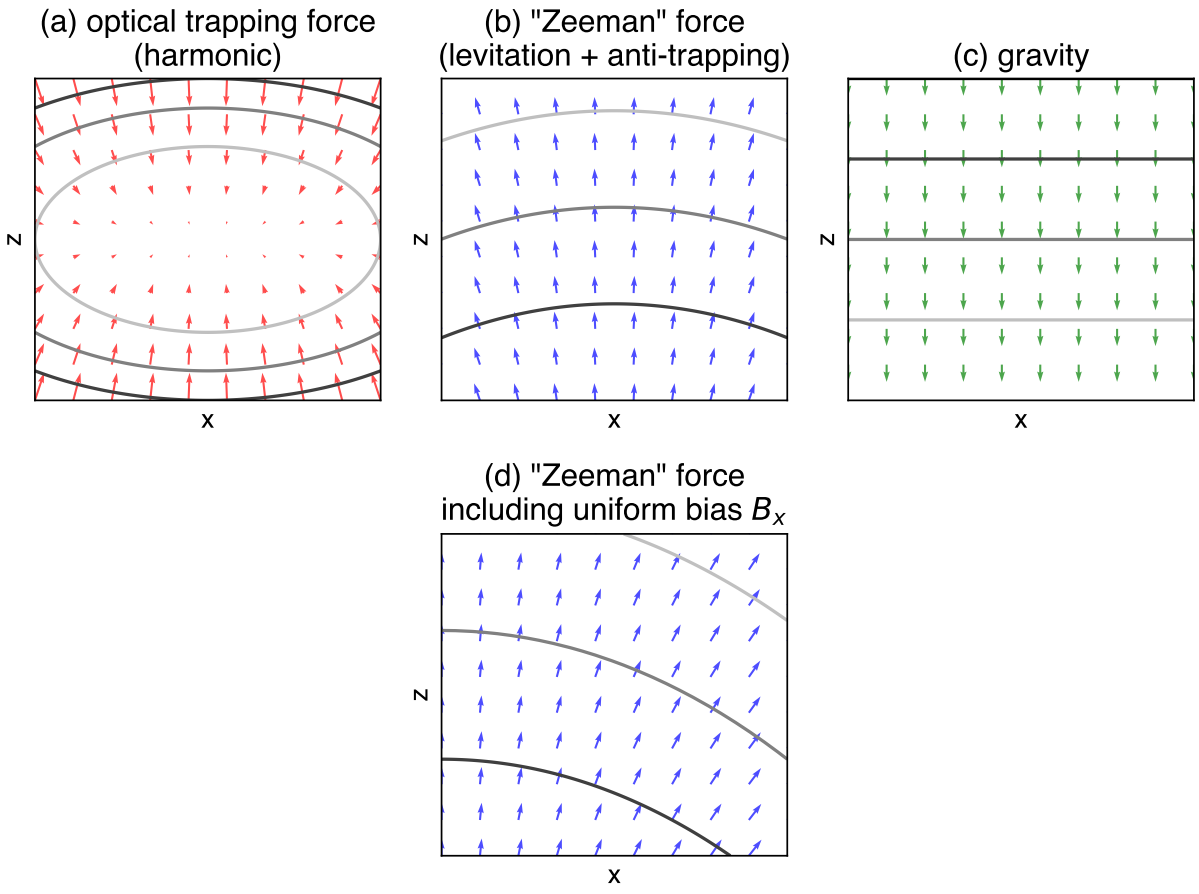

Figure 3.1: A schematic depicting the spatial variation in the forces that play a role in the confinement of atoms. Contours show equipotentials of each force. In (a) the ratio of trapping potentials and in (b) the relative magnitude between transverse and vertical forces has been exaggerated for visual clarity.

lab	paper
x	z (approximate cylindrical symmetry axis)
y	y
z (gravity)	x

Table 3.1: A translation table between lab and paper (publication) axis naming conventions. The lab axes follow the naming conventions for the magnetic bias field coils, while the paper axes emphasize the cylindrical symmetry of the cigar-shaped trap.

Optical

The optical force arises from the AC Stark shift of the crossed 1064 nm ODT (optical dipole trap) beams, see figure 3.2. Since 1064 nm is far off-resonant from all optical transitions of both species, one can approximate fairly well the trapping potentials using perturbation theory, with the knowledge of the dipole transition matrix elements, especially those contributing to the D1 and D2 lines, which comprise the majority of the oscillator strength. In this particular case of perturbation theory, 1064 nm is sufficiently close to "DC" (zero frequency) that accuracy on the order of 10% requires including both the co-rotating term $\propto 1/(\omega_L - \omega_0)$ and the counter-rotating term $\propto 1/(\omega_L + \omega_0)$, where ω_L (ω_0) are the frequency of the trapping laser (atom). The ratio of the trapping frequencies are then given by the ratio of masses, and has been measured by us experimentally, see the Methods section of [65].

Magnetic/Zeeman

The magnetic force is due to the Zeeman shift. We typically work with ^{40}K $|9/2, -9/2\rangle$ and ^{23}Na $|1, 1\rangle$, although we do also work with ^{40}K $|9/2, -7/2\rangle$ to prepare for rf association of Feshbach molecules. We work with magnetic fields of around 100G, where the energy vs magnetic field is approximately linear,

$$\langle H_{Zeeman} \rangle \approx \mu_B g_F m_F B_{ext}, \tag{3.1}$$

and is precisely linear for stretched states. The force on an atom moving sufficiently slowly such that its magnetic dipole can adiabatically follow the change in magnetic field is $-\nabla \langle H_{Zeeman} \rangle$.

3.1.2 Experimental details

The geometry of the crossed-ODT

Measuring two trapping frequencies and the ellipticity of each trapping beam is sufficient to determine the third unknown trapping frequency, given the crossed geometry shown in figure 3.2. Conversely, one can use this to cross-check experimental measurements.

Only in this section "The geometry of the crossed-ODT," we will follow the "paper" axis naming conventions as specified in table 3.1. The intensity of light near the trap center, in

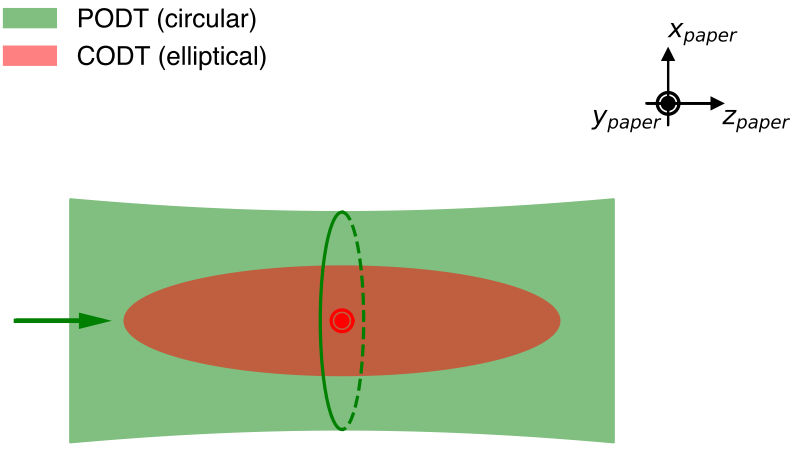

Figure 3.2: The Fermi1 experiment has two crossed 1064 nm ODT beams, shown in false color. The green is the circular "PODT" ("plug" ODT), while the red is the elliptical "CODT" ("computer ODT"), following the historical naming convention from previous generations. Beam waists are not shown to scale.

the limit of infinite Rayleigh range for both beams, is

$$I(x, y, z) = I_{PODT}(x, y) + I_{CODT}(x, z),$$

For ODTs, the trapping potential U is directly proportional to the intensity of light, and the total potential is

$$U(x, y, z) = U_{PODT} + U_{CODT}.$$

To derive trapping frequencies, we make the approximation that the trap is harmonic near its center,

$$\frac{1}{2}m\omega_i^2 r_i^2 = \frac{1}{2}\frac{\partial^2 U}{\partial r_i^2} r_i^2. \tag{3.2}$$

The LHS is the potential energy stored in a spring, whereas the RHS is the Taylor expansion of the potential about its minima.

In our geometry, the PODT (CODT) is solely responsible for y (z) confinement, i.e.

$$\omega_y^2 \propto \frac{\partial^2 I_{PODT}}{\partial y^2}, \omega_z^2 \propto \frac{\partial^2 I_{CODT}}{\partial z^2}.$$

For this reason, assume that these frequencies have been measured. However, in the x-direction, both beams contribute to the confinement, and thus we decompose the trapping frequency into two terms corresponding to the second derivative of each beam's intensity profile,

$$\omega_x^2 = \omega_{x,PODT}^2 + \omega_{x,CODT}^2.$$

(For concreteness, $\omega^2_{x,PODT} \propto \partial^2 I_{PODT}/\partial x^2$.)

We can identify due to the circular symmetry of the PODT beam

$$\omega_{x,PODT} = \omega_y.$$

Similarly we can relate $\omega_{x,CODT}$ to ω_z, with knowledge of the ratio of its beam waists, $\epsilon = w_x/w_z$ ($\epsilon = 4$, as last set up by Carsten Robens in preparation for the experiments in [38]). The elliptical intensity profile is

$$I_{CODT}(x,z) = I_0 \exp\{(-2x^2/w_x^2)\} \exp\{(-2y^2/w_y^2)\}.$$

Using equation (1),

$$\omega^2_{x,CODT} = \epsilon^2 \omega_z^2.$$

Thus the relation between the trapping frequencies is

$$\omega_x = \sqrt{\omega_y^2 + \epsilon^2 \omega_z^2}. \tag{3.3}$$

Gravitational sag in an ODT

We first consider only the effects of the optical dipole trap and gravity. Near the minimum of the optical potential, we can approximate its force as a linear restoring spring force,

$$F_{opt} \approx -kx = -m\omega^2 x.$$

The equilibrium position of the spring is given by where the force is zero,

$$m\omega^2 x_{eq} + mg = 0 \implies x_{eq} = g/\omega^2.$$

Since the trapping frequency ω is species-dependent, this implies that the two clouds will have different center positions along the gravity axis. A rough number for our experiment is $\omega \approx 2\pi \times 100$ Hz (125 Hz) for Na (K) along this axis, yielding a displacement of ~ 25 μm (16 μm) along the gravity axis.

This presents a limitation for science that requires spatial overlap (e.g., creation of ground state molecules from the component gases) and readout (e.g., two clouds will not simultaneously be perfectly in the imaging plane without differential alignment of downstream species-specific optics).

Magnetic levitation force

Fortunately, we have a third force readily available from a spatially in-homogeneous magnetic field we can apply. We typically do science with a homogeneous field applied with Helmholtz coils, a.k.a. the Feshbach "FB" field, along with an in-homogeneous field with anti-Helmholtz, a.k.a. the Stern-Gerlach "SG" field, coils along the same axis (parallel to gravity). A description of the most recent modification to these coils, which require moderately high currents and water cooling, is in the thesis [64].

As a very simple model, we will completely neglect the spatial dependence of the field from the Helmholtz coils, treating it as a constant B_{FB}. Meanwhile, the SG field along the coil axis has a spatial dependence

$$B_{SG}(z) \propto \left[1 + (z/a - d/(2a))^2\right]^{-3/2} - \left[1 + (z/a + d/(2a))^2\right]^{-3/2}$$

for coils of radius a and separation d. Altogether, along the symmetry axis (z) of the coils, the z-component of the B-field is

$$B(z) = B_{SG}(z) + B_{FB}.$$

The B-field can be reasonably approximated as linear for the central region of this curve, and thus it imparts a spatially uniform force (see figure 3.1b, along the symmetry axis $x = 0$).

The force is then, using the approximation from equation 3.1,

$$F = \mu_B g_F m_F \frac{dB_{ext}}{dz}.$$

The ratio of the forces between each species is

$$\frac{F_K}{F_{Na}} = \frac{g_F m_F|_K}{g_F m_F|_{Na}}.$$

For the ground hyperfine states of each species, the ratio is

$$\frac{(2/9) \times (-9/2)}{(-1/2) \times 1} = 2.$$

By our choice of species, this is quite close to the weight ratio

$$\frac{m_K g}{m_{Na} g} = \frac{40 \text{ amu}}{23 \text{ amu}} \approx 1.74.$$

So it is possible to perfectly levitate one species against gravity and still provide some compensation to gravity on the other. Historically, the SG field was chosen to optimize the cloud overlap for a specific configuration of the ODT (power and beam shapes). For instance, see Zoe Yan's thesis [64].

The gradient needed to perfectly levitate Na in the 1,1 state is

$$\frac{dB}{dz} = \frac{m_{Na} g}{g_F m_F \mu_B} \approx 807 \text{ G/m}. \tag{3.4}$$

Note that the presence of the bias field B_{FB} prevents the field from vanishing and reversing direction along the z-axis. Without the bias field, the anti-Helmholtz field will not provide a spatially uniform force.

The model presented in this section is useful to get only a rough physical understanding of the experiment. For example, it is almost certainly guaranteed that the ODT is not perfectly in the center of the coils, the coils are imperfectly wound and asymmetric, etc. In fact, we know that during trap frequency measurements, modulating the SG field will impart not only a force along the symmetry axis of the coils, but also orthogonal to it. Additionally, we know that applying the SG field imparts an additional bias on the atoms by 1 G, which tells us that the atoms sit roughly 1 mm away from the center of the SG coils.

Additional mechanical effects of applied magnetic fields

The combination of using a Helmholtz coil and anti-Helmholtz coil in parallel does not only provide a levitation force. It also creates a potential in the plane normal to the symmetry axis of the coils, as shown in figure 3.1b! We will also consider the application of a uniform bias field in the plane normal to z.

Let us now define the origin of our coordinates to be on the symmetry axis (z) and halfway between the coils. Then the total vector field is

$$\vec{B}(x,y,z) = \vec{B}_{SG} + \vec{B}_{FB} \approx \left[\frac{B'}{2}x, \frac{B'}{2}y, -B'z\right] + [0,0,B_{FB}], \tag{3.5}$$

where the approximation is taken near the origin and $B' \equiv dB/dz$.[3]

Along the x-axis (or equivalently y, due to cylindrical symmetry), the field magnitude as a function of position is

$$\begin{aligned} |B(x, y=0, z=0)| &= \sqrt{B_{FB}^2 + (B'x/2)^2} \\ &\approx B_{FB} + (B'x/2)^2/B_{FB}, \end{aligned} \tag{3.6}$$

where the approximation is valid where $B_{FB} \gg B'x$. This gives the anti-trapping (at least for the strong-field seeking states typically used for science) potential in the xy-plane.

To get an estimate for the strength of this trapping potential, we use the gradient calculated earlier to levitate an Na 1,1 atom. Even though this is an *anti-trapping* potential, as shown in figure 3.1b, we nonetheless quote "trapping frequencies" (you could perhaps think of them as imaginary) to quantify the curvature of the potential, for easy comparison to the optical dipole trap later. Such a potential has a (imaginary) frequency of

$$\omega_{xy} = \sqrt{\left|\frac{2g_F m_F \mu_B (B'/2)^2}{m B_{FB}}\right|}. \tag{3.7}$$

For a typical science field of $B_{FB} = 100$ G, for both species we have

$$\omega_{xy} \approx 2\pi \times 1 \text{ Hz}.$$

The center of this anti-trapping potential can be shifted by applying a second uniform bias field in the xy-plane B_{bias}, say along x. Its position x_{mag} moves as

$$x_{mag} = \frac{2B_{bias}}{B'} \approx (2.5 \text{ mm/G}) \times B_{bias}. \tag{3.8}$$

So even for a moderate B-field of several Gauss this can be significant, relative to the typical cloud sizes in-situ ($\sim$ 10–100μm).

[3] A simple mnemonic for remembering the approximate form of the SG-field is to remember $\nabla \cdot B = 0$ and the cylindrical symmetry present in the scenario.

Using bias fields to displace the trap center

Since it is possible to displace the magnetic anti-trap center by applying a bias field, this becomes a tool for inducing center-of-mass motion for an atom cloud. The overall trapping potential along the x-axis is then

$$U_{trap} = \frac{1}{2}m\omega_{ODT}^2 x^2 - \frac{1}{2}m\omega_{mag}^2(x - x_{mag})^2, \tag{3.9}$$

where we replace the subscript $\omega_{mag} \equiv \omega_{xy}$ for clarity. The overall trap center then moves to where $dU_{trap}/dx = 0$, i.e.

$$x_0 = \frac{\omega_{mag}^2}{\omega_{ODT}^2 - \omega_{mag}^2} x_{mag} \approx \left(\frac{\omega_{mag}}{\omega_{ODT}}\right)^2 x_{mag} \propto B_{bias}. \tag{3.10}$$

This is schematically depicted in figure 3.1(d). Of course, this should be taken with a grain of salt since both trap potentials are anharmonic. An important consequence of this is that displacements along the tight axis of the trap are smaller for the same applied B-field.

Observing center-of-mass motion in time-of-flight

To observe the center-of-mass motion, we can either look *in situ* or by releasing the atoms from the trapping potential (time-of-flight). To see why time-of-flight is commonly needed, consider that the bias fields available in the lab are on the order of 4 G. Using the $\omega_{ODT}^{labX} \approx 2\pi \times 10$ Hz and $\omega_{ODT}^{labY,labZ} \approx 2\pi \times 100$Hz, by adiabatically ramping on the bias fields, this corresponds to *in situ* displacements of the atom cloud by approximately

$$x_0^{labX} \approx 100\mu\text{m}, \; x_0^{labY,labZ} \approx 1\mu\text{m}.$$

These length scales can be quite challenging to measure given the relative stability between the camera and the ODT positions.

As a first modification to this scheme, we can instead wait for a quarter trap period after displacing the atom cloud and releasing it to convert its newfound potential energy into kinetic energy. Finally, releasing the atoms from the trap when its center-of-mass velocity reaches a maximum allows us to scale the signal by a factor of time-of-flight t. The typical *in situ* time-of-flight distance after 20 ms are, using the relation $m\omega^2 x_0^2/2 = mv^2/2$,

$$x_{ToF}^{labX} \approx (2\pi \times 10\text{Hz}) \times 100\mu\text{m} \times 20\text{ms} \approx 125\mu\text{m},$$

$$x_{ToF}^{labY,labZ} \approx (2\pi \times 100\text{Hz}) \times 1\mu\text{m} \times 20\text{ms} \approx 12\mu\text{m},$$

and the time-of-flight is limited by the field of view available on the camera and the atoms falling out of the imaging plane due to gravity. More generally, the scaling of the maximum *in situ* velocity is different from the displacement by a factor of ω_{ODT}, i.e.

$$v_{max} = \frac{2B_{bias}}{B'}\frac{\omega_{mag}^2}{\omega_{ODT}}. \tag{3.11}$$

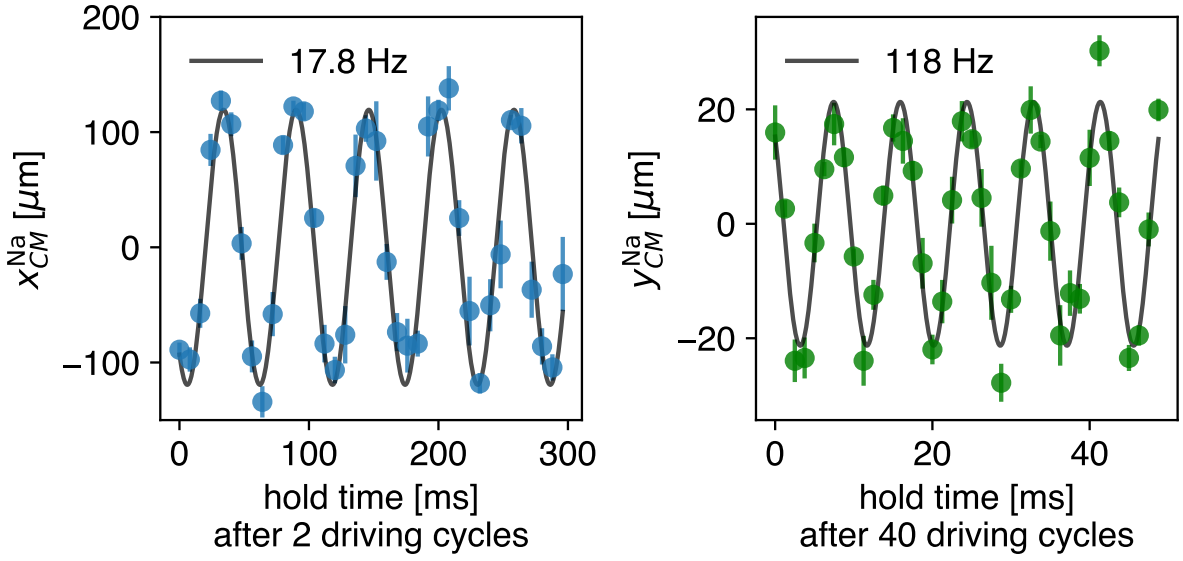

Figure 3.3: Center of mass oscillations are induced by sinusoidally driving a bias field. This data is taken using Na with 20 ms time-of-flight on the z-camera. Credit to Huan Bui for this data.

3.1.3 Measuring trap frequencies

Due to the drift of the alignment of the two crossed ODT beams and the positioning and strength of magnetic fields applied to the atoms, the trap frequencies in experiment can drift on the order of $\sim 2\%$ day-to-day (for example, see the Methods of [65]). Therefore, it is necessary to re-measure them prior to taking publication-quality data, and for accurate measurements one should apply the same magnetic fields used in the experiment.

We follow a two-step procedure to measure trap frequencies. First, we locate the resonance by modulating the strength of the trapping potential sinusoidally in time, i.e., the method of parametric heating. The heating is most efficient when the sinusoidal frequency is $2\omega_0/n$, where n is an integer and ω_0 is the trap frequency (see section 27 of [66]), and this translates to a broadening in the spatial profile of the atoms. In fact, this is the main experimental technique used in our paper measuring collective oscillations in a Bose-Fermi mixture [65].

This first step allows us to roughly locate the resonance positions, but has several drawbacks. When using the parametric heating method with a bosonic species, a nonzero condensate fraction can systematically bias the measurement, since its collective motion will have resonance frequencies dictated by hydrodynamics, which are different from the single-particle resonance frequencies. Additionally, to increase the cloud width (e.g., for better signal-to-noise), it is tempting to drive the parametric resonance in a non-perturbative manner to substantially heat up the ensemble. Since a strong drive pushes the atoms further from the region they typically occupy during an experiment, the anharmonicity in the trapping potential is a second factor that can bias the measurement. Finally, the lineshape of this spectrum will depend on the details of the implementation, e.g., whether number of driving

cycles or duration is held constant as the frequency is varied.

These pitfalls are mitigated by the second step of our procedure, where we induce center-of-mass oscillations in the trapping potential we wish to characterize. As discussed previously, the modulation of the bias fields in xy-plane (lab coordinates) and the the gradient field along the z-axis will displace the center of the trapping potential in each of these axes, respectively. However, there can also be undesired cross-coupling, e.g. we previously observed that modulating the gradient field can also induce motion in the xy-plane. We speculate that this is due to an unintentional misalignment between the optical trapping potential and the geometric center of the magnetic field coils. We find that a simple linear ramping down of the gradient field and jumping it back to its original setpoint is sufficient to displace the atoms far enough to induce measurable oscillations along z. Meanwhile, in the xy-plane we find that a near-resonant sinusoidal modulation of the bias field (of up to 40 cycles! see section 3.1.2 for an explanation) is necessary. We show the observed center-of-mass motion using this method in figure 3.3.

Even with the more precise method of inducing center-of-mass oscillations, there a few technical points to be aware of due to the approximate degeneracy of the y, z (lab) axes. Particularly with a non-resonant drive such as a using simple linear ramp or step waveform, it is possible to excite motion in all three axes. The relative angle between the camera's chip orientation and imaging axes to the eigenaxes of the trap furthermore means that beating will be present when analyzing the motion in the axes defined by the camera.

3.2 Rf and microwave spectroscopy

In this section, we will go over how we use rf and microwave drives to manipulate the internal states of atoms, as well as use atoms to probe the external field. In our experiment, we work at low magnetic fields ($\lessapprox 120$ G), where the total angular momentum F and its component along the magnetic bias field m_F are approximately good quantum numbers.

3.2.1 Spin state initialization at ~ 4 G

We prepare the internal states of the atoms so that they are in their respective ground hyperfine states after transferring atoms from the magnetic trap to the crossed ODT. For robustness, we use adiabatic sweeps rather than precisely timed pulses.

In section 4.3.1 of thesis [28], Wu goes over the key ingredients for performing and verifying high fidelity spin state preparation, as it was originally set up in Fermi1. Due to the ever-evolving capabilities of the experimental apparatus (see Appendix C of [64]), we no longer have the capability to perform "Stern-Gerlach" style imaging looking along the lab-Y axis to verify that the spin state has been prepared as desired.

Instead, we rely on imaging along lab-Z; for both species we can image at either $B \lessapprox 10$ G (applied using the bias field coils) or $B \gtrapprox 65$G (applied using the water-cooled Feshbach coils)[4]. For Na, both the successfully initialized atoms in $F = 2, m_F = 2$ and the "stragglers" in $F = 1, m_F = 1$ can be imaged at either choice of field. For ^{40}K, we make eight transitions

[4]We also note that the bias field coils and Feshbach coils both impart a field along lab-Z, but the fields point in opposite directions, which makes setting up the waveplates for imaging a bit tricky!

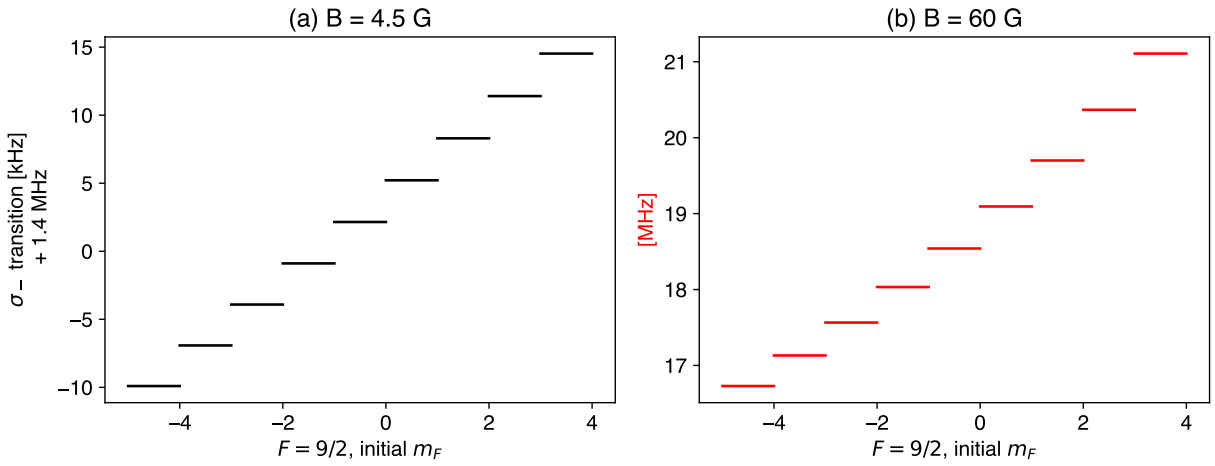

Figure 3.4: We show the frequencies of the nine σ_- transitions crossed to transfer from $m_F = 9/2$ (magnetically trappable) to $-9/2$ (hyperfine ground state) in the $F = 9/2$ electronic ground state hyperfine manifold. At 4.5 G (the status quo, shown in figure a), the transitions are resolved by < 5 kHz, whereas at 60 G the transitions are resolved by > 400 kHz.

within the $F = 9/2$ ground state hyperfine manifold, from $m_F = 9/2$ to $-9/2$. We have successfully set up imaging of $m_F = 9/2$ at $B \approx 10$ G and $m_F = -9/2$ at $B \gtrapprox 65$ G. However, we note that without sympathetic cooling of ^{40}K using Na, the ^{40}K is too dilute to detect by eye in the images, which adds additional dependencies when testing that the K loading and spin preparation is working properly.

^{40}K $F = 9/2$, from $m_F = 9/2$ all the way to $m_F = -9/2$

High fidelity spin preparation of ^{40}K requires driving across nine σ_- transitions. The multiplicative scaling of the total fidelity with number of transitions makes this a challenging task. This is, however, only one difficulty, another is that at $B \approx 4$ G, the quadratic part of the Zeeman shift splitting the nine states is small, and therefore the transition frequencies between states on the Zeeman "ladder" are nearly degenerate, spaced by ~ 5 kHz. This is shown graphically in figure 3.4a. While Doppler broadening is not the limiting factor in resolving these transitions, this introduces the difficulty that it is possible to use too large a Rabi frequency for the adiabatic sweep(s). For a two-level system with a single transition frequency, increasing the Rabi frequency typically improves the fidelity, but for us this can be detrimental due to unwanted driving of the undesired σ_+ transitions[5], driving the atoms back up the ladder of spin states. This is shown in figure 3.5, and could perhaps be mititgated by performing spin transfer at a stronger bias field (see figure 3.4b).

Shelving ^{40}K from $F = 9/2 \rightarrow 7/2$

Infidelity in the spin transfer results in unwanted, non-negligible spin population in $F = 9/2, m_F = -7/2$. Since this state is often later used for either science, calibrations, or

[5]since the rf polarization is most likely not pure

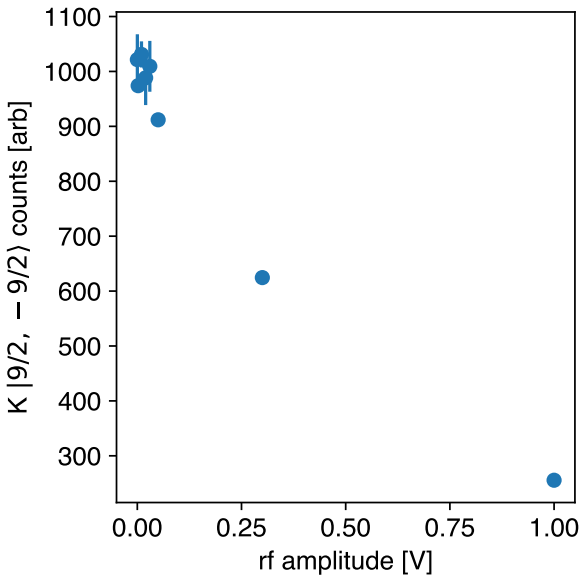

Figure 3.5: Number of K atoms (arbitrary units) successfully transferred to the state $|F = 9/2, m_F = -9/2\rangle$ vs amplitude of the chirped rf pulse. This is a case where more power used for an adiabatic drive is worse!

Feshbach molecule association later on, it is necessary to remove any population there. This is done by shelving them away, into $F = 7/2, m_F = -5/2$ with a 30 ms adiabatic microwave σ_+ pulse chirped over 1.446 7 GHz $\pm$400 kHz at an external magnetic field of ≈ 81 G after sympathetic evaporation in the ODT, shown in figure 3.6. We then presume that atoms in the "shelf" state do not strongly affect downstream procedures/physics, although we do not currently have the capability to remove them from the trap and experimentally verify this statement.

^{23}Na $F = 2, m_F = 2 \rightarrow F = 1, m_F = 1$

In contrast to the procedure described previously for ^{40}K, our Na spin preparation consists of driving only the $F = 2, m_F = 2 \rightarrow F = 1, m_F = 1$ transition. This was previously done by shining on a microwave with static frequency ≈ 1.8 GHz and ramping a time-varying external B-field through the resonance condition. Though this method does successfully transfer the atoms into the desired spin state, applying a bias field can have unintuitive/undesired mechanical effects, as discussed in section 3.1.2. Residual magnetic gradient fields that linger and spatial in-homogeneity in the bias field cause this ramp to have a side-effect of exciting a sloshing motion of the atoms, as seen in figure 3.7. This is undesirable as the ensemble center-of-mass motion eventually damps out due to anharmonicity of the trap and effectively heats the atoms.

After upgrading of our microwave source to a DDS-based oscillator that supports "phase-continuous" frequency sweeps[6], we were able to test the alternate approach of applying a

[6]credit to Carter Turnbaugh and Yiming Zhang for implementing this

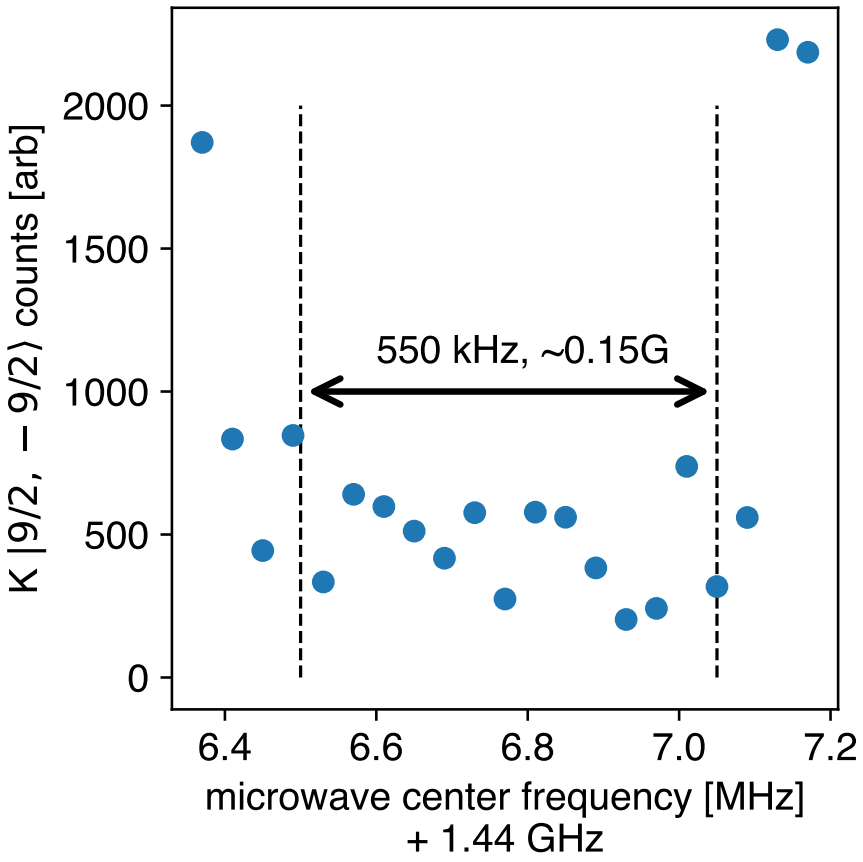

Figure 3.6: Number of K atoms (arb) remaining in $|F = 9/2, m_F = -7/2\rangle$ after the cleanout microwave pulse to $|F = 7/2, m_F = -5/2\rangle$ is applied. The width of this spectral feature protects against drift of ~ 0.15 G in the external field. Credit to Huan Bui for taking this data.

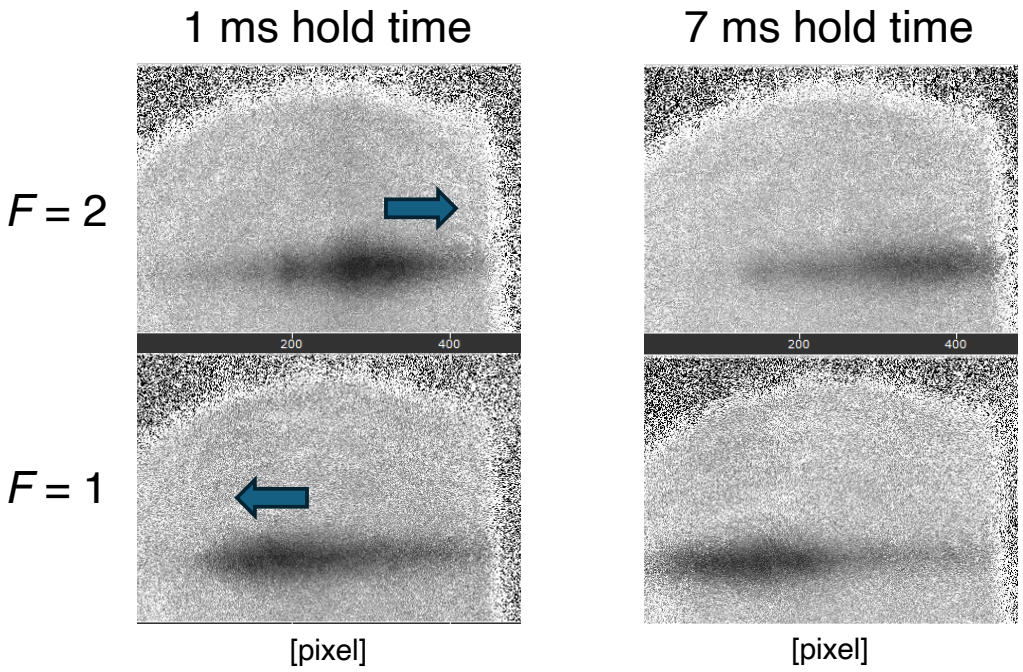

Figure 3.7: Absorption images taken with the z-camera, of Na $|F = 2, m_F = 2\rangle$ and $|F = 1, m_F = 1\rangle$ states, after a linear magnetic field ramp in time and variable hold time in the optical trap, as typical for Na spin preparation. The microwave pulse is deliberately set such that we have substantial population in both states. The sign of the force (schematically shown by the blue arrows) imparted on the atoms is spin-dependent, reminiscent of the famous Stern-Gerlach experiment.

static external bias field and sweeping the frequency instead. We observed experimentally that this approach appears to be more robust against drifts in the resonance condition, as shown in figure 3.8. Separately, combined with the addition of waiting for the residual magnetic trapping fields to decay, our new procedure largely eliminates inducing the unwanted sloshing of atoms.

3.2.2 Measuring the "science" bias field

We characterize the applied magnetic field at the location of the atoms by using K atoms themselves as a probe. This is a critical measurement, since our position in the Feshbach resonance landscape will determine the binding energies measured in Chapters 4, 5. The measured rf transition frequency along with the prior knowledge of the K hyperfine structure in an external field allows us to infer the magnitude of the B-field. For example, see the rf spectrum taken in figure 3.9a. By using a pure spin-polarized sample of fermions (rather than Na or an Na-K mixture), we avoid systematic biases of the measurement due to so-called "clock" shifts. See [67] for an experimental demonstration of this effect.

The external magnetic field is stabilized using closed-loop feedback on the measured current in the Feshbach coils (rather than, for example, the measured magnetic field near the chamber), as described in [28]. Therefore, other undesired sources of magnetic fields, for example 60 Hz oscillations due to the power line or eddy currents near the atoms, are not actively cancelled. For measurements much shorter than the 16 ms period, we can synchronize experimental repetitions with the power line to remove the corresponding noise in our measurements. However, certain experiments, such as the one discussed in Chapter 4, require measurement times of much longer than 16 ms. To characterize the fluctuations of the B-field due to the power line, we can take multiple rf spectra (using pulse lengths much shorter than 16 ms) synchronized with it, but with variable delay time to sample over the 16 ms period. A less data intensive variation of this idea is to instead fix the applied rf frequency where the population transfer is most sensitive to fluctuations in magnetic field, as shown in figure 3.9b. From the observed fluctuations, we conclude that the power line contributes fluctuations of < 5 mG on top of ~ 100 G.

We believe that the magnetic field stability in our experiment is one of the limiting factors in the coherence times of driving rf transitions. For example, we drive Rabi oscillations in initially spin-polarized K atoms and find a decay time of a few ms, as shown in figure 3.10. We have not experimentally confirmed temporal fluctuations in the B-field as the sole cause; for example, spatial inhomogeneities in both the static field and the rf driving field can also contribute to the decay of coherent oscillations. However, even with a coherence time of a few ms, we find that for spectra taken with long pulses still provide an experimental resolution of ~ 5 kHz FWHM, as shown in figure 3.11.

Bias field controls (and limitations)

For the purpose of future improvements, we will conclude with a few miscellaneous technical tidbits about the current B-field control system.

- It takes $\sim$ 20 ms for the magnetic field at the atoms to completely stabilize after jumping the setpoint of the field. That is, after waiting $\sim$ 20 ms, our measurements

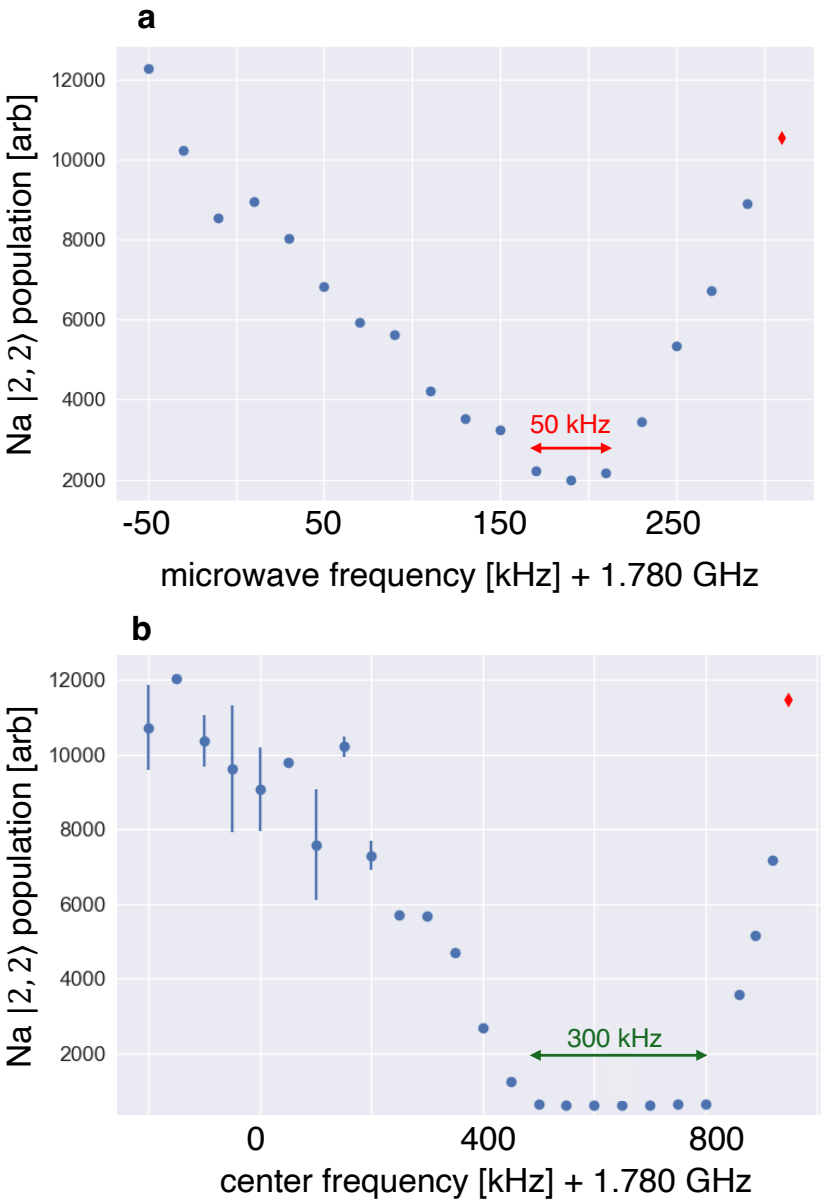

Figure 3.8: Number of Na atoms (arbitrary units) remaining in $|F = 2, m_F = 2\rangle$ after applying the spin transfer microwave pulse to $|F = 1, m_F = 1\rangle$. Using the same pulse durations, we take spectra as a function of (a) static microwave frequency and time-varying bias field or (b) center frequency of the chirped pulse, and find a significant improvement in the window of stability (from $\sim$ 50 kHz window to $\sim$ 300 kHz) using the latter method. I share credit with Huan Bui for taking this data.

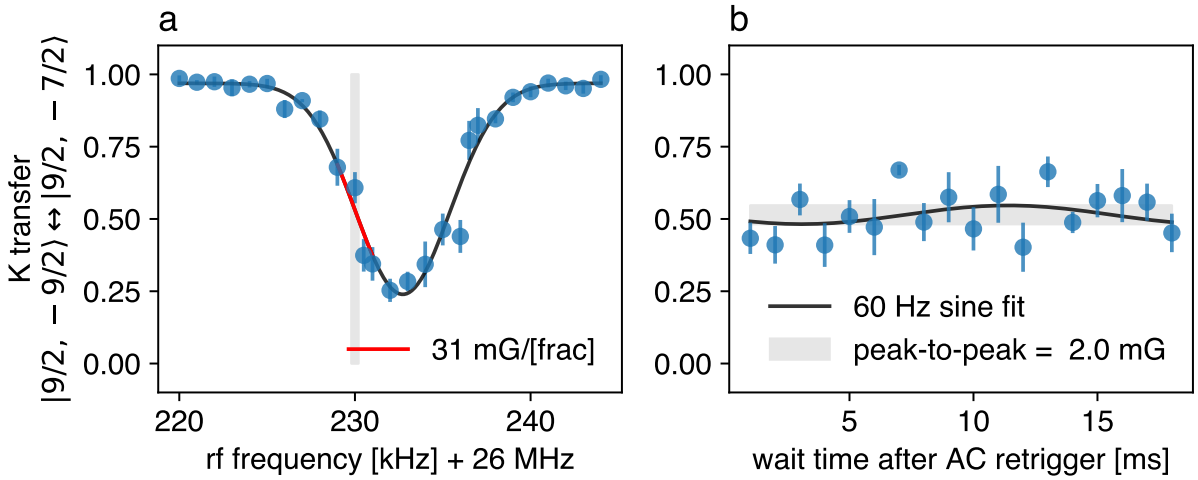

Figure 3.9: The fractional K atom population remaining in $m_F = -9/2$ after driving the transition to $m_F = -7/2$ within $F = 9/2$ with a 240 μs (approximately 3π) Blackman pulse applying an external magnetic field of $B = 101$ G. (a) Spectrum taken with varying rf drive frequency. (b) A measurement of the transfer with varying wait time after synchronizing to the power line, using a fixed drive frequency of 26.230 MHz, where the sensitivity is 31 mG/[fraction].

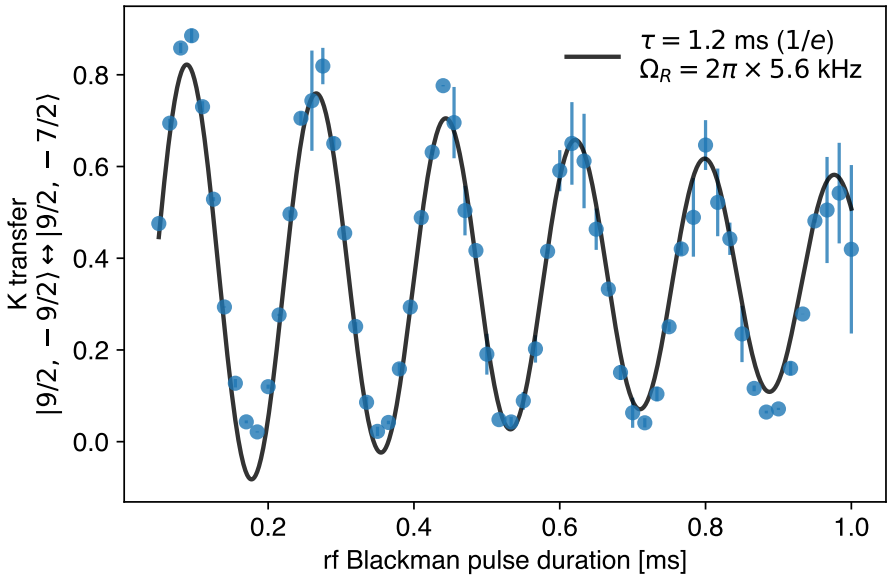

Figure 3.10: We drive Rabi oscillations between $F = 9/2, m_F = -9/2 \leftrightarrow -7/2$ in K atoms. We find a $1/e$ coherence time of ~ 1.2 ms by fitting to an exponentially decaying sinusoid function. Credit to Huan Bui for taking this data.

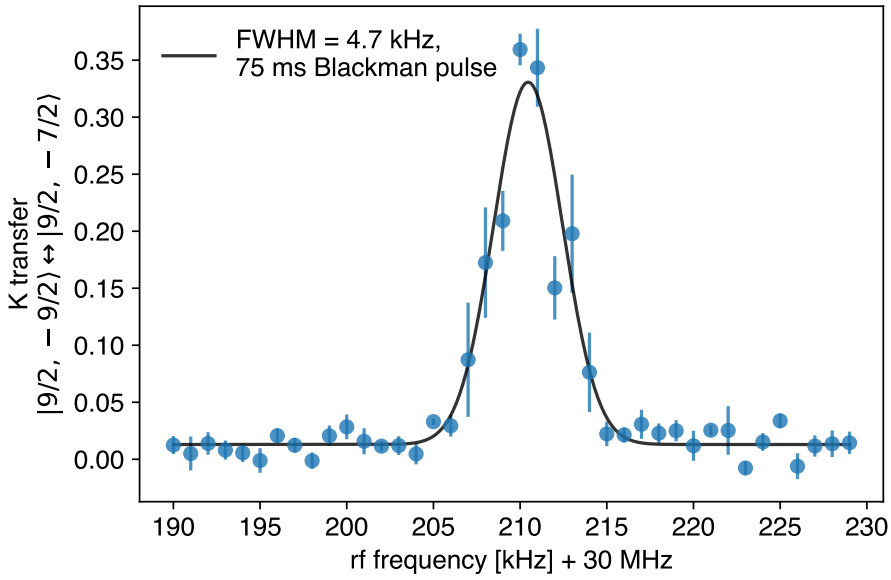

Figure 3.11: Rf spectroscopy of the $F = 9/2, m_F = -9/2 \leftrightarrow -7/2$ transition in K atoms, using a 75 ms pulse with $B = 120$ G. Using pulses ~ 100 ms is typical of the experiments discussed in Chapter 4. We find a 4.7 kHz FWHM, fitting to a Gaussian lineshape. Given the measured coherence time in our system, we theoretically expect a peak transfer of 0.5, corresponding to a fully mixed state. However, our measurements deviate from this due to imaging artifacts that affect $m_F = -9/2$ and $-7/2$ populations differently.

using rf spectroscopy indicate that additional waiting time does not change the position or width of the spectrum measured.

- Our experience shows significant discrepancies between the B-field measured at the atoms (using rf spectroscopy measurements) and the Hall probe measuring the current flowing through the coils (the signal that we use for feedback), particularly in ramps of < 1 ms. This makes considerable guesswork and manual fine-tuning of the current setpoint waveform necessary for precise ramps and jumps of the B-field, which is necessary when performing rf or microwave quantum state manipulations such as shelving, removal, etc.

- The realized B-field using the Feshbach coils can drift on the order of 10 mG from day to day despite using a constant setpoint, so in setting up any state manipulations that rely on the stability of this field should take this into account, such as rf association of Feshbach molecules, spin state preparations, etc.

Chapter 4

Two- and three-body molecule formation in a dilute mixture

The contents of this chapter include material copied verbatim from the manuscript in preparation,

> Alexander Chuang*, Huan Bui*, Arthur Christianen*, Yiming Zhang, Yiqi Ni, Denise Ahmed-Braun, Carsten Robens, Martin W. Zwierlein (2024). Observation of a Halo Trimer in an Ultracold Bose-Fermi Mixture.

This work is a collaboration between the experimental team at MIT and theorists Arthur Christianen and Denise Ahmed-Braun.

4.1 Introduction

Three-body bound states in quantum mechanics have a rich history, from the molecular hydrogen ion [68], [69], the nuclei of tritium and ^{3}He [70], [71], to the helium trimer [72], [73]. The three-body problem is of fundamental theoretical interest, since it displays phenomena which are markedly different from the physics of just two particles. For pure contact interactions, Thomas predicted a collapse [74], as the effective potential, an inverse square law in the hyperradius, supports infinitely deep bound states. Efimov studied particles in the regime of large two-body scattering lengths, and found a universal "staircase" of trimer bound states, characterized by a constant ratio between successive energy levels [44].

Efimov's scenario, originally proposed for nuclear physics, was studied in detail both experimentally and theoretically in the field of ultracold gases [75]. Efimov states were first observed in a gas of identical bosonic cesium [76], and later several successive states were demonstrated [77]–[80]. The majority of observations were via particle loss at particular values of the scattering length. Exceptions are studies of three distinguishbable fermions of ^{6}Li, where Efimov states were directly observed in radiofrequency (rf) spectra [81], [82], allowing the determination of binding energies.

The properties of the Efimov trimers greatly depend on the relative masses of the involved particles, especially when not all mutual two-body interactions are large [75]. For one light atom interacting with two heavy ones the Efimov effect becomes more prominent, and the

excited Efimov states become easier to observe [79], [80]. For the opposite heavy-light-light combination which we study here true Efimov states only appear exceedingly close to unitarity. However, we show that this does not preclude the formation of a single weakly bound "halo" trimer [83], which may still have some universal properties.

In this work, we directly observe such a halo trimer bound state using rf-spectroscopy as illustrated in Fig. 4.1. The trimer is formed by two light ^{23}Na-bosons surrounding a heavy "impurity" atom, fermionic ^{40}K. The fermion interacts resonantly with the bosons near a Feshbach resonance, with scattering length a, while the bosons weakly repel each other (Bose-Bose scattering length $a_{\mathrm{BB}} = 56.5a_0$, based on [84]).

We may understand the existence of this weakly bound trimer state by first considering the extreme limit of an infinitely heavy impurity. For positive scattering length, a dimer

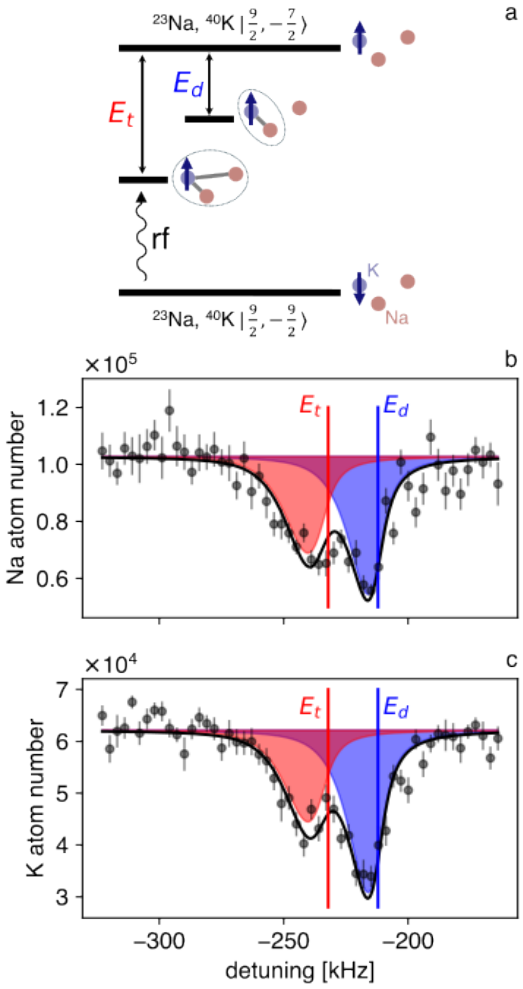

Figure 4.1: (a) Rf spectroscopy of free-to-bound transitions into Na-K dimer and Na_2-K trimer states with binding energies E_d, E_t, respectively, red-detuned from the bare atomic hyperfine transition. (b-c) Depletion spectra taken at 101.8 G, where losses due to resonant coupling to the dimer state and trimer state are present in (b) Na and (c) K. The underlying dimer and trimer fitted lineshapes are shown as blue and red shaded regions, respectively, with solid lines marking the binding energies and solid curves showing the summed lineshape.

bound-state exists at energy E_d. In the absence of interactions between the light bosons, the impurity simply acts as an external potential in which both bosons can occupy the same energy level, giving this trimer a binding energy of $2E_d$. When bosons instead repel at short range, they cannot simultaneously occupy the bound state and the trimer energy is suppressed. Universal properties of trimers and larger clusters in this scenario have been studied in Refs. [85], [86] for an effective three-body repulsion, finding that a universal trimer state always persists at least for near-unitary interactions.

In our case, the fermionic ^{40}K atom, is only about twice heavier than the bosons, but in combination with the modest interboson repulsion, this mass imbalance is enough to yield a scenario qualitatively similar to the infinite mass case. The trimer bound state we observe has an energy close to E_d, implying that the second boson is, on average, found significantly further away from the heavy atom than the first. We can reproduce the measured binding energy curve of the trimer theoretically.

In section 4.2 we will first layout the experimental methodology and the experimental evidence for the observation of the trimer state. In Sec. 4.3 we then move on to discuss the properties of the trimer state, such as lineshape, energy and wave function, based on both experimental and theoretical analyses. After discussing in more detail the relevant loss processes and the relative dimer-trimer signal strengths (Sec. 4.4), we will conclude our work in Sec. 4.11.

4.2 Experimental observations

We prepare a Bose-Fermi mixture of ^{23}Na and ^{40}K, trapped in an optical dipole trap with Na trapping frequencies $2\pi\times(18, 118, 125)$ Hz in their respective hyperfine ground states $|F = 1, m_F = 1\rangle_{\mathrm{Na}}$ and $|F = 9/2, m_F = -9/2\rangle_{\mathrm{K}} \equiv |\downarrow\rangle_{\mathrm{K}}$, with typical initial peak ^{23}Na densities of 0.4 – 0.88 μm^{-3} and ^{40}K densities of 1.1 – 2.4 μm^{-3}. To probe the few-body bound states of interest minimizing many-body effects in our system, we prepare the mixture in the non-degenerate regime at $\approx$200 nK. Thus for our densities we have $T/T_C \sim 1.4 - 1.8$ and $T/T_F \sim 0.7 - 0.9$. The ratio of atom numbers is comparable so that we are able to observe the creation and subsequent loss of molecules in the population depletion of both species.

To measure the binding energies of the NaK dimer and Na_2K trimer states, we perform rf association spectroscopy by driving a free-to-bound hyperfine transition of K, from $|\downarrow\rangle_{\mathrm{K}}$ to $|\uparrow\rangle_{\mathrm{K}} \equiv |F = 9/2, m_F = -7/2\rangle_{\mathrm{K}}$, in the presence of Na, as shown schematically in Fig. 4.1a. We work near a broad interspecies Feshbach resonance at $\sim$ 110G between $|F = 1, m_F = 1\rangle_{\mathrm{Na}}$ and the final state $|\uparrow\rangle_{\mathrm{K}}$ by applying magnetic fields from 100.5 to 105 G (see Fig. 4.3). This allows us to measure the trimer binding energies as it tracks the dimer, over an order of magnitude. We then probe the transitions by a variable-frequency rf driving pulse. For the typical spectra, as shown in Figs. 4.2 and 4.8, we use a Blackman rf-pulse with a window-averaged Rabi frequency of $\Omega_{\mathrm{rf}} \sim 2\pi \times 5$ kHz on the bare atomic transition. Subsequently, we detect the populations of Na and the two spin states of K using resonant absorption imaging. For the rf pulse, we choose a variable duration between 3 and 250 ms, such that at least $\approx$ 30% of the initial state populations remains. Strong losses in the initial state populations indicate the presence of resonant rf coupling to a bound state.

We note that the initial interspecies interaction is large and negative, varying from -1400

to $-1100a_0$ over the range of magnetic fields we apply. The interspecies attraction enhances the wavefunction overlap to the final bound states of interest.

A compilation of rf depletion spectra for varying magnetic field is shown in Fig. 4.2, where from top to bottom the Feshbach resonance is approached. In all of the spectra, the presence of the trimer state is clearly established by the double-peak structure of the rf-association feature. In fact, the trimer feature has comparable weight to the dimer peak for the whole range of magnetic fields, which is surprising since this trimer feature has not been observed before. The relative peak weights as a function of magnetic field are shown in Fig. 4.4a). We find that the trimer weight substantially increases as the resonance is approached. We will address these relative weights further in Sec. 4.4.

To fully understand our spectra, and to unambiguously establish the different nature of

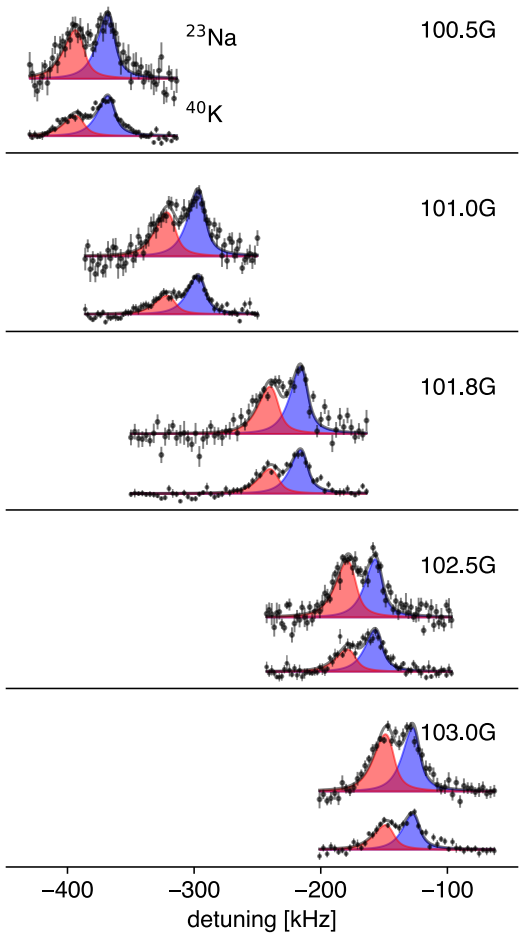

Figure 4.2: Depletion spectra of Na (K), shown as the upper (lower) trace within each panel with square (circle) markers, taken at B-fields between 100.5 and 103G, in proximity to the Feshbach resonance at 110G. The trimer feature (red shaded) closely tracks the dimer (blue shaded) in all datasets. Error bars show the standard error on the mean, for 7-15 repetitions taken per point. Due to atom number variations in sample preparation between datasets, the initial Na : K ratios prior to application of the rf pulse vary from $N_0^{\mathrm{K}}/N_0^{\mathrm{Na}} = 0.3 - 0.65$.

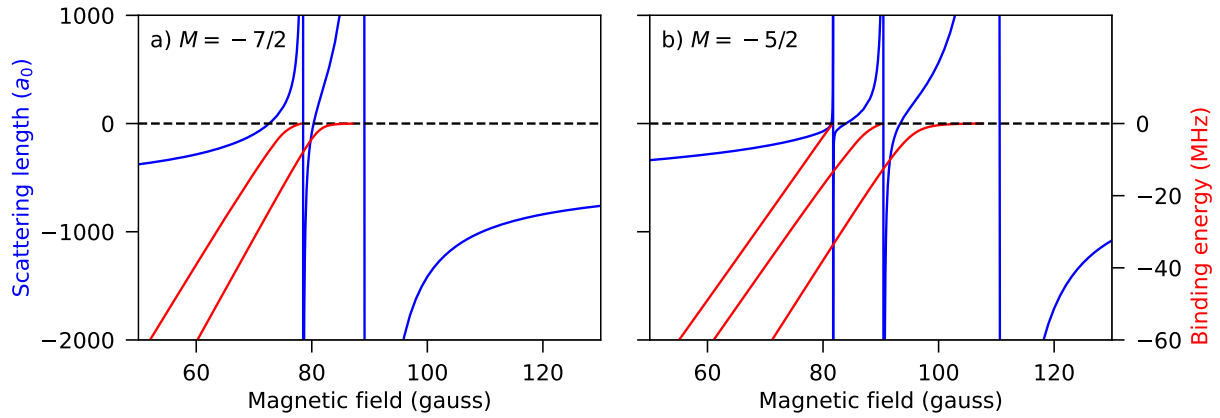

Figure 4.3: Scattering length (blue, in a_0) and binding energies (red, in MHz) of ^{23}Na and ^{40}K as a function of magnetic field. For ^{23}Na the internal state is $|F = 1, m_F = 1\rangle$, for ^{40}K the internal state is a) $|F = 9/2, m_F = -9/2\rangle$ and b) $|F = 9/2, m_F = -7/2\rangle$. The M in the figure is the total magnetic quantum number in the collision, which is conserved. The curves are based on coupled-channels calculations with the Na-K interaction potentials from [87].

the dimer and trimer peaks, we need to consider not only the rf association processes but also possible loss processes. Indeed, without loss of the dimer and trimer populations, the signal detected in the Na imaging channel should remain unchanged. This is because our Na imaging probe is equally sensitive to the initial atom population as to the dimer and trimer populations, since first, rf association preserves the hyperfine state of Na, and second, the dimer and trimer states are weakly bound. This allows the near-resonant Na imaging light to scatter and dissociate the molecules.

The observed depletion of the Na-atoms can be attributed to three-body loss processes: the relaxation of Feshbach dimers into a deeper rovibrational state upon collision or interaction with a third atom. The excess energy is released as kinetic energy, leading to the ejection of both the atom and the molecule from the trap. For trimers this process can happen internally, leading to relaxation into a deeply bound dimer and free atom ($Na_2K \rightarrow NaK + Na$). This is consistent with our observation that the association and decay of trimers depletes the Na and K initial populations in a $2:1$ ratio, as shown in Fig. 4.4b). In contrast, the dimers can be lost through dimer-atom collisions with free atoms of either species (NaK-K and NaK-Na collisions). The presence of these two loss mechanisms, with $2:1$ and $1:2$ ratios for Na to K depletion, respectively, is also consistent with our observation that the production of dimers leads to a depletion ratio $< 2:1$ of initial Na and K populations. The loss dynamics is discussed in more detail in Sec. 4.4.

The different loss dynamics between dimers and trimers is most striking near the Feshbach resonance. We show an example of this at $B = 105$ G in Fig. 4.5. Here we see both the dimer and trimer features with roughly equal weights in the K depletion, whereas in Na we see a strong suppression of losses near the dimer resonance, indicating a lower rate of dimer-Na collisional loss. A consequence of the longer dimer lifetime is that we are now able to directly detect the surviving dimers, as shown in Fig. 4.5c. Experimentally, this is realized by applying a square-envelope rf pulse of duration comparable to the decay time of

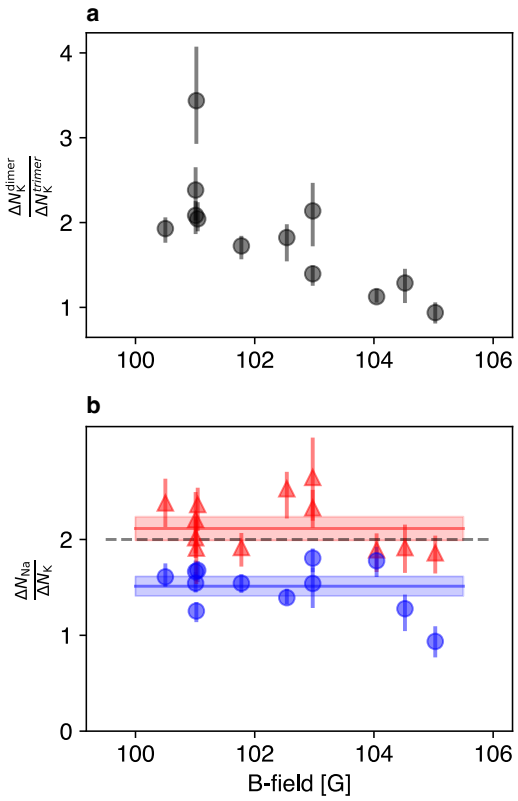

Figure 4.4: (a) The ratio between the fitted trimer and dimer feature heights, in the K spectra. For both plots, error bars on the data points indicate 68% confidence intervals, as found by bootstrapping. (b) The intraspecies ratio of the fitted trimer (red triangles) and dimer (blue circles) peak depletions vs applied magnetic field. The trimer data clusters around 2 : 1 Na-K loss ratio, whereas the dimer data lies between 1 : 1 and 2 : 1. The solid lines (shaded regions) show the weighted mean and standard deviation of the estimated ratios, across magnetic fields.

the dimers. The trimers are notably still absent, due to their much shorter lifetimes.

Our measurement of the surviving dimer population after applying the rf pulse allows us to bound its $1/e$ decay time at $\gtrapprox 1.4$ ms. We cannot detect any arrival signal on the trimer feature within our accessible experimental parameter space and our signal-to-noise (SNR), and therefore provide only bounds of the trimer's $1/e$ lifetime. The length of our pulse and SNR provides an upper bound of $\sim$1 ms. By attributing the entire convolution kernel width used in the fitting functions to lifetime broadening, we can provide a lower bound of $\sim$20 μs. This is likely to be an underestimate of the lifetime however, since there are known factors such as technical noise that also contribute to broadening.

The notable absence of any detectable signal of surviving trimers clearly shows that the intrinsic trimer decay mechanism occurs on a much shorter timescale than the decay of dimers for our experimental parameters. This marked difference in their lifetimes, along with their different binding energies and Na/K loss ratios, are three physical features that allow us to clearly distinguish between the products (dimer and trimer) created in our rf

association procedure.

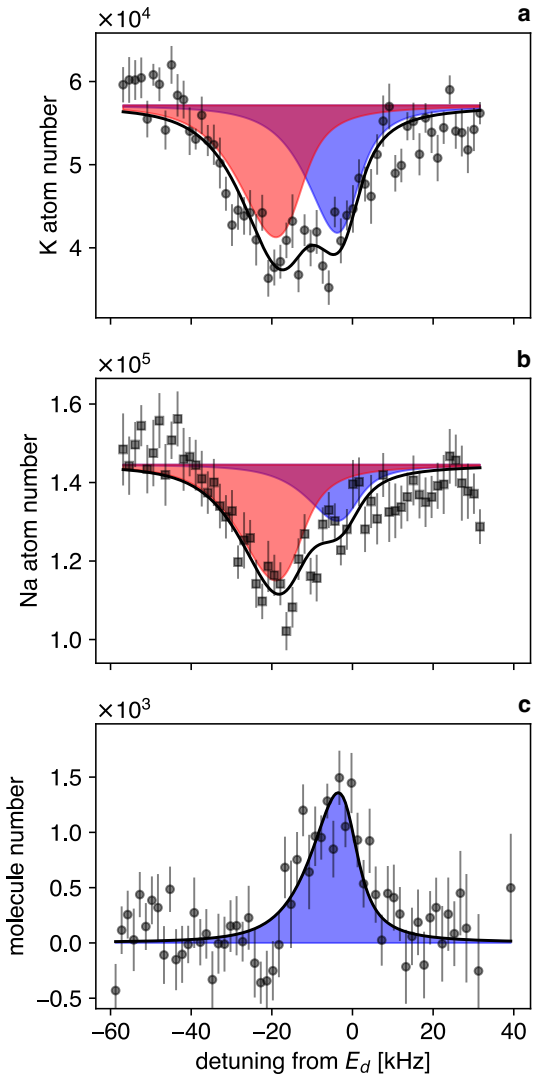

Figure 4.5: (a-b) Depletion spectra taken with a 30 ms Blackman-envelope rf pulse, at $B = 105$ G. The loss in Na population on the dimer feature is strongly suppressed here. (c) A spectrum taken by applying a shorter 3 ms square pulse, with pulse parameters chosen to observe the arriving dimer and trimer populations in the final state $|\downarrow\rangle_{\mathrm{K}}$. There is only one spectral feature here, with the trimer arrivals being noticeably absent, due to their short intrinsic lifetime relative to the rf pulse duration.

4.3 Trimer properties

4.3.1 Lineshapes

Having established the existence of the halo trimer, we move on to study its properties. To extract the dimer and trimer binding energies from the data, a good knowledge of the dimer and trimer lineshapes is required. Previously, the trimer lineshapes were fitted using phenomenological fit functions such as Lorentzian or Gaussian lineshapes [81], [82]. Here we attempt to extract the energy more accurately by employing lineshapes based on theoretical modeling. The total lineshape of the rf-association feature can be modeled as the weighted sum of the dimer and trimer lines. Both lines are intrinsically asymmetric due to the finite temperature and the free-to-bound nature of the rf-transition.

In a thermal gas, the dimer lineshape as a function of energy E in the universal limit is well known [88] and given by

$$F_d(E_d - E) \sim \frac{2}{\pi} \frac{k\kappa_d(1-\kappa_d a_i)^2}{(k^2+\kappa_d^2)^2(a_i^2k^2+1)} \exp\left(-\frac{E}{k_B T}\right), \tag{4.1}$$

where $E = \frac{k^2}{2\mu_{\mathrm{NaK}}}$ for relative momentum Na-K k in the initial state, and $E_d = -\frac{\kappa_d^2}{2\mu_{\mathrm{NaK}}}$ is the dimer energy with the associated wave vector κ_d. We further use the initial scattering length a_i, temperature T and the Na-K reduced mass μ_{NaK} .

The trimer lineshape cannot be captured in a simple analytical form, but the low-energy threshold behavior can be deduced straightforwardly. Let us first briefly revisit the dimer case. The two-particle s-wave scattering wave function $f_d(k,r)$ is given by

$$f_d(k,r) = \sqrt{\frac{2\mu_{\mathrm{NaK}}}{\pi\hbar^2 k}} \sin(kr + \delta_k), \tag{4.2}$$

where r is the interparticle distance and δ_k is the phase shift, which for short-range interactions is given by

$$\lim_{k\to 0} k\cot(\delta_k) = -\frac{1}{a} + \frac{r_{\mathrm{eff}}k^2}{2} + \mathcal{O}(k^4). \tag{4.3}$$

for effective range r_{eff}. Importantly, δ_k is linear in k for small k. If we compute the overlap of this function with the localized bound-state wave function ψ_d, we therefore find

$$\lim_{k\to 0} |\int_0^\infty dr \psi_d^*(r) f_d(k,r)|^2 \sim k \sim \sqrt{E}, \tag{4.4}$$

which we recognize from Eq. (4.1). In the experimentally relevant regime, the dimer is strongly bound compared to the initial thermal energy, meaning that this leading-order threshold behavior is the most critical. The momentum-dependence of the denominator in Eq. (4.1) plays a minor role at the experimental temperature, except to set the prefactor of the expression to ensure the correct normalization of the wave function.

To consider the threshold scaling for the trimer wave function we employ the adiabatic hyperspherical approach. One can show that the three-body analog of the s-wave scattering solution is given by

$$f_t(K,R) = \sqrt{\frac{2\mu R}{\hbar^2}}[J_2(KR) - \tan\Delta_K Y_2(KR)], \tag{4.5}$$

where μ is the three-body reduced mass, R and K are the hyperradius and the hyperradial momentum, $J_2(KR)$ and $Y_2(KR)$ are regular and irregular spherical Bessel functions of second order and Δ_K is the three-body phase shift. In the three-body case the threshold law gives that $\tan(\Delta_K) \sim K^4$. Hence, for $KR \to 0$, $f_t(K,R) \sim K^2$. Making a similar argument as in the dimer case, we can show that

$$\lim_{K\to 0} |\int_0^\infty dR \psi_t^*(R) f_t(R)|^2 \sim K^4 \sim E^2. \tag{4.6}$$

The threshold behavior is therefore markedly different from the dimer case, leading to a larger temperature shift of the trimer peak than the dimer peak (in the low temperature limit). The different energy dependence of the trimer lineshape can be understood from a phase-space argument: for the low-energy contributions to the lineshape all the particles in the bound state need to be simultaneously at a small momentum, which is much more unlikely for the trimer than the dimer.

Whereas the dimer is strongly bound compared to the thermal energy scale, this is no longer true for the halo trimer. Here the binding energy of the third atom to the dimer is comparable to the thermal energy. Hence, it is important to consider the leading-order corrections to the threshold scaling. Tscherbul and Rittenhouse [89] derive a trimer lineshape for Efimov states close to the atom-dimer threshold, and for $Ka \ll 1$:

$$F_t(E_t - E) \sim \frac{(2\kappa_t^2 + K^2 - 2\kappa_t\sqrt{\kappa_t^2 + K^2})^2}{K^4} \exp\left(-\frac{E}{k_B T}\right), \tag{4.7}$$

where $E = \frac{K^2}{2\mu}$ and $E_t - E_d = -\frac{\kappa_t^2}{2\mu}$. Here the wave function consists of a dimer plus a weakly bound additional atom, and therefore we would expect a similar lineshape as in the case studied here. We indeed find a good agreement of this lineshape with the lineshape from hyperspherical calculations for the relevant low-energy regime. We do not account for the initial-state scattering length in the lineshape, because it is small compared to the thermal de Broglie wavelength. Therefore the lineshape is not much affected in the experimental regime. Note that this is different for the signal strength which is substantially enhanced for initial-state attraction.

For the final fit function used to approximate the lineshape, we convolve the above-mentioned lineshape with a 8-10 kHz FWHM Lorentzian kernel and observe good agreement with the data, as can be viewed in Figs. 4.1, 4.2, and 4.5. The width of the experimental broadening is comparable to the intrinsic linewidth of the dimer and trimer features. The predominant source of broadening are rapid fluctuations of the applied magnetic field caused by technical noise. However, we note that a separate set of calibration experiments on the bare atomic transition suggests that broadening beyond convolution with a ∼5 kHz FWHM kernel is not directly caused by this technical limitation. This fit model ignores implicitly time-varying quantities over the rf pulse duration such as the remaining population, as well as spatially varying quantities such as the local density, phase space overlap and temperature, all of which are averaged over in our measurements. We further do not explicitly include many-body mean-field shifts of the dimer and trimer lines, which we expect to be of the order of 1-2 kHz.

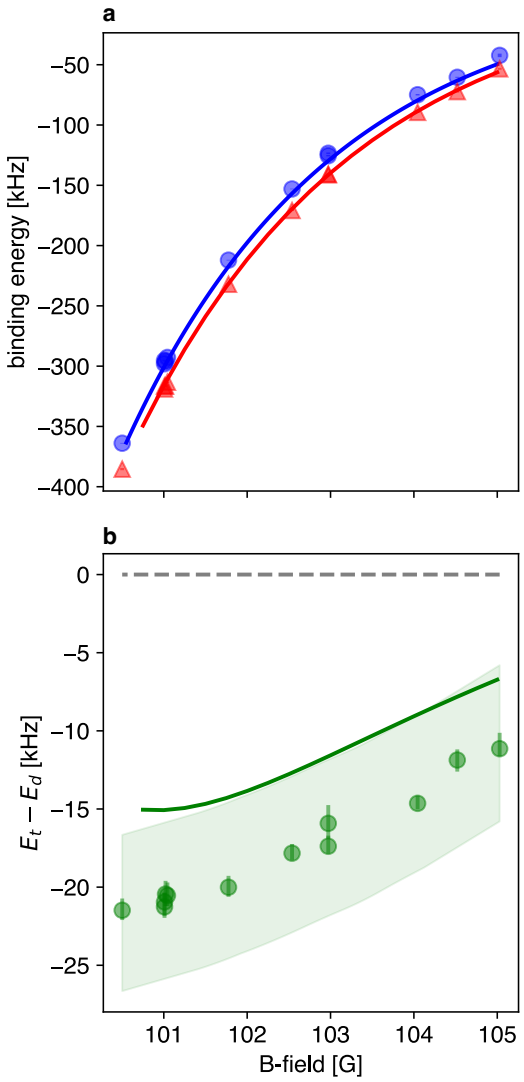

Figure 4.6: (a) The measured binding energies of the dimer (blue) and trimer (red) vs applied magnetic field. Error bars showing 68% confidence intervals are found by bootstrapping and are within the markers. (b) Difference in measured binding energies of the dimer and trimer (green circles) along with the theoretical prediction (solid line). The shaded region shows the FWHM of the Lorentzian convolution kernel used to fit the lineshapes, setting a frequency scale for systematic error of the fit model.

4.3.2 Trimer binding energy

The fitted dimer and trimer binding energies are summarized in Fig. 4.6a. Their spacing, shown in Fig. 4.6b, is a small fraction (5-20%) of the dimer binding energy through all our measurements. This strongly contrasts with the simplified fictitious case discussed in the introduction of a trimer state where an infinitely heavy impurity binds two non-interacting bosons, thus having a binding energy being twice that of the dimer. The impurity having a finite mass only lowers the energy compared to the infinite-mass case, meaning that the

suppression of the trimer energy is predominantly due to the interboson repulsion.

Interestingly, the interboson repulsion does not have to be resonant to suppress the trimer binding energy. In our case the modest interboson repulsion of approximately $56.5a_0$ already has this effect, even though the boson-impurity scattering length is more than an order of magnitude larger. As discussed in Refs. [85], [86] multichannel effects can also give rise to an additional effective repulsion, but this effect is strongest for narrow resonances. Here the same qualitative picture of the trimer state lying slightly below the dimer was predicted. More detailed investigations of multichannel effects for the current system, such as the presence of a virtual bound state and the interplay with the other nearby Feshbach resonance, are left for future work [90].

We theoretically compute the dimer and trimer energies based on input from realistic Na-K and Na-Na interaction potentials [84], [87]. In short, we construct real-space model potentials using Gaussians, which match the scattering length and effective range of the realistic interaction potentials, but which do not contain deep lying bound states. All the parameters are chosen without fitting or matching to the experimental data. We find that for the magnetic fields under consideration, the theoretical dimer energy is accurately represented by the universal expression

$$E_d = -\frac{\hbar^2}{2\mu_{\mathrm{NaK}} r_{\mathrm{eff}}^2}\left(1 - \sqrt{1 - \frac{r_{\mathrm{eff}}}{a}}\right)^2, \tag{4.8}$$

where a and r_{eff} both depend on B. The next order correction is about 1 kHz at B=100G, and substantially smaller closer to the resonance.

The theoretical dimer and trimer energies are plotted along the experimental data in Fig. 4.6a and 4.6b. From Fig. 4.6a we see that the theoretical dimer and trimer energies agree with the experimental results up to 5-10 kHz. However, in the difference plot we see that the theoretical dimer-trimer splitting is clearly smaller than the experimentally extracted result. Since the absolute difference is on the order of 5 kHz, which is smaller than the experimental linewidth, there is a variety of explanations for this difference.

One particular effect we have not considered in the lineshape is the many-body energy shifts of the lines. Due to the shallow trimer state, the atom-dimer scattering length is large and positive, which should lead to a shift of the dimer line to smaller binding energies. In turn, the atom-trimer scattering length is most likely either large and negative or large and positive. If it is large and negative this will lead to a downshift of the trimer line, if it is large and positive it leads to the formation of bound states with more particles which we do not resolve. However, these would also lie lower in energy than the trimer, leading to a downshift of the measured line. Consequently, we expect these many-body effect to be responsible for an increase in the dimer-trimer splitting fitted from the experimental data on the order of a few kHz as compared to the theoretically computed (few-body) trimer energy.

Other effects, such as saturation, also have the tendency to increase the observed dimer-trimer splitting. Taking this into consideration, the theoretical results are consistent with the experiment.

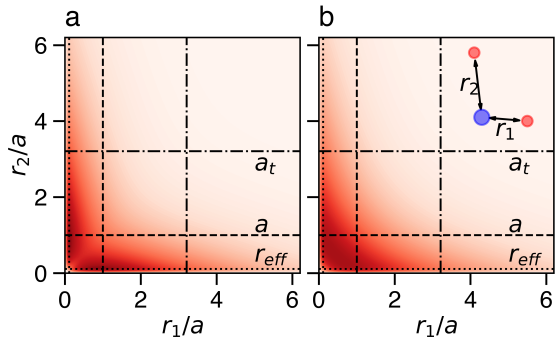

Figure 4.7: The trimer wavefunction amplitude as a function of the two Na-K distances r_1/a and r_2/a at $B = 103$ G in units of the scattering length. a) shows the full numerical wave function, b) shows the result of the model from Eq. 4.9. The horizontal and vertical lines show the relevant length scales in the model, the Na-K scattering length a (dashed), the trimer size $a_t = 1/\kappa_t$ (dash-dotted) and the Na-K effective range $r_{\rm eff}$ (dotted).

4.3.3 Trimer structure

Since the theoretical trimer energy is consistent with the experiment, we can use the theoretical model to further analyze the internal structure of the trimer, as shown in Fig. 4.7a). This figure shows the numerical trimer wave function for the magnetic field of 103 G as a function of the two Na-K distances r_1 and r_2. From the plot is is clear that the trimer can be viewed as consisting of a tightly bound dimer state, with a weakly bound additional third particle.

Inspired by this result, we construct a model wave function of the form

$$\psi_t(r_1, r_2) = \frac{1}{\sqrt{2N}}[\psi_d(r_1)\psi_{ad}(r_2) + \psi_{ad}(r_1)\psi_d(r_2)]. \tag{4.9}$$

Here N is a normalization factor, ψ_d is the dimer wave function and ψ_{ad} the atom-dimer wave function specifying the behavior of the third particle. Both ψ_d and ψ_{ad} can be modeled using a similar functional form [1]

$$\psi_{d/ad} \sim [\exp(-\kappa_{d/t} r) - \exp\left(-\frac{r}{\rho_{d/t}}\right)], \tag{4.10}$$

where

$$\rho_d = \frac{3a}{8} - \frac{a}{8}\sqrt{9 - 16\frac{r_{\rm eff}}{a}}. \tag{4.11}$$

and similarly for the ρ_t in terms of the atom-dimer scattering length and effective range. The first term in Eq. (4.10) is the asymptotic solution outside the range of the potential, whereas the second term captures a suppression of the wave function at short range. The precise form of this term is less important, as another term with a similar magnitude and extent would capture the physics equally well. Note that the κ_t in this equation is defined using a different reduced mass than in Eq. (4.7), namely μ_{NaK} instead of the three-body

[1] This is the wave function solution for a separable potential of Yukawa form.

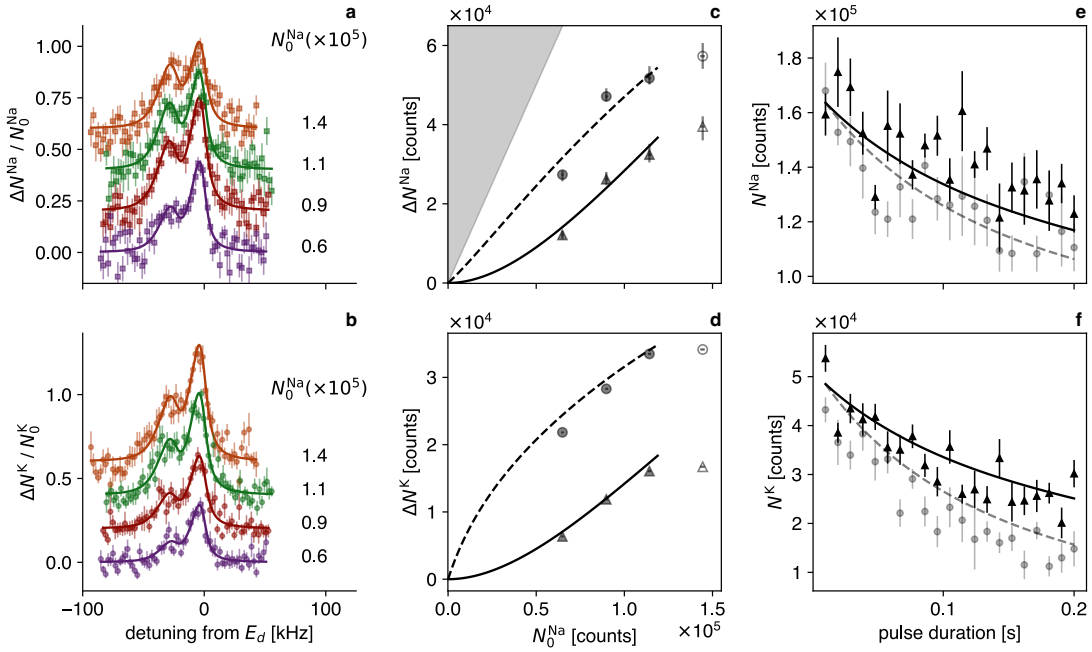

Figure 4.8: (a-b) Depletion spectra taken at 101 G, with initial corresponding peak Na density ranging from 0.4-0.88 μm^{-3}, shown as fractional loss of the initial population. Offsets have been added between spectra for visual clarity. (c-d) Peak heights of the fitted underlying dimer (circles) and trimer (triangles) features vs initial Na density. Solid (dashed) lines show fits to the two- and three-body collision models described in equation 4.12 (4.13, 4.14). The open-face markers represent the spectrum taken at the highest initial Na density, with a shorter rf pulse duration (100 ms, as opposed to 200 ms for the other spectra) to avoid unity depletion of the K population, and therefore deviate from the curve fits computed for 200 ms pulses. The grey shaded area in the upper plot has lower boundary corresponding to the maximum loss possible. (e-f) Initial state population depletion vs duration of rf pulse, with rf frequency chosen on the peak of the dimer (trimer) feature, corresponding to the circular (triangular) markers. Solid (dashed) lines show the prediction using the models described in (b).

reduced mas μ. That is because here the spatial coordinate r we are using corresponds to the boson-impurity distance instead of the hyperradius. The parameter $\rho_{d/t}$ characterizes the range at which the short-range wave function is suppressed. In particular, $\rho_d \approx r_{\rm eff}/3$ for $r_{\rm eff} \ll a$.

We find that a wave function of the form of Eq. (4.9) has an overlap of around 98% with the full numerical trimer wave function for the whole range of magnetic fields probed in the experiment. The result from this construction for B=103 G is plotted in Fig. 4.7b). For large values of either r_1 or r_2 the results in Figs. 4.7a) and b) match very well. Since this is where most of the weight of the wave function is located, this leads to the large overlap which we find. However, as may be expected, the simplified wave function does not fully capture the short range details of the wave function for $r_1, r_2/a < 1$. In particular, the trimer

wave function in a) shows a stronger suppression along the diagonal due to the interboson repulsion, which is not directly captured in b).

The simplified wave function makes the interpretation of the trimer structure and its relevant length scales easier, since they can directly be read off from Eq. (4.10). These relevant length scales are indicated by the horizontal and vertical lines in Fig. 4.7. The extent of ψ_d is set by the dimer binding energy, where for B=103 G $1/\kappa_d \approx 1.06a$. Similarly, the size of the trimer is set by $1/\kappa_t \equiv a_t$ (note that a_t is not a scattering length). However, the peak of the dimer wave function is approximately set by the effective range r_{eff}. From Fig. 4.7 we see that the peak of the trimer wave function lies around a, showing that the atom-dimer effective range is approximated well by the Na-K scattering length. We find this to be generally true over the magnetic field range which we study.

4.4 Loss processes and relative signal strengths

Since the formation processes of dimers and trimers require differing numbers of their constituent Na atoms, their association rates should depend differently on the density of Na atoms. We have measured this dependence and shown the results in the spectra in Fig. 4.8(a, b).

To model the trimer formation we use a simple rate equation with trimer formation coefficient Γ_t

$$\frac{dn_{\text{K}}}{dt} = \frac{1}{2}\frac{dn_{\text{Na}}}{dt} = -\Gamma_t n_{\text{K}} n_{\text{Na}}^2. \tag{4.12}$$

Here the densities of K, Na, are denoted by $n_{\text{K}}, n_{\text{Na}}$ respectively, and the effect of their Gaussian spatial profiles is detailed in Appendix 4.7.1. We use that the trimer decay rate is much faster than the association rate in our experiment.

The dimer formation and decay processes are modeled with the relevant two-body processes,

$$\frac{dn_{\text{K}}}{dt} = -\Gamma_d n_{\text{K}} n_{\text{Na}} - \Gamma_{d,\text{K}} n_d n_{\text{K}}, \tag{4.13}$$

$$\frac{dn_{\text{Na}}}{dt} = -\Gamma_d n_{\text{K}} n_{\text{Na}} - \Gamma_{d,\text{Na}} n_d n_{\text{Na}}, \tag{4.14}$$

$$\frac{dn_d}{dt} = \Gamma_d n_{\text{K}} n_{\text{Na}} - \Gamma_{d,\text{Na}} n_d n_{\text{Na}} - \Gamma_{d,\text{K}} n_d n_{\text{K}}, \tag{4.15}$$

where n_d denotes the density of dimers, Γ_d is the density-normalized rf association rate, and $\Gamma_{d,\{\text{species}\}}$ is the normalized loss rate due to atom-dimer collisions. Because $dn_d/dt \approx 0$ for most datasets in our experiment, we have a single timescale for population decay, set by the rate $\Gamma_d n_{\text{K}} n_{\text{Na}} \approx \Gamma_{d,\text{Na}} n_d n_{\text{Na}} + \Gamma_{d,\text{K}} n_d n_{\text{K}}$. We thus find that when fitting the rate coefficients, we are primarily sensitive to variations in Γ_d, which sets the timescale, and the ratio (but not the absolute values) of $\Gamma_{d,\text{Na}}/\Gamma_{d,\text{K}}$, which determines the ratio of population loss between species, as shown in Fig. 4.4a.

Notice that for short rf pulse durations and small depletions $\Delta n/n \ll 1$, these two models predict the intuitive linear and quadratic Na density dependence we expect for the instantaneous formation rate of Na-K dimers and Na_2-K trimers, respectively. We find that each of these models captures the qualitative trends of the peak heights observed in

experiment, as shown in the fit lines of Fig. 4.8(c, d), as well as the time-dependence of population depletion with the rf pulse tuned to the dimer and trimer resonant features Fig. 4.8(e, f).

We observe the general trend that the formation of trimers relative to dimers becomes stronger as we approach the Feshbach resonance. This can simply be understood from the fact the decreasing relative binding energy as the resonance is approached. Therefore the atom-dimer wave function ψ_{ad} in Eq. (4.9) becomes more extended, leading to larger Franck-Condon overlaps with the initial free particle wave functions.

While we see reasonable agreement between the fitted model and the experimental data in Fig. 4.8, our model neglects several mechanisms which cause the fitted parameters to be systematic underestimates. For instance, the model does not capture the behavior that the rate of molecule formation is most rapid in the densest region of the sample and for atoms having relative momentum near the rf resonance condition. The re-equilibration of atoms in real and momentum space can further bottleneck dynamics of rf association, leading to measured rates that are systematically too low. Importantly, the trap dynamics is diffusive due to the large initial state scattering length. As a result, the repopulation of areas where the Na is depleted might be slow, possibly limiting especially the dimer formation rate. We explore the effects of this re-thermalization process on rf association experiments in a follow-up work. Since the dimer coefficients have greater population depletion we expect them to be more prone to these systematic effects.

Another surprising observation is the fact that the trimer signal strength is comparable to the dimer signal. Indeed, from the theoretical wave functions we would expect the integrated trimer signal to be approximately five to ten times weaker than the dimer signal for the given atomic densities in our experiment. The underlying reason is that even though the trimer is very extended, its size is still substantially smaller than the interparticle distance. Again, non-trivial trap-dynamics, heating and saturation effects could potentially form the explanation.

4.5 Na density dependence on the formation of dimers vs trimers

The experiment shown in figure 4.8 measuring the association rate of dimers and trimers as a function of Na density was designed using the intuition that in the short rf-pulse limit, the respective association rates should have linear and quadratic scaling with Na density.

An important feature of the implementation of this experiment is that the initial temperature of the mixture is largely unchanging between datasets, as we fix the final ten-second evaporation stage in the optical dipole trap, which determines the temperature. We adjust the Na density by varying the total number loaded into the mixture. This can be controlled with the MOT loading time as a coarse tuning knob and the rf-knife evaporation duration in the magnetic trap, which favors higher Na:K ratio for longer rf-knife ramps over the same frequency ramp.

We can also increase the real-space density of the sample by compressing the optical dipole trap adiabatically, after evaporation. This has the undesired effect of changing the

temperature and momentum-space distribution as well. The effect of this is to not only alter the rate of rf association, but also broaden its lineshape, making it harder to resolve the dimer and trimer features. We briefly discuss this quantitatively below.

Dimer association after adiabatic trap compression

To model the rf association rate and lineshape, we use a simplified version of equation (1) of [91], keeping the ratio of trap frequency to temperature ω/T constant (i.e. moving along an adiabat), while varying the temperature. We omit factors independent of trap frequency and temperature and not considering non-thermal broadening mechanisms, to find the number of molecules of binding energy E_b associated from atoms of initial relative kinetic energy ϵ_r,

$$N_{mol} \propto \frac{\tilde{\omega}^2}{T^3} \exp\left(-\frac{\epsilon_r}{k_B T}\right) F_f(\epsilon_r) \propto \left(\frac{\tilde{\omega}}{T}\right)^3 \exp\left(-\frac{\epsilon_r}{k_B T}\right) \frac{\sqrt{\epsilon_r E_b}}{(\epsilon_r + E_b)^2}, \tag{4.16}$$

where we have Franck-Condon factor $F_f(\epsilon_r) \propto \tilde{\omega}\sqrt{\epsilon_r E_b}/(\epsilon_r + E_b)^2$ for vanishing initial scattering length. This analysis allows us to understand why doing an adiabatic compression does not lead to the increase in association rate as one might intuitively expect by only considering the effect that compressing the trap has directly on the real-space density. An example of such an unintuitive scaling is shown in figure 4.9 and further illustrates why this implementation is not ideal experimentally.

4.6 Heating from rf-induced three-body loss

In typical observations of three-body loss, where the requirement is that three atoms "meet" and undergo an inelastic loss process (no rf required), the typical result is that in a harmonic trap, this leads to heating. This is intuitive under the interpretation that the inelastic loss process does not strongly depend on the momenta (or kinetic energy) of the colliding trio, and that collisions happen most frequently near the trap center, where the density is high and the average (potential) energy of the atoms is lower than the mean. The removal of these lower energy atoms and rethermalization then has an anti-evaporative effect [92], [93].

Our rf spectroscopy experiments are not only a measurement of which rf drive frequencies we are able to perform rf association, which allows for the precise determination of binding energies. We can take the alternative view that we are observing an rf-induced three-body loss, since a large fraction of the associated products undergoes decay either due to a collision with an additional atom (dimers) or due to the proximity of the three atoms in the product (trimers). A key distinguishing feature of this process from the one discussed above is that rf association is sensitive to the relative momenta of the atoms being associated. So while atoms with low potential energy are most likely to be associated, depending on the rf drive frequency, we can selectively remove atoms in a particular "shell" in relative momentum space. These two effects can be competing for rf drives well detuned from the binding energy, where atoms with high relative momenta are addressed. In this case, we remove a pair of atoms with high kinetic energy, but low potential energy. Therefore it is not clear at all *a priori* whether we should always expect to observe heating.

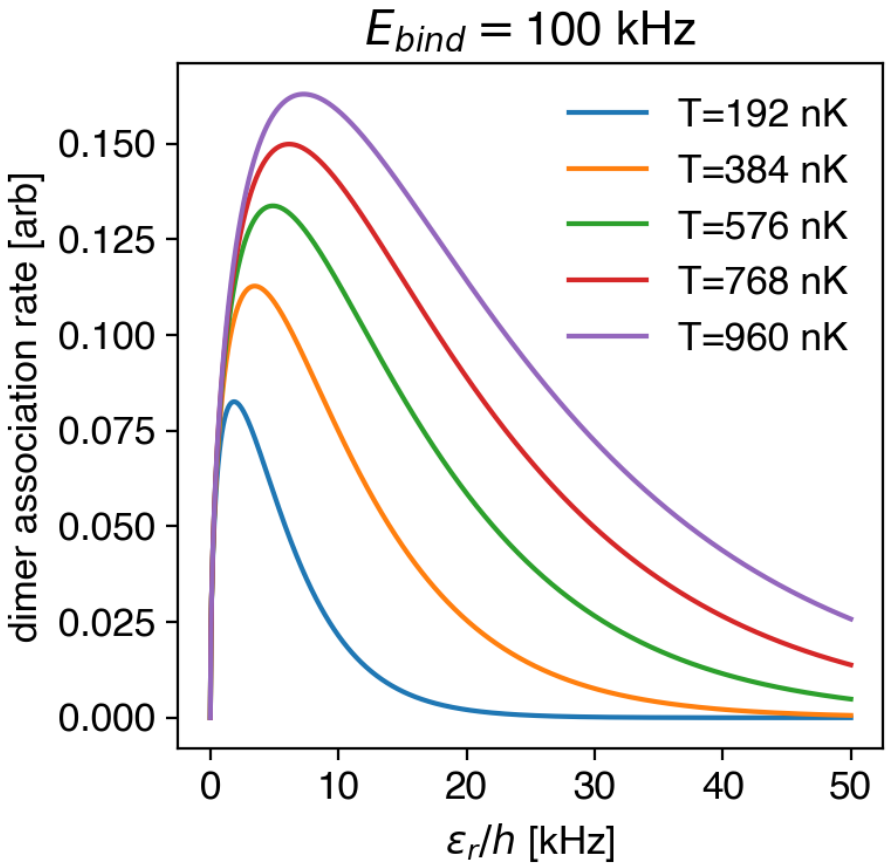

Figure 4.9: The rf association lineshape for dimers, calculated using equation 4.16, with fixed initial atom number and constant $\tilde{\omega}/T$, using $E_{bind} = 100$ kHz as an example. The lowest temperature shown (192 nK) roughly corresponds to the typical temperature of the atomic mixture we prepare, prior to application of rf. A five-fold increase in the temperature (and correspondingly $\approx$ ten-fold increase in the single-species density) is needed to double the maximum association rate. The increase in temperature also broadens the line to an extent that would make resolving a trimer feature 20-30 kHz detuned from the dimer resonance quite challenging experimentally.

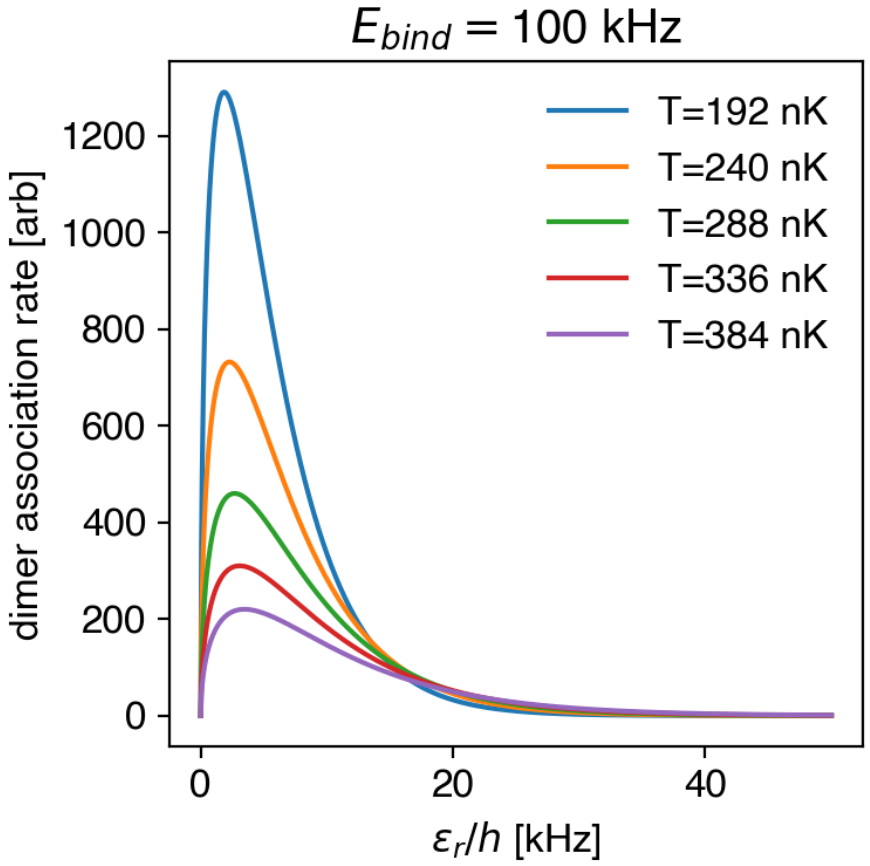

Figure 4.10: The rf association lineshape for dimers, calculated using equation 4.16, with fixed initial atom number and constant $\tilde{\omega}$ but variable temperature T, using $E_{bind} = 100$kHz as an example. The lowest temperature shown (192 nK) roughly corresponds to the typical temperature of the atomic mixture we prepare, prior to application of rf. A 20% increase in the temperature already almost halves the peak association rate, since the scaling with temperature is $\propto T^{-3}\exp(-\epsilon_r/(k_B T))$. Note that the peak of the lineshape does not shift dramatically over a 2x variation in temperature in this range.

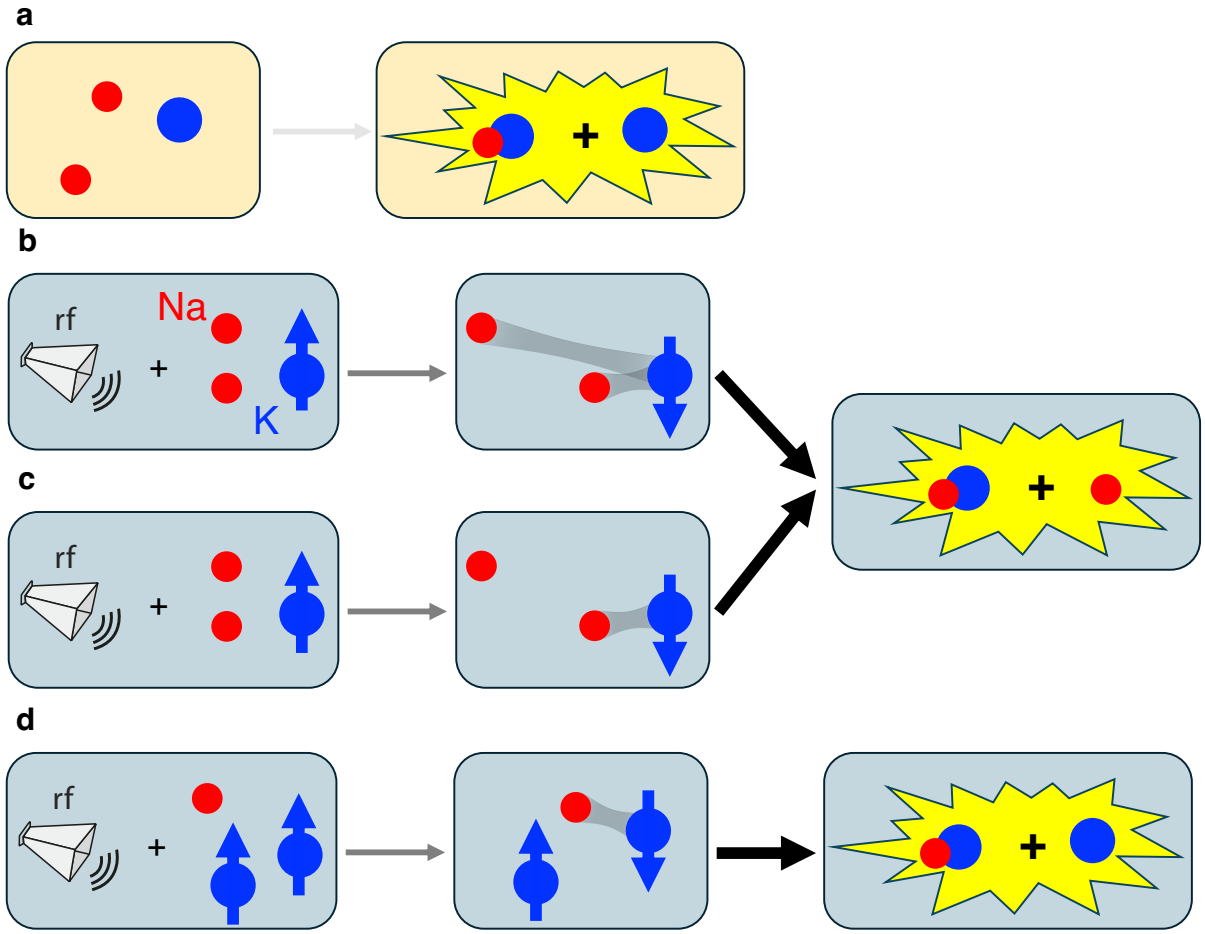

Figure 4.11: Three-body loss processes in our experiment, caused by relaxation into molecular bound states and a corresponding release of kinetic energy and escape from the trap. (a) Without rf, an inelastic collision between three atoms is required for loss. This rate is negligible compared to the typical rf pulse lengths of ~ 100 ms. (b-d) With rf, we can first resonantly associate atoms together into either a shallow-bound trimer (b) or dimer (c,d), which leads to enhanced losses. As denoted by the thickness and opacity of the arrows, rf association is the rate-limiting step in our experiment.

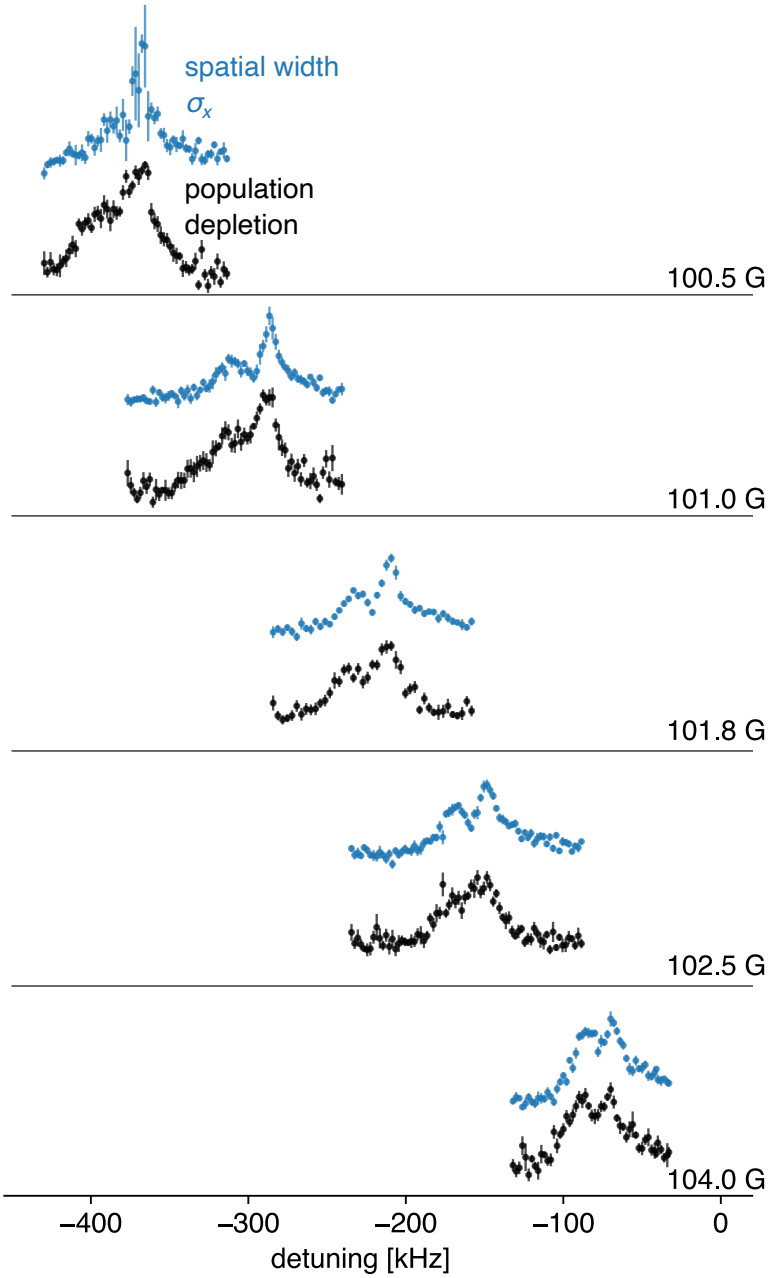

Figure 4.12: We find that the fitted Gaussian width (blue) of the atoms' spatial profile exhibits an rf frequency dependence, similar to the population depletion (black). The peak change in the widths (populations) are ∼20% (∼50%). As an example, we compare the broadening of the long axis of the cloud σ_x and population depletion in the K signal at different B-fields.

What we observed experimentally is that the heating mechanism in general wins out, and the heating rate of the atomic mixture is maximum near a resonance, as seen in figure 4.12[2], where the broadening in cloud widths indicate increasing temperatures. A possible explanation comes from considering that any possible cooling effect acts only on three degrees of freedom (the relative momentum), while the heating effect acts on six (three position coordinates times two atoms).

This is a wonderful complementary technique to observing the population loss, for two experimental reasons. The main source of noise in observing population loss is the stability of loading the atomic mixture, which has a fractional 1-σ deviation of $\approx 10\%$ when the apparatus is "well-behaved," and further improvements to this figure require careful investigation of every step in the loading procedure. The temperature of the mixture, on the other hand, is almost solely determined by the final trap depth in the optical dipole trap. Carsten Robens and Zoe Yan, while working on [38], implemented upgrades to the trapping optics (e.g., launching the "plug"-ODT from a fiber to replace the existing periscope) that largely eliminated this single point of possible instability. Furthermore, since we are working in the thermal regime, the atomic cloud size is *not* strongly dependent the number of atoms, and we have an overall stability corresponding to a fractional 1-σ deviation of the cloud width $\approx 3-5\%$ in the ^{40}K images, leading to a higher signal-to-noise ratio.

The rf-induced heating process has nontrivial temporal dynamics. The relevant factors include (1) the depletion of the available "reactants" (as addressed by the model in section 4.4), (2) the rate at which the atoms re-equilibrate to a thermal distribution, and (3) the dependence of the rf association rate itself on the temperature (through its dependence on the phase space distribution). The typical rf pulse durations of ~ 100 ms we use to achieve $\approx 30-50\%$ depletion of the sample are $\sim 10-100$ trap periods (depending on which eigenaxis of the trap we compare to), and the atom-atom scattering rate is of order $\sim$kHz . Therefore, we can decouple the time scale described in (2) from the problem by assigning an instantaneous temperature of the cloud. Therefore, it is clear that a revised version of the model presented in section 4.4 incorporating the temperature dependence is necessary, and this is currently a work in progress.

4.7 Additional discussions

4.7.1 Defining length scale for rf-association coefficients Γ_D, Γ_T

Since the rate equations in the main text implicitly discard the spatial dependence of the atomic and molecular densities, we describe how to construct length scales for an equivalent experimental dynamics with the same total atom numbers, distributed uniformly in the corresponding cubic volume (e.g., in a box trap), under certain assumptions[3].

We will assume that the spatial profile is static in time up to a scaling (e.g., assuming the atoms/molecules rethermalize to their initial temperature instantaneously). This neglects the heating induced by our spectroscopy procedure and the thermalization time-scale, and

[2]Thanks to Huan Bui's careful analysis of the spatial profiles.

[3]These assumptions are quite strong, so these results should be taken qualitatively rather than quantitatively.

therefore this will only serve as a rough model. Let us define the unit-normalized profiles $u_{\mathrm{K}}, u_{\mathrm{Na}}$ such that for both species s, $\int u_s(r)d^3r = 1$. The time and spatial dependence of the density n_s will be factorized into the total atom number N_s and the spatial distribution,

$$n_s(r,t) = N_s(t)u_s(r). \tag{4.17}$$

For trimers, we then have, after integrating over space,

$$\frac{dN_{\mathrm{K}}}{dt} = \frac{1}{2}\frac{dN_{\mathrm{Na}}}{dt} = -\Gamma_t N_K N_{\mathrm{Na}}^2 \int u_{\mathrm{K}}(r)u_{\mathrm{Na}}^2(r)d^3r, \tag{4.18}$$

The integral $I_t = \int u_{\mathrm{K}}(r)u_{\mathrm{Na}}^2(r)d^3r$ with units of $[\text{length}]^{-6}$ defines an effective box length for the trimers $l_t = I_t^{-1/6}$.

For the dimers, we can assume that the dimers formed do not have time to redistribute before they are lost from colliding with a free atom and are thus their spatial distribution is given by

$$u_d(r) = u_{\mathrm{K}}(r)u_{\mathrm{Na}}(r)/\mathcal{N}, \tag{4.19}$$

where the normalization factor $\mathcal{N}$ is included so that again u_d integrates to one. In terms of the absolute numbers, we have

$$\frac{dN_{\mathrm{K}}}{dt} = -\Gamma_d N_{\mathrm{K}} N_{\mathrm{Na}} \int u_{\mathrm{K}}(r)u_{\mathrm{Na}}(r)d^3r - \Gamma_{d,\mathrm{K}} N_d N_{\mathrm{K}} \frac{\int u_{\mathrm{K}}^2(r)u_{\mathrm{Na}}(r)d^3r}{\mathcal{N}}, \tag{4.20}$$

$$\frac{dN_{\mathrm{Na}}}{dt} = -\Gamma_d N_{\mathrm{K}} N_{\mathrm{Na}} \int u_{\mathrm{K}}(r)u_{\mathrm{Na}}(r)d^3r - \Gamma_{d,\mathrm{Na}} N_d N_{\mathrm{Na}} \frac{\int u_{\mathrm{Na}}^2(r)u_{\mathrm{K}}(r)d^3r}{\mathcal{N}}, \tag{4.21}$$

$$\begin{aligned}\frac{dN_d}{dt} &= \Gamma_d N_{\mathrm{K}} N_{\mathrm{Na}} \int u_{\mathrm{K}}(r)u_{\mathrm{Na}}(r)d^3r \\ &\quad -\Gamma_{d,\mathrm{Na}} N_d N_{\mathrm{Na}} \frac{\int u_{\mathrm{Na}}^2(r)u_{\mathrm{K}}(r)d^3r}{\mathcal{N}} \\ &\quad -\Gamma_{d,\mathrm{K}} N_d N_{\mathrm{K}} \frac{\int u_{\mathrm{K}}^2(r)u_{\mathrm{Na}}(r)d^3r}{\mathcal{N}}.\end{aligned} \tag{4.22}$$

It is not possible to identify a single length scale as we did with trimers that would replicate the same dynamics with the equivalent experiment in a box trap.

We will instead present a simplified model for constructing an effective length, where we assume the rf association is rate-limiting, as in the case of the experiment. We propose

$$\begin{aligned}\frac{dN_{\mathrm{K}}}{dt} &= -(1+\alpha)\Gamma_d N_{\mathrm{K}} N_{\mathrm{Na}} \int u_{\mathrm{K}}(r)u_{\mathrm{Na}}(r)d^3r, \\ \frac{dN_{\mathrm{Na}}}{dt} &= -(1+\beta)\Gamma_d N_{\mathrm{K}} N_{\mathrm{Na}} \int u_{\mathrm{K}}(r)u_{\mathrm{Na}}(r)d^3r, \\ \frac{dN_d}{dt} &= (1-\alpha-\beta)\Gamma_d N_{\mathrm{K}} N_{\mathrm{Na}} \int u_{\mathrm{K}}(r)u_{\mathrm{Na}}(r)d^3r,\end{aligned} \tag{4.23}$$

where the coefficients α, β encapsulate the dimer-atom collisional losses and satisfy $\alpha, \beta \geq 0$ and $\alpha + \beta \leq 1$. Here, they implicitly depend on the relative instantaneous densities

between the atomic species and their relative scattering rates with dimers. We will neglect this dependence. Furthermore, since we observe a negligible rate of dimer arrivals in most experiments, we have $\alpha + \beta \approx 1$. We can now identify the length scale for dimers via the integral $I_d = \int u_{\mathrm{K}} u_{\mathrm{Na}} d^3r$ and $l_d = I_d^{-1/3}$.

We will now assume that the distributions $u_{\mathrm{K}}, u_{\mathrm{Na}}$ follow a Maxwell-Boltzmann distribution with a temperature $T = 200$ nK. We will define, for trap axis i and species s, $\sigma_{i,s} = \sqrt{k_B T/(m_s \omega_i^2)}$, so that the unit-normalized probability distribution is

$$u_s(x) = \prod_i (2\pi\sigma_i)^{-1/2} \exp\left(-\frac{m_s \omega_i^2 x_i^2}{2k_B T}\right). \tag{4.24}$$

From the trap frequencies provided in the main text, for Na, we have $\sigma_i = (10.8, 11.5, 75.1)$ μm, and for K, we have $(6.8, 7.2, 47.0)$ μm. For the dimer, the characteristic length scale evaluates to

$$l_d = \left[(2\pi)^{-3/2} \prod_i \delta_i \times \prod_{i,s} (1/\sigma_{i,s})\right]^{-1/3} = 62\,\mu\mathrm{m}, \tag{4.25}$$

where we have introduced the auxiliary expression $\delta_i^2 = \sigma_{i,K}^2 \sigma_{i,Na}^2/(\sigma_{i,K}^2 + \sigma_{i,Na}^2)$. For the trimer, we have

$$l_t = \left[(2\pi)^{-3} \prod_i \theta_i \times \prod_{i,s\in\{K,Na,Na\}} (1/\sigma_{i,s})\right]^{-1/6} = 61\,\mu\mathrm{m}, \tag{4.26}$$

where $\theta_i^2 = \sigma_{i,K}^2 \sigma_{i,Na}^2/(2\sigma_{i,K}^2 + \sigma_{i,Na}^2)$.

4.7.2 Estimates of dimer and trimer lifetimes

By measuring the arriving population (or lack thereof) of dimers and trimers in the final spin state of K after applying an rf association pulse, we can make some estimates of the time scale of their decay.

Experimental data and fitting

See figure 4.13 for plots of the data analyzed, taken at $B = 105$ G with $t_{rf} = 3$ ms square rf pulse, $\Omega_{Rabi}^{atomic} \approx 2\pi \times 12$ kHz. The fit model used is a sum of dimer and trimer rf association lineshapes (see manuscript) convolved with a 8kHz FWHM Lorentzian kernel, on top of an atomic free-to-free background modeled by a Lorentzian on the lower frequency wing. The initial and arriving populations are jointly fitted using the same dimer binding energies and background location; the arriving population is fit with zero trimer feature weight; this choice was made because even by eye there appears to be no prominent second peak.

The Na depletion spectra is omitted from the analysis and could be included for a more thorough re-analysis.

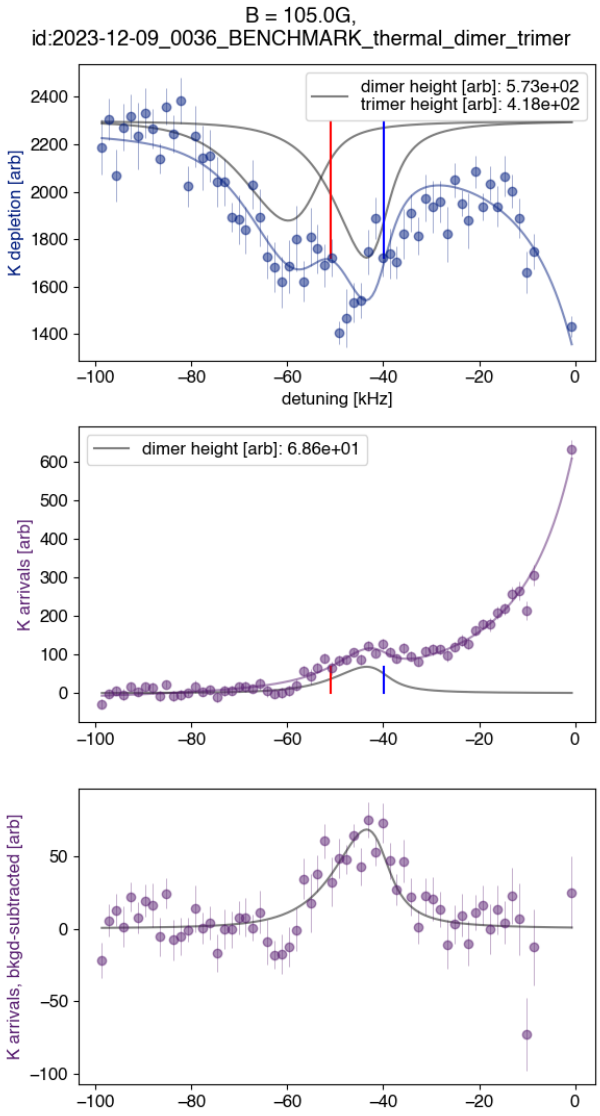

Figure 4.13: Data taken at $B = 105$ G with $t_{rf} = 3$ ms square rf pulse, $\Omega_{Rabi}^{atomic} \approx 2\pi \times 12$ kHz. (top) depletion of K initial spin state. Blue and red lines represent fitted dimer and trimer binding energies. (middle) arrivals into K final spin state. (final) arrivals, with Lorentzian background subtracted. Error bars represent standard error on the mean over $\sim$10 repetitions.

Imaging of K, $F = 9/2, m_F = -7/2$

Our atomic-only calibration datasets give us quantitative evidence that we are likely to be underestimating the K, $F = 9/2, m_F = -7/2$ population ("arrivals") by $\approx 10 - 20\%$ due to artifacts of the imaging scheme, leading to underestimations of the lifetime.

Dimer lifetime bounds

We will make several assumptions to simplify the analysis of the experiment. We will assume

1. The loss is approximately exponential in time. This amounts to assuming that the free atom populations available to collide with dimers and cause loss is approximately constant over the rf pulse duration.

2. The continuous production of dimers during the rf pulse is irrelevant, and we can approximately treat this experiment as equivalent to one where the dimers are populated and we wait for t_{rf} for them to decay. This will cause us to underestimate the lifetime, since the decay rate is proportional to the instantaneous dimer population.

3. The K population depletion is only due to rf association, and not collisions with the associated dimers, i.e. we assume all loss events are Na-NaK. This will cause us to overestimate the dimer population and therefore underestimate the lifetime as well. To quantify how much of an effect this has, we could make the complementary assumption, which will give a factor 1/2: all loss events are K-NaK, and therefore exactly half the K population depletion is due to rf association into dimers.

Under these assumptions, we have that

$$N_{arrival} \approx N_{depletion} \exp(-t_{rf}/\tau_{dimer}), \tag{4.27}$$

where the number of arrivals (depletion) $N_{arrival} = 68.6$ ($N_{depletion} = 573$), in experimental arb units, comes from the curve fits. Therefore we have

$$\tau_{dimer} \geq \frac{t_{rf}}{-\log(N_{arrivals}/N_{depletion})} = 1.41\,\text{ms}. \tag{4.28}$$

Note that the dimer decay time τ_{dimer} will depend on the density of free atoms available to collide with the dimers, so this estimate is particular to the realization of the experimental mixture loading.

This corresponds to lifetime broadening of $1/\tau_{dimer} = 2\pi \times 113$ Hz, which is negligible for our experiment.

Trimer lifetime bounds

We will make several analogous assumptions for the analysis of the trimer lifetime. We assume, with similar implications as before,

1. The loss is exponential in time. This is exactly true if we assume the next point, since trimer decay is an intrinsic mechanism.

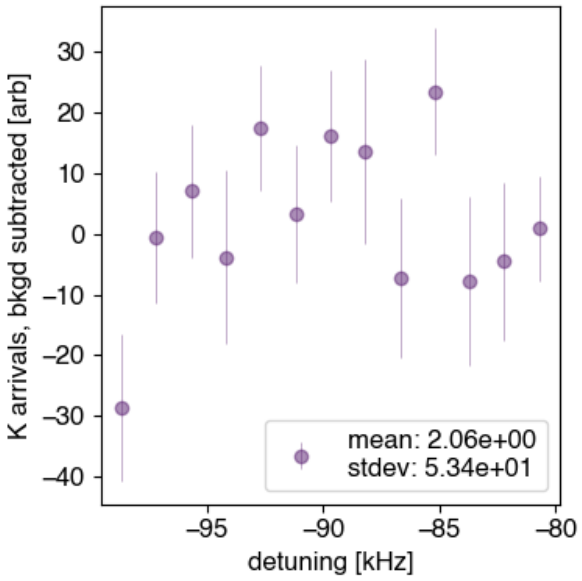

Figure 4.14: Shown is a the portion of the spectrum we can consider as the "background." (There is significant point-to-point fluctuation as well, which is encapsulated by the overall standard deviation of the entire subset, ∼50 arb.)

2. The continuous production of trimers during the rf pulse is irrelevant, and we can approximately treat this experiment as equivalent to one where the trimers are populated and we wait for t_{rf} for them to decay.

3. The K population depletion is only due to rf association. This is a reasonable assumption for trimer formation since its dominant decay mechanism is in fact decay into NaK + Na.

We do not see any trimer arrival signal in our experiment. We will therefore give first a lower bound for its lifetime from the broadening of the spectra, as accounted for by the 8 kHz FWHM kernel used for fitting. A conservative estimate (loose lower bound) assigns the entire 8 kHz to lifetime broadening, giving

$$\tau_{trimer} \geq \frac{1}{2\pi \times 8\text{kHz}} = 20\mu\text{s}. \tag{4.29}$$

This is a loose lower bound since we know we can account for some of the broadening to rapid fluctuations in the B-field (∼3-5 kHz). An even more conservative estimate assigns the entire width of the underlying spectral feature (∼15-20 kHz), not just the convolution kernel, to lifetime broadening. This is unreasonable however given that theory ascribes part of the width to the E^2 threshold law for three-body association and finite temperature.

To determine an upper bound for the trimer lifetime, we consider the following. We have data where the rf detuning is on the peak of the trimer feature (around −60 kHz), which does not appreciably differ from the baseline by eye. A subset of the spectrum showing only the baseline is given in figure 4.14. We will use the standard error on the mean of each data

point being ~ 20 arb as the scale for the minimum identifiable signal N_{min}. Then, we have, for a depletion of $N_{depletion} = 418$ arb,

$$\tau_{trimer} \lesssim \frac{t_{rf}}{-\log(N_{min}/N_{depletion})} = 0.97\,\text{ms}. \tag{4.30}$$

4.7.3 Imaging

We are primarily interested in counting the total number of atoms and measuring their temperature for this experiment. We therefore employ on-resonant absorption imaging with time-of-flight, since the *in situ* profile of the atoms are of secondary importance for us.

^{40}K, $F = 9/2, m_F = -9/2, -7/2$

We use the "simple" scheme described in section 5.4.6. In most experiments, we are not particularly interested in measuring the $m_F = -7/2$ population precisely, as our rf association pulses are much longer than the lifetime of the associated products. Therefore, after the rf pulse, only a negligible portion of the products detectable in the $m_F = -7/2$ channel remain. The problem of $m_F = -9/2$ population leaking into the $m_F = -7/2$ image is further mitigated by the fact that we image the $m_F = -9/2$ first, heating up that population, and then give time-of-flight before imaging $m_F = -7/2$, allowing the $m_F = -9/2$ atoms to propagate freely out of the region-of-interest and the focal plane.

Imaging ^{23}Na, $F = 1, m_F = 1$ with a cycling transition

No optical cycling transition exists for ^{23}Na, $|F = 1, m_F = 1\rangle$, but one does for $|F = 2, m_F = 2\rangle$, driving the σ_+ transition to $|F' = 3, m'_F = 3\rangle$ on the D2 line. The main advantage of imaging on a cycling transition is the lack of optical pumping into other hyperfine states, which limits the number of photons scattered before the atoms become dark (therefore limiting also signal-to-noise), and additionally makes the absorbed fraction of photons sensitive to the timing and intensity of the imaging laser pulse. To transfer the $|F = 1, m_F = 1\rangle$ population to the state that supports cycling imaging, we shine D2 light resonant with a $|F = 1, m_F = 1\rangle$ σ_+ transition, which pumps atoms into $|F = 2, m_F = 2\rangle$ (a *dark state* when illuminating with $|F = 1, m_F = 1\rangle$ σ_+ light). The main advantage of using this method is the robustness of optical pumping in general. The optical transition is ≈ 10 MHz wide and is fairly easy to address with given the stability of the experimental apparatus (e.g. applied external B-fields from shot-to-shot).

Due to experimental limitations, the optical pumping light uses the same optical paths that we typically use for non-cycling $|F = 1, m_F = 1\rangle$ σ_+ imaging, propagating along the imaging axis (colloquially "lab-Z"). This optical axis is then used once more in the experimental sequence to perform cycling imaging on $|F = 2, m_F = 2\rangle$. There are several major disadvantages to this scheme, as we discuss below.

There are a few idiosyncrasies of this scheme that are of experimental relevance. The primary consideration is that inevitably the $F = 1$ light used for optical pumping lands on the camera sensor, and this is indistinguishable from the $F = 2$ light later used for cycling imaging. If the optical pumping light is collected on the same frame as the imaging light,

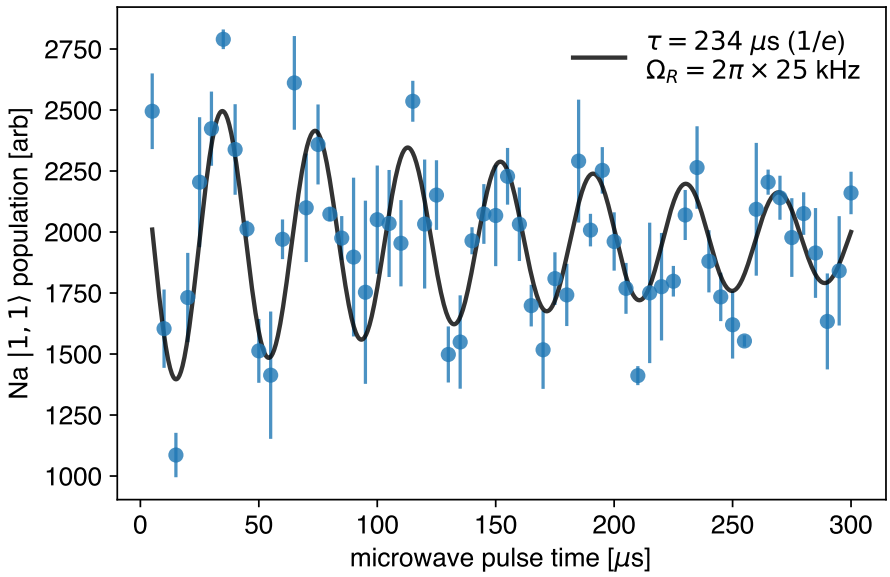

Figure 4.15: We observe oscillations in the Na $|1, 1\rangle$ population due to Rabi oscillations to $|2, 2\rangle$ at 80.3 G. Data has been fitted to an exponentially decaying sinusoid. Credit to Huan Bui for taking this data.

this can then wash out the "absorption fraction" signal, as typically $F = 2$ cycling images are darker than $F = 1$ non-cycling images. Correcting for this effect is a delicate procedure which depends on both the intensity and timing of the $F = 1$ and $F = 2$ light pulses. As the intensities drift over time, this leads to a need for frequent recalibration, which is obviously undesirable. This calibration was performed in Appendix C of [41], and a calibration with units of optical density (OD) per pixel per atom number is quoted; however, we found that within a few months the calibration was no longer valid given drifts in the laser powers. The unprocessed OD from this scheme are deceptively low, and taking data with "blacked-out" images (higher OD than what our signal-to-noise allows) can easily go unnoticed, leading to distortions in the number of counted atoms, or in other words, a *linear* conversion from OD per pixel to atom counts becomes incorrect.

To distinguish the optical pumping and imaging light, we instead read out the $F = 1$ and $F = 2$ light on different sub-frames of the camera acquisition, i.e. tagging them temporally. The drawback of this workaround is how fast the camera can shift a sub-frame; in "fast-kinetics" mode this is $\approx 700\mu$s (depending on the number of rows being shifted). During this shifting time, the atoms undergo expansion, and prior to their expansion they may not be in thermal equilibrium, due to the injection of energy from the optical pumping light. Therefore, the spatial profile of the atoms at the time of imaging is not easily modeled from first principles, but we expect that the atom counts of this method to be faithful. A by-product of this readout procedure is that we can also have an $F = 1$ *in situ* image that can provide information about the spatial profile prior to the distortion due to motion induced by optical pumping.

There are several changes for future implementations to avoid illuminating the camera

	atomic species	trimer signal	citations
rf spectroscopy	three spin states of ^{6}Li	atom loss, atom-dimer association resonance	[82], [94]
	two spin states of ^{7}Li	atom loss, free-atom association resonance	[95]
	two spin states of ^{7}Li	interferometry using dimer and trimer superposition	[96], [97]
loss resonances	spin-polarized ^{133}Cs	successive atom loss resonances, $\lambda \approx 22.7$	[46], [76]
	^{6}Li + 2 $\times^{133}$Cs	successive atom loss resonances, $\lambda \approx 5$	[47], [48], [98]
	^{40}K + 2$\times^{87}$Rb	atom-dimer resonance, but no free-atom resonance, observed	[99]
	^{41}K + 2$\times^{87}$Rb, 2$\times^{41}$K + ^{87}Rb	atom loss resonances. Disputed by [93]	[100]
	^{7}Li	atom-dimer (and dimer-dimer) loss resonances	[101]
other	^{85}Rb	dimer and trimer decay vs time	[42]
	^{4}He	Coulomb explosion imaging of trimer structure	[49]

Table 4.1: We summarize the observations of Efimov/halo trimers in some other experimental systems.

with $F = 1$ optical pumping light. One solution is to shine the optical pumping light from a different optical axis, and immediately afterwards exposing the camera for a $F = 2$ image. A second possibility is to instead use ≈ 1.9 GHz microwaves to drive the $|F = 1, m_F = 1\rangle \leftrightarrow |F = 2, m_F = 2\rangle$ transition *coherently*, which we can do with Rabi frequency of $\approx 2\pi \times 25$ kHz, see figure 4.15. The benefit of using a coherent drive is that the spatial properties of the atomic cloud are largely unchanged, as only the internal spin degree of freedom is manipulated. (It should however be noted that the external trapping potential, especially one due to a magnetic field gradient, depends on the spin state.) The downside of using this microwave transition is its high sensitivity to the external magnetic field, which can drift or fluctuate, shifting the spectroscopic feature by ≈ 2 kHz/mG and limiting its contrast.

4.8 Other experimental observations of atomic trimers

We briefly summarize relevant experiments in the table 4.1.

4.9 Resolving a second Efimov state?

The difficulty of directly measuring the famous Efimov geometric scaling factor λ (≈ 22.7 for three identical bosons) using rf spectroscopy is the extreme requirement on frequency

resolution, since the binding energies scale as λ^2. To give a sense of scale, the typical measured binding energy in such experiments is on the ∼10–100 kHz scale, and so for the case of three equal masses, we require a resolution on the scale of 20–200 mHz[4]. To compare to our experimental system, this corresponds to temperatures of ∼1–10 pK (typical 200 nK in our experiments) and coherence times of ∼5–50 s (typical ∼ms in our experiment, from magnetic field fluctuations). In our experiment, the scaling factor is calculated to be even less forgiving, with $\lambda \approx 100$, and therefore with current techniques we do not expect to be able to detect a second Efimov state using our methodology.

4.10 Direct measurement of trimer decay

As discussed in section 4.7.2, we are unable to observe population of the trimer state and thus do not directly measure its decay dynamics. Two other techniques have been developed towards this goal. In [42], a rapid magnetic field ramp across a Feshbach resonance creates both dimers and trimers in a bosonic sample. Since the dimers and trimers are indistinguishable to their imaging probe, the trimers' decay can only be then identified due to its single-body exponential time-dependence. In the Bar Ilan group, a coherent superposition of dimers and trimers are created using a short-duration, high-bandwidth pulse and probed using an interferometry protocol (DITRIS). The fast decay of trimers contributes to decreasing contrast in the oscillations; however, again in this set of experiments dimers and trimers cannot be distinguished [96], [97].

In our experiment, we are able to selectively populate the trimer state spectroscopically[5], and the remaining obstacle is if we can increase its rate. In principle, using a stronger drive, e.g., with more rf power or instead using a laser-driven two-photon Raman transition, should be beneficial. Of course, one consideration when increasing the coupling and decreasing the pulse duration is to verify that power and Fourier broadening does not cause the unwanted driving of the dimer association or atomic transitions as well. However, it is not clear that the available drive power is the only limiting factor in the production of trimers, since the atom-trios ready for conversion (e.g., given by the phase space overlap) may also cap the total number of trimers produced in a short pulse.

4.11 Conclusion

In this paper, we have reported the first direct production of heteronuclear halo trimers and the measurement of their binding energy. We focused on the scenario of two light Na bosons bound to one heavy K-atom. Our measurements revealed an array of physical properties, including binding energy, lifetime, and density dependence of the formation rate, that allow us to clearly distinguish the trimers we observe from the familiar Feshbach dimer molecule. With precision rf-spectroscopy of these few-body systems, we have resolved the binding energies of both two- and three-body bound states over an order of magnitude in

[4]We use shallower binding energies in our argument here, since scaling in the opposite direction, towards deeper binding energies, takes us further out of the "halo"/universal regime.

[5]Moreover, into an initially unpopulated spin-state, which should help with SNR problems.

binding energies. A measurement of the remaining dimer and trimer populations after the application of the rf association pulse allowed us to place bounds on the trimer lifetime, an active area of both experimental [42], [96], [97] and theoretical [102] investigation. We found that the density dependence of the rf signal can be understood from simple two- and three-body processes.

Furthermore, we presented a theoretical analysis of the trimer energy and wave functions, developing a clear picture of the nature of these halo trimers. Improved theoretical modeling both on the few-and many-body level and a reduction of the experimental noise should enable a more refined analysis in the future, opening the way to more accurate comparisons. This will allow to answer open questions regarding the universality of these trimer states and the nature of the three-body parameter in these systems. We also expect that with reasonable technical improvements, it will be possible to associate trimers within their decay time and thus directly measure their intrinsic lifetime. Furthermore, the appearance of halo trimers should not be restricted to Na-K mixtures, because the conditions of having heavy "impurities" immersed in a Bose gas with modest positive scattering lengths are met in other mixtures as well. A possible feature of a halo trimer was also observed in the atom-dimer loss rate for a different Feshbach resonance but for the same species used here [103].

Our study is also important for other research avenues in the domain of ultracold gases. For example, the presence of weakly bound trimer states is of direct relevance for bi-alkali molecule experiments which rely on the formation of dimers by ramping across a Feshbach resonance as an intermediate step [104]. The presence of weakly bound trimer states is also expected to play an essential role in the many-body physics which emerges when the gases are cooled into the degenerate regime [105]–[107]. This will lead to interesting higher-order correlations, which we start to explore in Chapter 5.

Chapter 5

Bose polarons as hybridized dimers and trimers

The content in this chapter includes content copied verbatim from the manuscript in preparation,

> Alexander Chuang*, Carsten Robens*, Arthur Christianen*, Yiqi Ni, Eric Wolf, Yiming Zhang, Richard Schmidt, Martin W. Zwierlein (2024). Superpositions of dimers and trimers formed from Bose polarons.

This manuscript was written as a collaborative effort between the experimental team at MIT and theorists A. Christianen and R. Schmidt.

5.1 Introduction

Throughout physics, important properties of particles are defined by their interactions with background fields. For example, in the standard model the Higgs field gives all particles their mass, and the field of W-bosons mixes the different flavours of quarks according to the Cabibbo–Kobayashi–Maskawa (CKM) matrix. In solids, electrons can form polaron quasiparticles due to dressing by phononic excitations of the crystal lattice, and excitons can form polaritons by coupling to the electromagnetic field in a cavity.

Here we explore the case of an ultracold atom immersed in the quantum field formed by a Bose-Einstein condensate (BEC). In the spirit of quantum simulation, where ultracold gases find many applications, it was shown that such an "impurity" in a BEC can form a "Bose polaron" quasiparticle, reminiscent of the well-known Fröhlich polaron in condensed matter. However, for sufficiently strong interactions, the behaviour of ultracold gases clearly differs from the condensed matter case. For example, impurities can bind bosons from the background gas to form so-called Feshbach molecules. In condensed matter, the equivalent would be electron-phonon bound states, which only exist in special materials [108].

In case of a fermionic background gas, already relatively simple theories were sufficient to explain the so-called polaron-to-molecule transition, which is a precursor to the BEC-to-BCS crossover. However, in the Bose polaron case the possibility of binding multiple bosons from the BEC and the importance of the interboson interactions, has led this problem to remain

an open topic of discussion. From this difference alone, one can recognize the intricacies of bound-state formation in a degenerate medium, and how this can lead to the formation of strongly correlated matter.

5.2 Experimental methods

In our experiments featuring fermionic ^{40}K-atoms as impurities in a BEC of ^{23}Na, we observe that the background BEC stimulates the formation of a conceptually new quasiparticle, i.e., a coherent superposition of dimer, trimer, and free impurity states. A pictorial representation of our experiment is given in Fig. 5.1a). In Fig. 5.1b) we indicate the simple theoretical model which explains the core of our experimental observations. This effective three-level Hamiltonian consists of "bare" levels corresponding to a free impurity, a dimer (Na + K) and a trimer (2Na + K) state, and off-diagonal coupling between these levels caused by the BEC. The eigenvalues of this Hamiltonian and the character of the eigenstates in terms of the different free components is shown in Fig. 5.1c). We also observe the weakly-bound trimer state in absence of medium-effects (see Chapter 4). This is already noteworthy, since this marks the first observation of a trimer state in the Efimov-unfavourable regime of a heavy impurity in a BEC of light and repulsive particles.

The formation of dimer-trimer superposition states appears since the coupling between the dimer and trimer mediated by the BEC is an order of magnitude larger than their difference in binding energies. This provides evidence that the eigenstates we observe are strongly mixed, and amplifies the effect of the higher-order correlations in the system, which would otherwise be extremely challenging to observe. This formation of strongly correlated states due to bound-state formation in presence of particle-exchange with the background medium, is particularly interesting also in the physics of excitons in two-dimensional semiconductors and molecules in superfluid Helium.

The experiment starts with a Bose-Fermi mixture of ^{23}Na and ^{40}K at $\approx 100\,$nK, trapped in an optical dipole trap with trapping frequencies $2\pi \times (108, 112, 9)$ Hz. The BEC has a typical peak density of $n_{\mathrm{B}} \approx 40\mu\mathrm{m}^{-3}$ and the Fermi gas is two orders of magnitude more dilute. We perform rf-injection spectroscopy by driving ^{40}K from its initial spin state, which we denote as $|\downarrow\rangle \equiv |F = 9/2, m_F = -9/2\rangle$, into a final spin state $|\uparrow\rangle \equiv |F = 9/2, m_F = -7/2\rangle$ for which the impurity-boson interatomic potential supports a shallow bound state. By measuring the number of transferred atoms we can extract information about the presence of final states at the probed energy, and importantly, the overlap with these final states and the initial state.

An essential feature of our experiment is that the impurity in its initial state $|\downarrow\rangle$ is already strongly interacting with the bath, with approximately constant $(k_n a)^{-1} \sim -1$ over the range of magnetic fields used, where a is the initial interspecies scattering length and $k_n = (6\pi n_{\mathrm{B}})^{1/3}$ is the inverse interboson distance. This is possible due to the proximity of a broad initial-state Feshbach resonance to the magnetic field range of $100 - 120$G containing the final state resonance, see Fig. 4.3. Indeed, we allow the impurity to form a strongly interacting attractive Bose polaron by letting it thermalize with the bath for 25ms before performing spectroscopy. This boosts the wavefunction overlap with the bound states of interest in the final many-body Hamiltonian, as the BEC density is already strongly enhanced near the impurity. This allows us to drive the rf-transition to final bound states faster than the

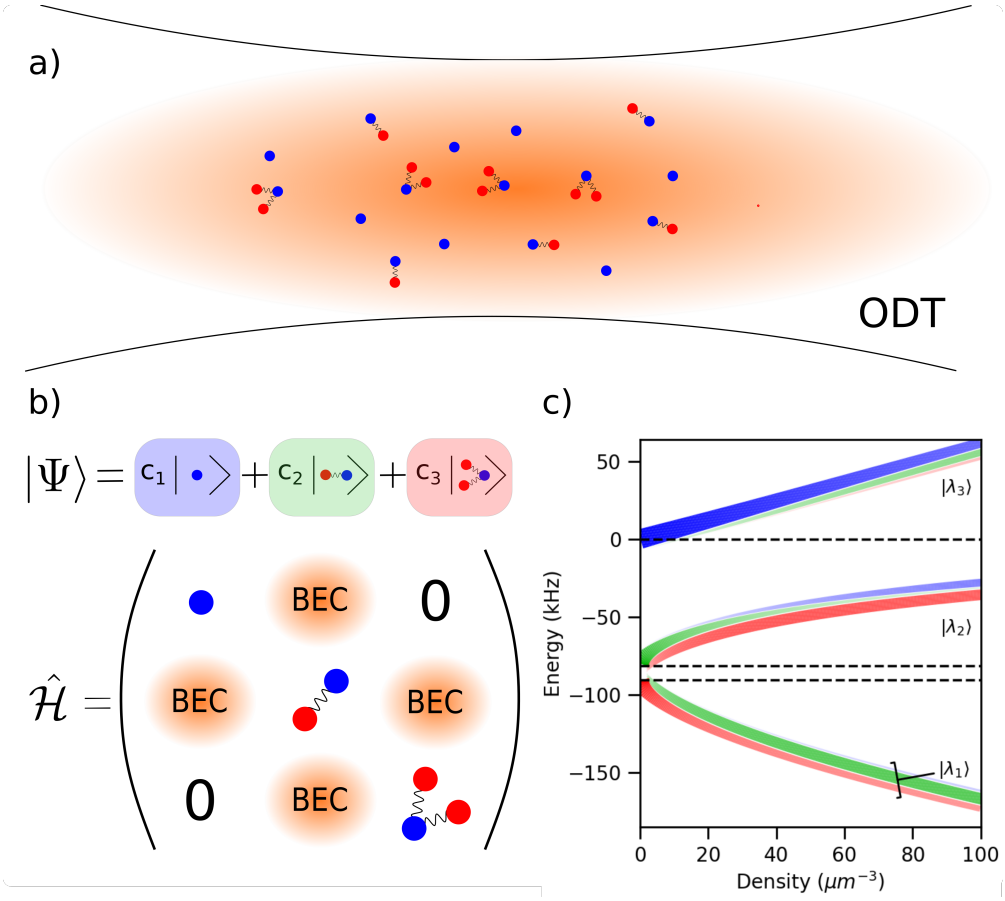

Figure 5.1: Pictorial overview of our work. a) The BEC of ^{23}Na (orange), trapped in an optical dipole trap (ODT), containing ^{40}K impurities (blue) after photo-association. Some impurities bind with bosons from the BEC (in red) to form dimers and trimers. b) The wave function of a single impurity in a BEC forming a superposition of a free impurity, a dimer, and a trimer, and the effective Hamiltonian in the basis of these three states. On the diagonal are the energies of these states and the off-diagonal contributions are due to the exchange of particles with the BEC. c) The energies (in kHz) and structure of the three eigenstates $|\lambda\rangle$ of this Hamiltonian as a function of the density of the BEC in μm^{-3}. The widths and opacities of the colored sub-lines indicate the size of the coefficients (as shown in b)) $|c_1|^2$ (blue), $|c_2|^2$ (green) and $|c_3|^2$ (red) for each of the eigenstates. The horizontal dashed lines indicate the energies of the three basis states in absence of a background BEC.

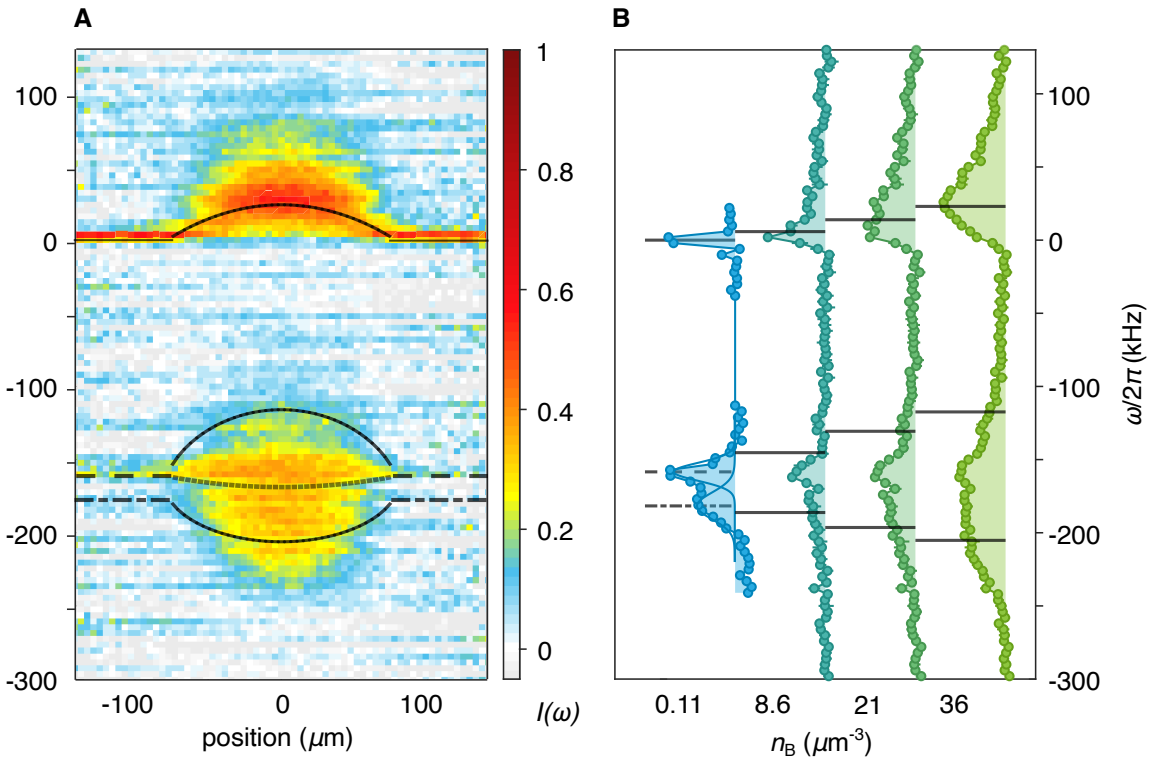

Figure 5.2: (A) The population transfer from impurity spin state $|\downarrow\rangle$ depends strongly on its position within the BEC. We show spatially resolved spectra at $B = 102.5$G measuring the remaining population in $|\downarrow\rangle$ as a function of displacement along the long axis of the cigar shaped trap and the rf-frequency detuning from the bare hyperfine transition. In (B) cuts of Fig. (A) are shown for some boson densities n_{B}. The solid colored lines indicate the theory predictions from the three-level model, whereas the dashed line shows the theory result with at most one excitation from the BEC. Impurities deeply immersed in the BEC show striking deviations from theory predictions only allowing for a single excitation on top of the BEC.

decay of the short-lived final states. Key here is to vary the pulse time with the impurity-bath interaction strength, such that ∼50% of the initial polaron $|\downarrow\rangle$ population is injected into the manifold of bound states. This is necessary as the coupling strength between the initial attractive polaron and bound states changes dramatically near the Feshbach resonance. With this procedure we are able to both deplete the initial population as well as witness the production and arrival of novel molecular states in our experiment.

We naturally observe the effect of the background BEC on the impurity atoms by spatially resolving the rf-signal at different positions in the atomic cloud, as shown in Fig. 5.2a) for the magnetic field of B=102.5G. In Fig. 5.2b) we show a few cuts from Fig. 5.2a), but as a function of the density. The frequency shown is the frequency shift compared to the bare hyperfine transition. The colored lines show the fitting-parameter-free theoretical predictions using a three-level model as depicted in Fig. 5.1b).

5.3 Discussion

At low density in the edge of our cloud, we observe the bare free-to-free and free-to-bound hyperfine transitions. Here we already recognize our first key result: in Fig. 5.2b), we see a clear double peak emerging in the free-to-bound spectrum, which we attribute to the dimer and the trimer states. This marks the first observation of such a weakly-bound trimer state in the Efimov-unfavourable regime. The weights of the two contributions are approximately equal because the transition is saturated.

When the density is increased towards the middle of the cloud, the narrow peaks at low density broaden immensely due to the coupling with the medium. The upper peak shifts upward in energy, due to the formation of a *repulsive polaron*. The lower peak on average shifts to lower energies, due to *attractive polaron* effects. The coupling with the medium is so strong that the lowest energy at which we observe significant signal lies approximately 50 kHz below both the bare dimer and the trimer energies, that is about a third of the binding energy. We are therefore clearly in the strong-coupling regime where the many-body correlations with the medium are equally important as the binding leading to molecule formation.

A key indication that the admixing of both dimer and trimer states is required to explain these results, is the fact that a theoretical description admitting only a single excitation from the medium (indicated by the dashed line in FIg. 5.2a)) does not capture at all the lowest attractive polaron energy. Our theoretical three-level model, as qualitatively shown in Fig. 5.1b) (see [109] for more details), captures the width of the rf-spectrum much better, showing that the qualitative picture is correct. Still, the lowest attractive polaron energy is underestimated. This is likely due to the admixture of states with even higher number of excitations from the medium, and broadening due to three-body loss. The upper solid line of Fig. 5.2a) is the middle line of the three-level model, and this captures well the upper edge of the experimental attractive polaron signal. This shows that the strength of the many-body splitting due to the coupling with the condensate well-matches the experimental picture.

In Fig. 5.3 we see the polaron rf-spectrum as a function of the magnetic field, studying our system over a broad range of impurity-bath final interaction strengths. Focusing first on Fig. 5.3A, we show the spectrum obtained from measuring the atoms transferred from

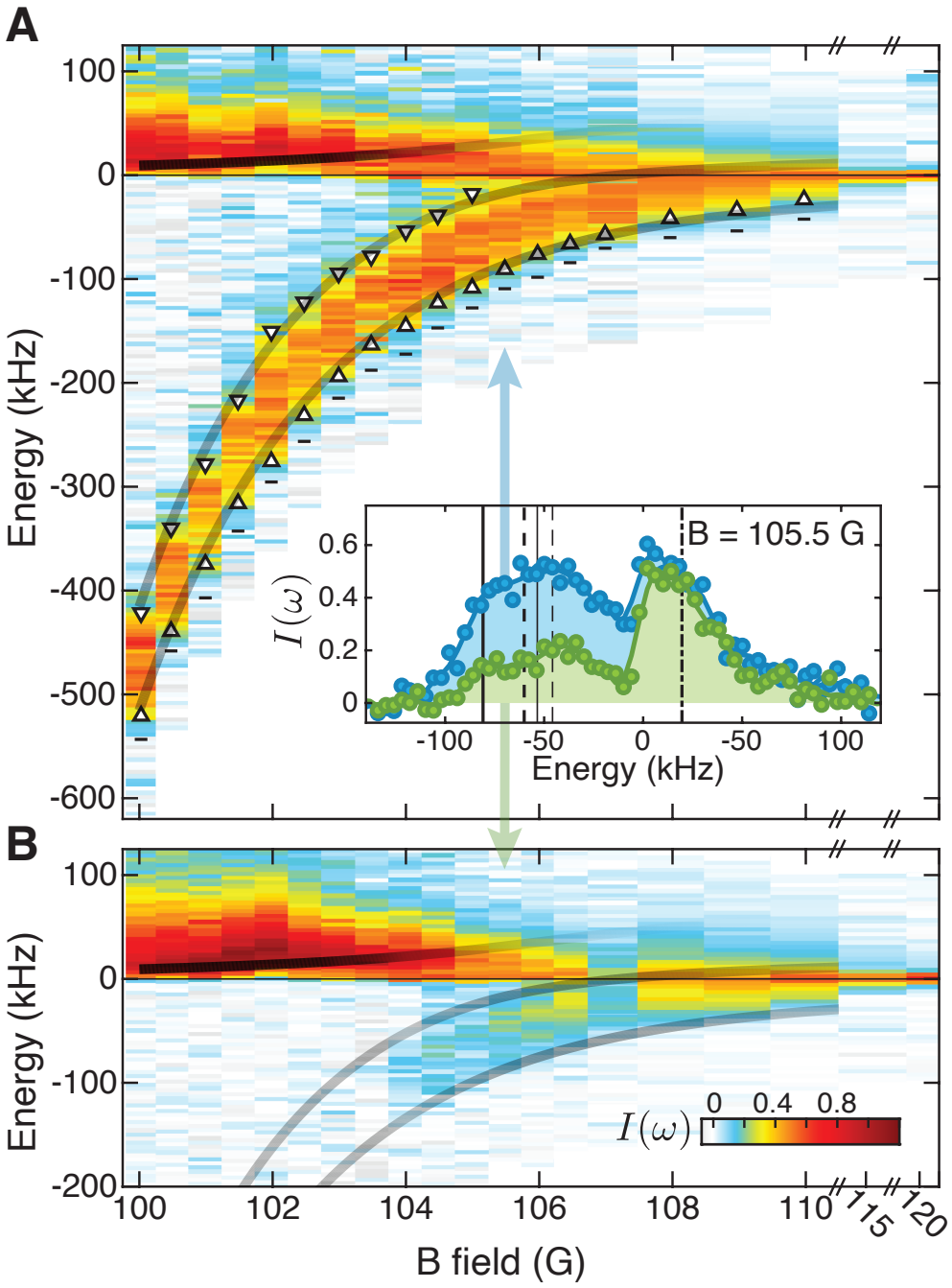

Figure 5.3: Measurement of the RF transfer fraction in the center of the BEC via (A) depletion of $|\downarrow\rangle$ and (B) arrival of $|\uparrow\rangle$. Spectra are taken at various magnetic fields and plotted versus the energy of the final state with respect to the bare impurity state. In the inset a cut is shown of the obtained signal at 105.5G. In (A) the full width at half maximum of the signal is indicated by the triangles. The theory results from the three-level model are indicated via the solid lines, of which the opacity is set by the overlap of the states with the initial polaron state, weighted by the duration of the RF pulse. The horizontal black markers in (A) denote the lowest energies for which nonzero rf transfer was measured in our experiment.

the initial state, and we see again the repulsive and attractive polaron branches. The black horizontal bars in Fig. 5.3A mark the deepest binding energies where we see spectral response, and the threshold behavior we observe on the low-energy flank of the spectra strongly suggests that we indeed observe the ground state of the final state Hamiltonian. The full width at half maximum (FWHM) of the attractive branch is indicated by the triangles, and the theory curves (opaque lines) are computed using the three-level model discussed before. The opacity of the theory curves is given by the overlap of the initial state and weighted by the rf pulse length T_{rf}, which is proportional to the transferred population for pulses within linear response. We additionally note that for B =115, 120G, the interspecies scattering length of initial and final spin states are approximately equal, so despite strong interactions, both branches collapse into a single feature given by the spectral resolution of our probe.

We find that the two lowest energies of the theoretical three-level model reliably describe the FWHM frequencies of the attractive polaron branch over the wide range of interaction strengths explored. Thus, the models accounting for the many-body correlations due to the BEC are sufficient to predict the spectral location and width. However, the accurate computation of the full spectral lineshape is beyond current theoretical approaches. Our experiment provides an excellent testbed for developing theory that also includes the mechanisms of three-body loss and adding phononic excitations on top of the molecular states.

We remark that the peaks of the repulsive polaron branch of the spectra deviate from its theoretical repulsion energy, as shown by the upper opaque line in Fig.5.3A. The repulsive polaron corresponds to a broad continuum of scattering states, which are shifted upward in energy due to the need for the quantum mechanical wave function to be orthogonal to the attractive polaron states. The experimentally determined spectral weights not only depend on the available density of states, but also on the wave function overlap with the initial state. The intricacies of the repulsive polaron lineshape cannot be expected to be captured by the single repulsive polaron line following from our three-level model. However, what is still captured is the decrease in the repulsive polaron spectral weight for increasing positive impurity-boson scattering length.

Fig. 5.3B we show the number of atoms arriving in the final state. Comparing this signal to the depletion signal from Fig. 5.3A allows us quantitatively estimate the decay lifetimes $1/\Gamma$ of the states prepared during the rf injection pulse time. We model transfer between populations $P_\downarrow, P_\uparrow$ as $dP_\downarrow \propto -\Omega_R(t)^2 P_\downarrow dt$, where the Rabi frequency Ω_R is time-dependent due to pulse shaping, and the loss in $|\uparrow\rangle$ as $dP_\uparrow + dP_\downarrow = -\Gamma P_\uparrow dt$. (For more details, see section 5.4.5.) We first are able to observe the arrival of the upper repulsive polaron branch, where losses are weak. However, in the attractive branch the arrival signal is much weaker. The origin of this effect is the final state being short-lived compared to the rf pulse duration. Their short lifetimes can be explained by a significant trimer admixture, and trimers have a short lifetime due to three-body recombination. We find that the lifetime decreases substantially with increasing binding energy. Qualitatively this is to be expected, since the probability that the three particles meet each other at short distance and undergo the recombination reaction increases along with the binding energy.

At the magnetic fields where we are able to detect nonzero population in $|\downarrow\rangle$ in the attractive branch, we observe decay lifetimes $1/\Gamma$ of greater than 50μs. Up to factors order unity, this contributes to a lifetime broadening of $\Gamma/(2\pi) \approx 3$ kHz, whereas the typical spectral widths measured (> 50 kHz, e.g., Fig. 5.4 top left) is at least an order of magnitude

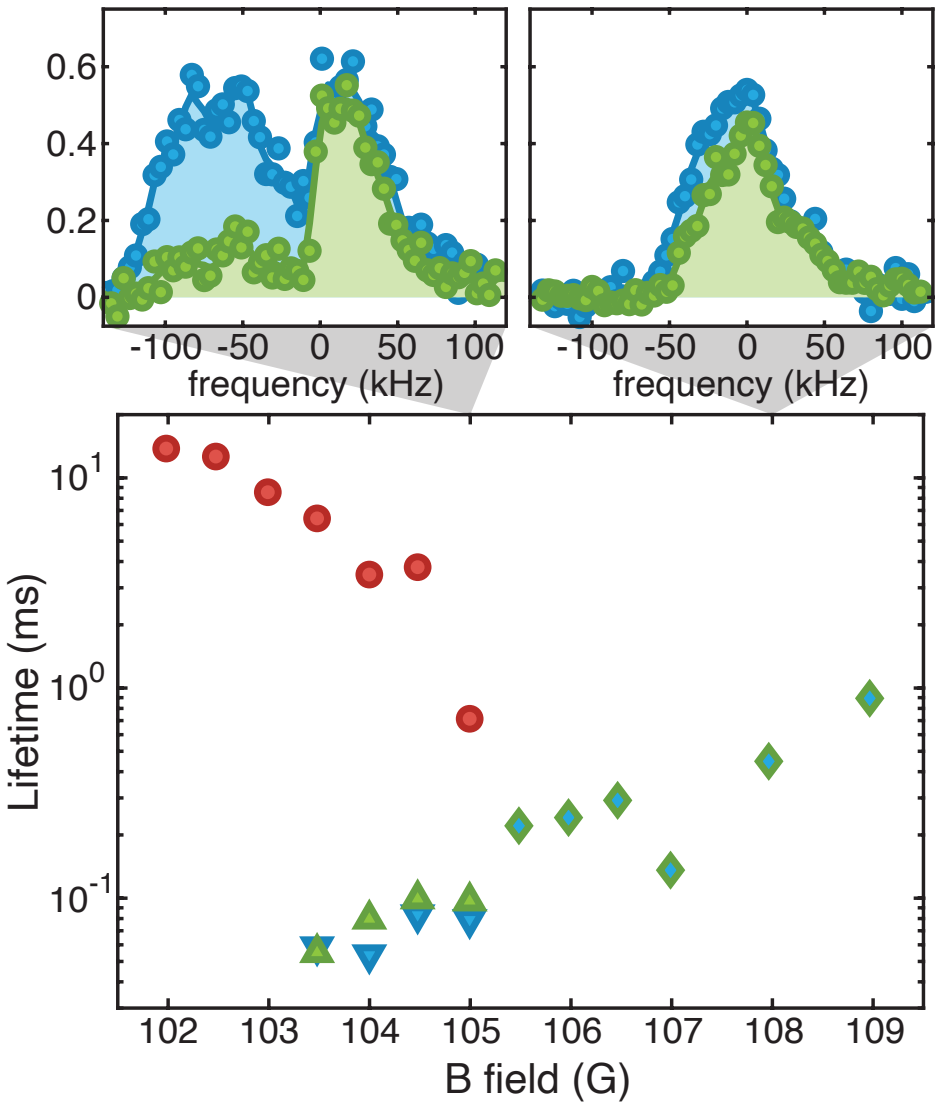

Figure 5.4: The lifetimes of the states created by rf injection are inferred from the ratio of population depleted from $|\downarrow\rangle$ to population observed in $|\uparrow\rangle$, as shown in Fig. 5.3. Population transferred to $|\uparrow\rangle$ during the rf pulse can decay rapidly due to three-body recombination. For data taken at $B \leq 105$G, we are able to resolve the attractive and repulsive branches of the spectrum, whereas for larger magnetic fields the two features merge. This can be seen in the exemplary spectra shown in the top row. The lifetime of the bound states (triangles) decreases at deeper binding energy (away from the Feshbach resonance), whereas the lifetime of the repulsive polaron branch (circles) increases. At sufficiently deep binding energies, we do not observe any population in $|\downarrow\rangle$.

greater. This serves as an additional confirmation that the broad spectra we observe cannot simply be attributed to loss and gives further credence for the many-body interpretation presented above.

The similarity in the structure of the depletion and arrival spectra, for example in figure 5.4 at 105 G, indicates that all bound states have approximately similar lifetimes. This is in obvious contrast with the spectra in figure 4.5 in the previous Chapter 4, where we only witness the arrival of dimers but not trimers, due to their significant difference in decay rates. This is further evidence for the interpretation of the bound states being strongly admixed eigenstates of approximately equal contribution of dimer and trimer character, in the presence of a BEC. In this picture, each state inherits a combination of their decay rates.

5.4 Additional details

5.4.1 Interpreting our experiment through the lens of bound-to-bound spectroscopy

As discussed in Chapter 1, the work in this chapter and in Chapter 5 of Y. Ni's thesis, "A new pathway to the dipolar molecule ground state from Bose polarons" [41], followed up on several key findings from [38]. Namely, we could create Bose polarons, well-defined quasiparticles in a long-lived metastable state with ∼ms lifetime and ∼10s of kHz binding energies, and the high frequency tails of the rf spectra revealed that strong interspecies interactions indeed resulted in enhanced short-range correlations between Na and K atoms (see section 5.1 "Contact is all you need" from [41]). In fact, the strong interactions, beyond allowing the formation of the internal polaron structure, also resulted in an effect where the Na BEC essentially acted as an additional trapping potential, attracting K atoms towards its center, as shown in figure 5-4 of [41]. This suggested that leveraging the interactions in a Bose-Fermi mixture to first form Bose polarons could improve the overall conversion efficiency of atoms to molecules. One can entirely bypass the Feshbach molecule association step, as done in [41], or as we discuss, explore if the rf association efficiency from atoms to Feshbach molecules would benefit an initial state with enhanced short-range correlations.

This idea was originally conceived thinking in the framework of bound-to-bound transitions in a two-body setting. There, we expect that the rf spectrum should have a delta-like feature due to the discrete nature of the two states we couple, located at a frequency given by the difference in binding energies between the states [110]. Generalizing this line of thinking to the many-body setting we work with in this chapter, the initial state would be the attractive polaron (prepared on the attractive side of the Feshbach resonance), and the final state would be a Feshbach dimer, as we show in figure 5.5 b.

With the benefit of hindsight, we know that going from the two-body to the many-body setting introduces qualitatively new physics. We have already seen in the previous chapter that even simply going from the two to three atoms reveals a trimer state with similar binding energy to the dimer. In the many-body regime, the presence of a dense bosonic bath and high-order correlations gives rise to additional rich phenomena. Indeed, we emphasize that the final states we are studying are not simply the Feshbach dimer; they are the attractive Bose polaron on the repulsive side of the Feshbach resonance, as shown in figure 5.5a.

To briefly illustrate the theoretical challenge in modeling this scenario, we give a few examples. Levinsen and colleagues show that even for the case where no three-body bound states exist "in a vacuum" (i.e., if we had no such trimer state as discussed in Chapter 4), the effects of three-body correlations are crucial in calculating the Bose polaron's properties, including energy and quasiparticle residue [111]. Separately, in a simplified picture without interboson repulsion, we can have a collapse, an infinite ladder of states corresponding to any integral number of bosons binding to a single impurity, each adding its own binding energy [59]. And, as discussed in the introduction, we can have a situation where the BEC acts as a coherent reservoir and can cause mixing between states of different boson number, and this is our case.

5.4.2 Bose polarons on the repulsive side of the Feshbach resonance

To date, there have been several other ultracold atom experiments [112]–[114] studying the attractive branch of the Bose polaron where two-body bound states are supported in the few-body limit. In all the cited references, the peak position of the spectral feature (inferred rather than directly measured for the case of interferometry experiments) shows no significant difference from the binding energy of the Feshbach dimer, i.e., what we would expect from few-body physics. The most convincing evidence of that many-body effects play a significant role comes from the ^{39}K experiment performed in a box trap at the University of Cambridge [114]. In this experiment, J. Etrych et. al demonstrate a universal scaling between the width of their measured spectral feature and the density of the bath n_B (scaling as $n_B^{2/3}$), presenting this as evidence for the "many-body state(s) with attractive-polaron character." We are currently still investigating whether the level-repulsion in our effective three-level model has a similar scaling or if it can be distinguished from this observation.

5.4.3 Measurement of the polaron ground state energy

We will first compare and review several previous experimental works on polaron spectroscopy before drawing parallels to the work presented in this chapter. These experiments followed either the *injection* [93], [115] or *ejection* [38] spectroscopy procedure, where the initial or final impurity internal state is non-interacting with the Bose bath, respectively. A key advantage of the non-interacting initial state in the injection procedure is that its three-body loss rate is strongly suppressed compared to the strongly interacting final state, and therefore a long-lived sample can be prepared prior to interrogation with an rf drive. In contrast, in the ejection protocol, one attempts to prepare the sample by allowing the system to relax into strongly interacting Bose polarons in their ground state, and here one must take care to avoid losing the sample entirely due to strong losses as the system relaxes. The advantage of the ejection protocol, assuming that one has prepared polarons only in their ground state, is the ability to then directly probe its properties, e.g. its contact.

Quantitative interpretation of these spectra, e.g., estimating a polaron's ground state energy, requires the protocol used to be taken into account. As an example, it is shown in supplementary material of [38] that injection and ejection spectroscopy experiments on the same system can produce drastically different lineshapes, with the peak of the injection

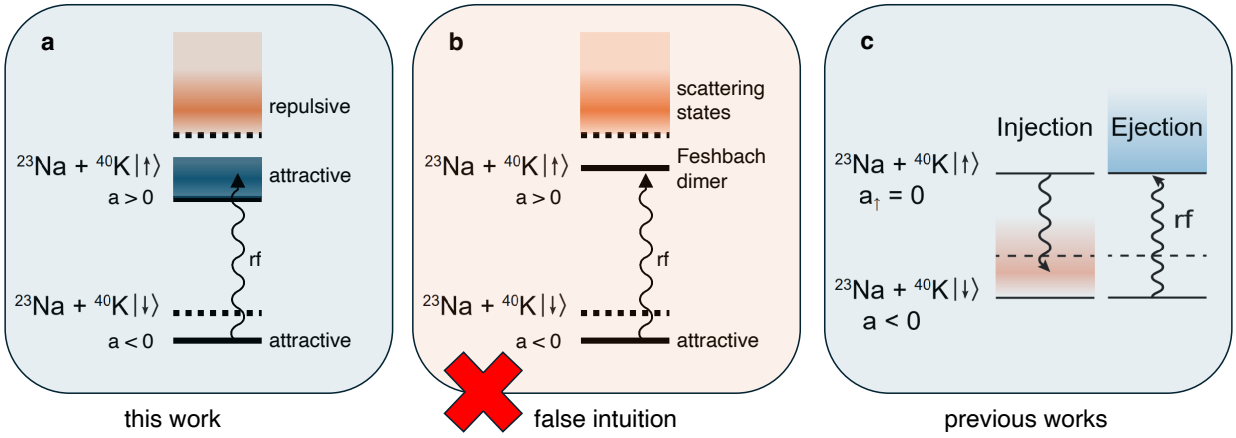

Figure 5.5: Our experiment (a) is an example of bound-to-bound spectroscopy that does not exhibit a delta-like spectrum, as one might expect with the intuition shown in (b) which neglects the many-body nature of the final state. It also deviates from the typical injection and ejection protocols shown in (c). Subfigure (c) reproduced from the supplementary material of [38].

spectrum lying much closer to the threshold. The key idea is that while a non-zero density of states at the energy bridged by the rf drive is required for population transfer, the wavefunction overlap between initial and final states can additionally modify this lineshape. Therefore, the peak position of a measured spectra cannot be directly interpreted as the ground state binding energy, although this is typically the most intuitive feature to compare between experimental measurements and theoretical predictions of the binding energy. Depending on whether the injection or ejection procedure is used, it can be a systematic under/overestimate of the true binding energy.

The ground state energy of a quantum system is a standard observable to compare between theory and experiment, and to obtain an accurate measurement, we use a novel spectroscopy protocol, as shown in figure 5.5a. This is because neither the typical injection or ejection methods are satisfactory for this purpose. It is experimentally challenging to prepare our system in this state to perform ejection spectroscopy, due to the short lifetimes (compared to required rf pulse durations) as measured in Figure 5.4. However, following the typical injection protocol by starting with a non-interacting initial state (no correlations with the bath) hinders coupling into states with strong correlations, including the ground state, due to poor wavefunction overlap.

Therefore, we choose both states in our experiment to have finite interspecies interactions, and this can be described as an injection protocol with a strongly interacting initial state. We prepare a state with correlations already present, and probe the final states available at even stronger interactions. This method of initial state preparation enhances coupling into the states with high-order correlations, and in principle the threshold of our spectra should place a tighter upper bound on the Bose polaron ground state energy, given an accurate measurement of the binding energy of the initial state.

We find experimentally that the low frequency threshold of our spectra does not show

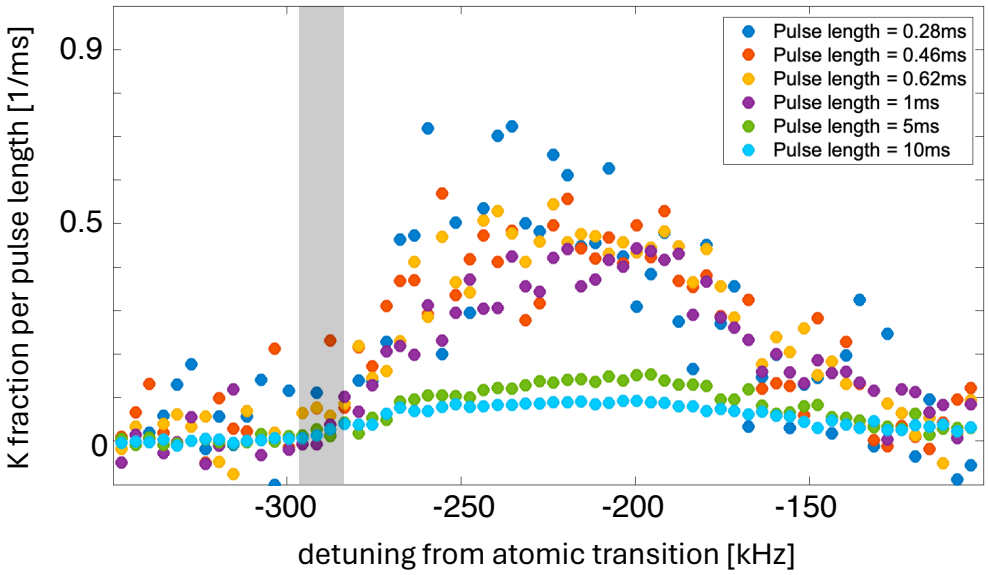

Figure 5.6: Polaron spectra taken with pulse times ranging from 0.28 – 10 ms at an external field of $B = 102$ G. The data shown here is from the densest central region of the BEC. The grey shaded region is a guide to the eye, marking the low frequency threshold where we begin to detect population transfer. The rates of population transfer for data taken with pulse lengths between 0.28 and 1 ms are overlapping, whereas the 5 and 10 ms data are significantly lower due to saturation. Credit to Carsten Robens for generating an earlier version of this plot.

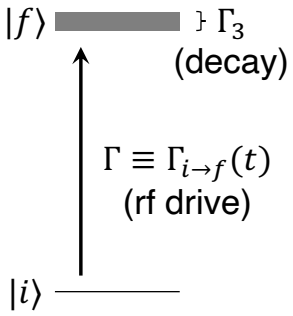

Figure 5.7: Atoms are prepared in state i, and driven via $\Gamma(t)$ into state f which has decay rate Γ_3.

any obvious dependence on the rf pulse length, as shown in figure 5.6. This has two possible interpretations. Either there exist states of even lower energy beyond the measured threshold, but with wavefunction overlap to the initial state that suddenly falls off at the threshold, or that the threshold indeed marks the position of the ground state.

5.4.4 Local density approximation

Our atomic mixture is trapped in a harmonic trapping potential (not a box), and therefore both the initial impurity K density and BEC density are spatially varying. This may initially seem like an annoyance, since we are measuring effects that depend strongly on the density of the BEC, and therefore trap averages blur out these effects[1]. The flip side of the coin is that by taking experimental images *in situ*, in every image, we sample over a wide range of BEC densities, and by examining the rf spectra as a function of space, relative to the center of the BEC where it is the densest, we can measure density-dependent effects within a single image! The details on how to approximate the local density are in section 3.4.3 of [64].

5.4.5 Bound state lifetimes

Here we will describe how we infer the lifetime of the bound states. The lifetime of a quantum state can be estimated by driving a transition into that state, with a known pulse shape and measurements of the initial and final state populations after the pulse. If we neglect coherence (e.g. Rabi oscillations) and assume a one-way transfer, the rate equations we present precisely describe the dynamics.

Let us denote the initial and final state populations by $P_i(t)$, $P_f(t)$, and assume the initial conditions $P_i = 1, P_f = 0$. The coupled rate equations which describe the experiment are

$$\frac{dP_f}{dt} = -\frac{dP_i}{dt} - \Gamma_3 P_f(t)$$
$$\frac{dP_i}{dt} = -\Gamma(t) P_i(t),$$

[1] In fact, our analysis does not remove the blurring effects of line-of-sight integration, so some degree of this problem persists.

and this is schematically shown in figure 5.7. Γ_3 denotes the final state decay rate (subscript standing for three-body loss), and $\Gamma(t)$ denotes a time-dependent transfer rate (as in Fermi's golden rule), with the time dependence arising from the pulse shape used to drive the transition.

We can integrate the differential equation for P_i,

$$P_i(t) = P_i(0) \exp\left(- \int_0^t \Gamma(t')dt' \right).$$

We now consider a few special cases. For a square pulse, simple closed form solutions exist. For a Blackman pulse of total length T (and typically $\alpha = 0.16$),

$$\Gamma(t) = \Gamma_0 \times \left(\frac{1-\alpha}{2} - \frac{1}{2}\cos\left(\frac{2\pi t}{T}\right) + \frac{\alpha}{2}\cos\left(\frac{4\pi t}{T}\right)\right)^2.$$

Notice that the quantity in the large brackets is proportional to the electric field driving the rf transition. The change in population is proportional to the power, so the quantity is squared.

The integral to give P_i is

$$\int_0^t \Gamma(t')dt' = \frac{\Gamma_0}{192\pi}[24\pi(\alpha(3\alpha-4)+3)t + 24(\alpha-2)T\sin\left(\frac{2\pi t}{T}\right) +$$

$$6(1-4(\alpha-1)\alpha)T\sin\left(\frac{4\pi t}{T}\right) + \alpha T(3\alpha\sin\left(\frac{8\pi t}{T}\right) - 8\sin\left(\frac{6\pi t}{T}\right))].$$

This can then be substituted into the equation for P_f. Note that the integral over the pulse duration T is

$$\int_0^T \Gamma(t')dt' = \frac{\Gamma_0}{8}(\alpha(3\alpha-4)+3)T.$$

In an experiment, we measure the populations at the end of the Blackman pulse, i.e. we are given $P_i(T), P_f(T)$. From the population remaining in the initial state at the end of the pulse $P_i(T)$, we can solve for Γ_0,

$$\Gamma_0 = -\frac{8}{(\alpha(3\alpha-4)+3)T}\log(P_i(T)).$$

We then numerically integrate $\frac{dP_f}{dt}$ (with a solver, e.g. MATLAB's ode45) to numerically solve for the remaining unknown, Γ_3, using our measurement of the surviving population at the end of the pulse in the final state, $P_f(T)$.

5.4.6 Raman shelving between hyperfine manifolds in ^{40}K

We used a carefully crafted shelving protocol to measure populations of ^{40}K in $|\downarrow\rangle$ and $|\uparrow\rangle$ to infer the lifetimes of the bound states discussed in the previous sections. A simple scheme (used in the work of the previous chapter) is shown in figure 5.8. One of the main problems of this scheme is that the σ_- transition driven by the imaging light on state

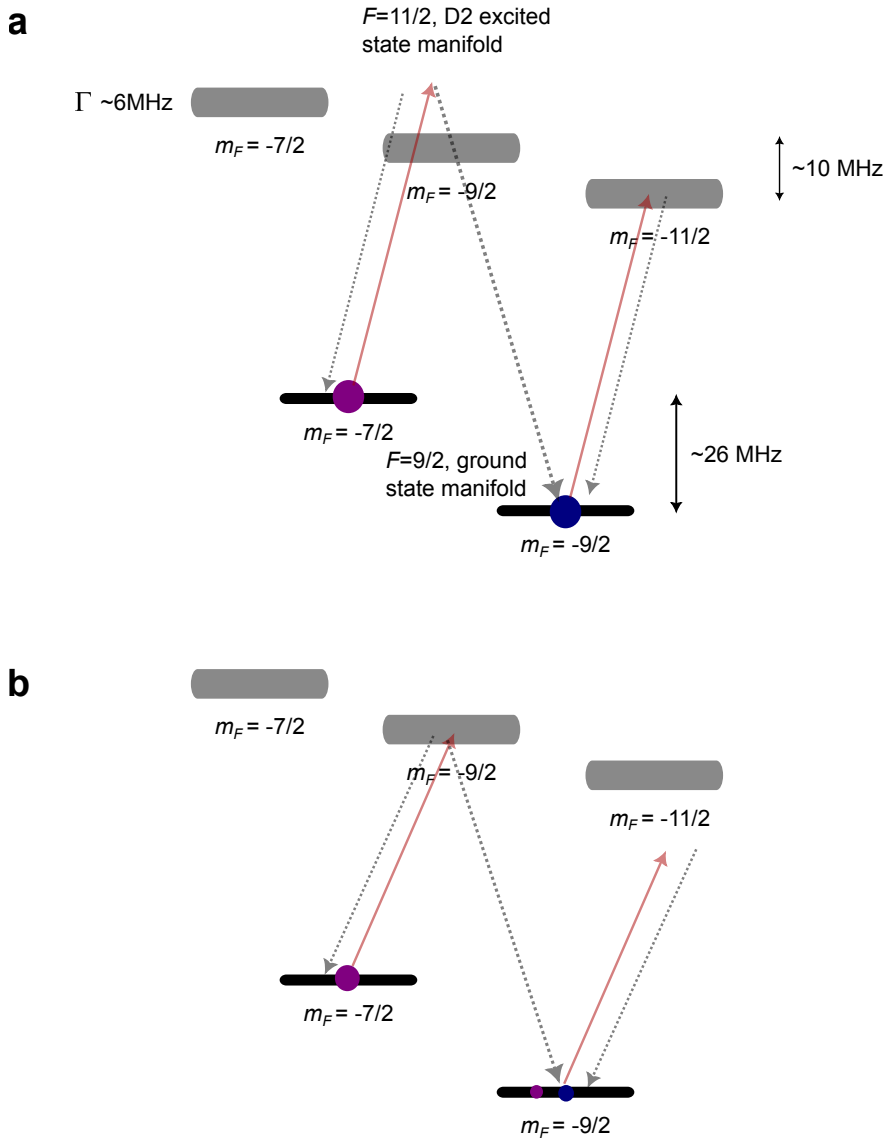

Figure 5.8: A simple spin-resolved imaging scheme for ^{40}K states in the $F = 9/2$ ground state manifold, driving σ_- transitions with a natural linewidth of ≈ 6 MHz. The level structure is shown for an external magnetic field of $B \approx 100$ G. Solid arrows depict the light, while dashed arrows represent spontaneous decay channels, and solid circles indicate atomic populations at the start of each stage. Experimental imperfections in the imaging light polarization further complicates this process, but we ignore this as a first-order approximation. The main imperfections in this imaging scheme arise from the non-cycling nature of the transition driven in (b) and significant off-resonant scattering rates. (a) First, we primarily image $m_F = -9/2$, driving resonantly on the cycling σ_- transition. Photons can also be off-resonantly scattered by atoms in $m_F = -7/2$. This imaging process is almost entirely destructive in that repeated photon scattering causes the atoms to heat up, moving out of the imaging plane and possibly becoming un-trapped. However, a small fraction of atoms can remain as shown by the small circles in (b). (b) Next, we primarily image $m_F = -7/2$, driving resonantly on the non-cycling σ_- transition.

$|F = 9/2, m_F = -7/2\rangle \equiv |\uparrow\rangle$ is not cycling, while the analogous σ_- transition driven by the imaging light on state $|F = 9/2, m_F = -9/2\rangle \equiv |\downarrow\rangle$ is. As a result, whenever atoms in $|\uparrow\rangle$ are exposed to resonant (or near-resonant) σ_- light, they are optically pumped into the $|F = 9/2, m_F = -9/2\rangle \equiv |\downarrow\rangle$. Furthermore, since our experimental apparatus does not have the capability of imaging two different spin-states of ^{40}K simultaneously and *in situ*, this optical pumping effect unavoidably causes us to overestimate the $|\downarrow\rangle$ population and underestimate for $|\uparrow\rangle$.

Furthermore, due to the atomic structure of ^{40}K in an external B-field of ~ 100G (see figure 5.8), both the light resonant with the σ_- transition used to image $|F = 9/2, m_F = -7/2\rangle \equiv |\uparrow\rangle$ *and* the light off-resonant by $\Delta \approx 16$MHz (for $|\uparrow\rangle$) used to image $|\downarrow\rangle$ have non-negligible scattering rates which contribute to optical pumping. The scattering rates R_{sc} can be approximated from the familiar Lorentzian lineshape for a closed two-level system $R_{sc} \propto 1/(1 + 4(\Delta/\Gamma)^2)$ in the absence of saturation, where the natural linewidth $\Gamma \approx 6$ MHz for the ^{40}K D2 transition we use. Their ratio is $R_{sc}^{\text{off-resonant}}/R_{sc}^{\text{resonant}} \approx 3\%$. Without shelving implemented, the natural choice is to choose the lesser of two evils and image $|\downarrow\rangle$ first, which contaminates the population measurement of $|\downarrow\rangle$ with population in $|\uparrow\rangle$ due to the $\approx 3\%$ off-resonant scattering rate. After this, $|\uparrow\rangle$ (which has been partially depleted due to optical pumping) is imaged, and this signal is also contaminated by residual population in the complementary state $|\downarrow\rangle$.

Our imaging procedure (absorption imaging) cannot distinguish between photons scattered on the desired resonance and those scattered off-resonantly. Using the equilibrium off-resonant scattering rate calculated for a closed two-level system neglects the fact that the optical pumping process is dynamical, and this fact means that any attempt at calibration and correction is also sensitive to the intensity and duration of the imaging laser pulses applied, as well as the density of the atoms we are measuring. To avoid this to first order, we implement a more sophisticated imaging procedure, as shown in figure 5.9, which shelves the state $|\downarrow\rangle$ into a different hyperfine manifold (into state $|\text{aux}\rangle = |F = 7/2, m_F = -7/2\rangle$) while $|\uparrow\rangle$ is imaged. Upon the completion of imaging $|\uparrow\rangle$, the $|\downarrow\rangle$ population stored in $|F = 7/2, m_F = -7/2\rangle$ is un-shelved back to its original state and imaged. Any $|\uparrow\rangle$ population optically pumped into $|\downarrow\rangle$ during imaging is transferred into $|\text{aux}\rangle$. Therefore "leakage" of population signals between the two images is avoided entirely (up to the fidelity of the shelving pulse), and the primary limitation of this scheme is that the population in $|\uparrow\rangle$ is underestimated due to optical pumping during its imaging.

The main physical constraint in our implementation of this shelving sequence for this particular experiment is the lifetime of the bound states we are probing ($\ll 1$ ms). The microwave Rabi frequency available to drive the shelving/unshelving transition at the time of performing this experiment was insufficient for our purposes. Therefore, we implemented the shelving protocol using a two-photon Raman transition, launched onto the atoms in the experiment via the optical path typically used to deliver the "upleg" STIRAP light, with the optics being suitable due to their similar wavelengths. The ability to deliver energy to the atoms in a focused spatial mode allowed us to achieve a maximum two-photon Rabi frequency $\Omega_{2\text{ph}} \gtrapprox 2\pi \times 500$ kHz, with a one-photon detuning of $\Delta \approx -20$ GHz from the ^{40}K D1 transition (measured on the wavemeter), using ≈ 40 mW of optical power. Compared to the ≈ 10 W of microwave power that we can typically deliver near the experimental chamber, we are able to perform our shelving pulses in $\leq 10\mu$s with much less power. The

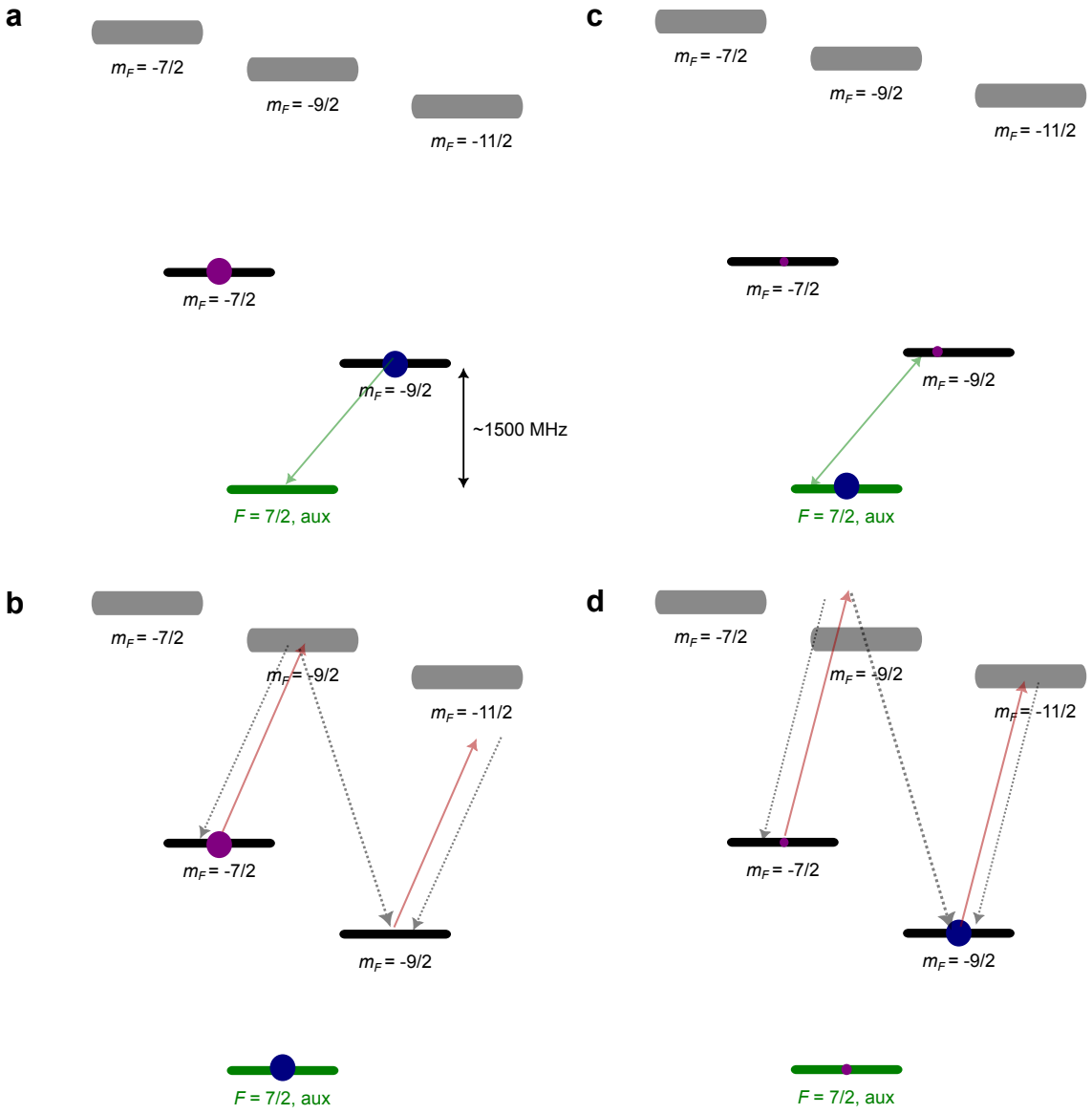

Figure 5.9: By introducing shelving to an additional auxiliary state in the ground hyperfine manifold $F = 7/2$, we can avoid some of the imperfections, primarily leakage of $m_F = -9/2$ signal into the $m_F = -7/2$ image, as discussed in section 5.4.6, by almost entirely eliminating unwanted off-resonant scattering. The symbols used in this figure are defined in figure 5.8. (a) First $m_F = -9/2$ is shelved to $F = 7/2$, via a two-photon Raman pulse. (b) The $m_F = -7/2$ state is imaged resonantly. Note that there is no $m_F = -9/2$ population that can off-resonantly scatter photons. (c) The shelved population stored in $F = 7/2$ is returned to its original state, $F = 9/2, m_F = -9/2$. (d) Finally the $m_F = -9/2$ population is imaged. The $F = 7/2$ auxiliary state is higher in energy than the $F = 9/2$ manifold, but is shown below it for visual clarity.

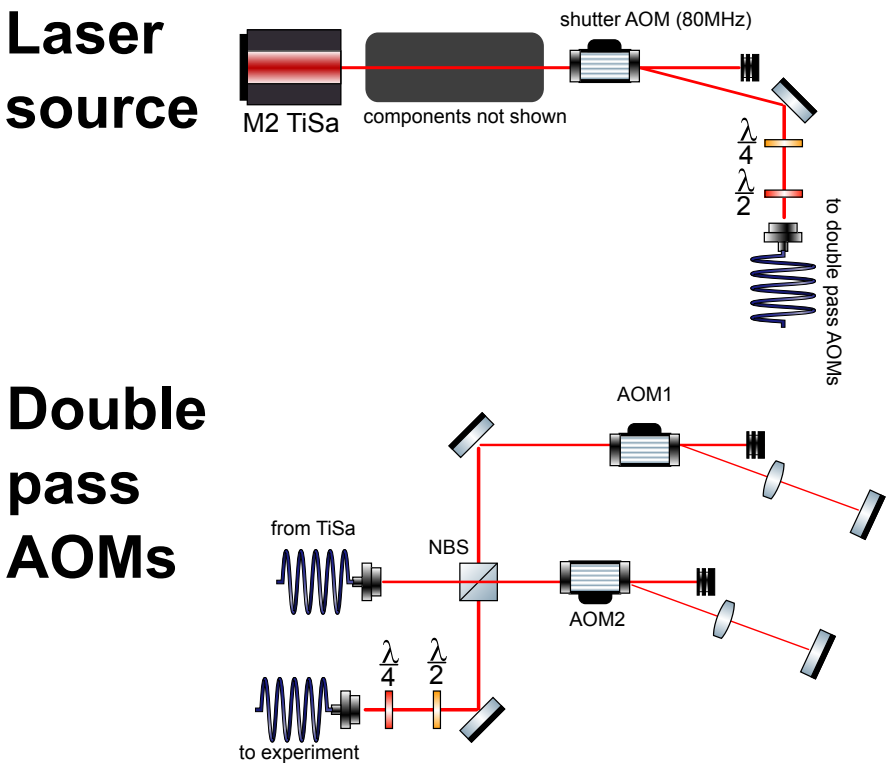

Figure 5.10: There are three AOMs in our setup to modulate the frequency and intensity of the light driving the two-photon Raman transition (mechanical shutters not shown). The shutter AOM provides an overall pulse envelope, while each double-pass AOM creates one of the two tones needed to drive the Raman transition, with twice the sum of their rf driver frequencies setting the two-photon detuning. The double-pass AOMs are 400 MHz resonant devices from Intra-Action, and the overall efficiency of the "Double pass AOMs" setup is $\approx 13\%$. The light originates from a M2 TiSa with coarse frequency stabilization provided by an etalon lock and verified to have one-photon detuning $\Delta \approx -20 \pm 1$ GHz from the ^{40}K D1 line. To implement an adiabatic pulse, (1) the shutter AOM is driven with a constant frequency but time-varying truncated Gaussian envelope, and (2) AOM1 is driven with an rf source chirped synchronously with the envelope applied to the shutter AOM. AOM2 is driven with a fixed-amplitude, fixed-frequency rf source. This optical setup can be verified to work by using a GHz bandwidth photodiode on the experiment side to measure a beat note between the two tones. Icons from ComponentLibrary by Alexander Franzen.

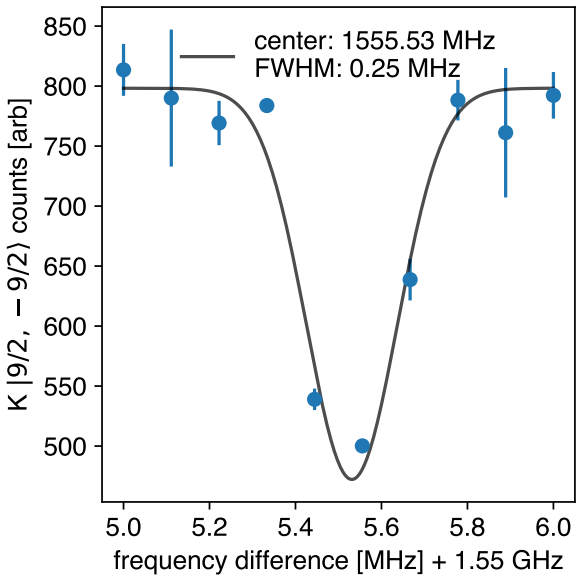

Figure 5.11: We take a two-photon spectrum measuring population depletion from $|\downarrow\rangle$ by driving into $|\text{aux}\rangle$ with a two-photon pulse-averaged Rabi frequency of $\approx 2\pi \times 250$ kHz and a 10μs Gaussian pulse. Shown on the horizontal axis is the twice the sum of the rf drive frequencies applied to AOM1 and AOM2. Spectrum taken at $B = 106$ G. Data is fitted with a phenomenological Gaussian function.

one drawback of using a focused beam of laser light is that it also imparts a mechanical force on the atom cloud and can induce breathing and sloshing oscillations that distort the atoms' spatial profile.

To locate the two-photon transition of interest, we first performed two-photon spectroscopy. As an example, figure 5.11 shows a spectrum taken at $B = 106$ G. The two-photon resonance condition experimentally found at ≈ 1555.5 GHz differs by 100 kHz from the splitting between $|\downarrow\rangle$ and $|\text{aux}\rangle$ naively calculated using the hyperfine structure of ^{40}K in an external B-field of $\Delta E/h = 1555.6$ GHz. We attribute this to differential AC Stark shifts on the hyperfine states of interest due to the light field, but we did not investigate this in further detail experimentally.

To ensure robustness of this optical shelving pulse over drifts in the optical power, one-photon detuning, and two-photon resonance condition, we implement the analogue of a one-photon Landau-Zener pulse, for a two-photon transition [116]. This can be achieved by frequency modulating one tone in the light such that the two-photon δ detuning crosses through the resonance, and simultaneously amplitude modulating the entire light pulse with a truncated Gaussian envelope. The amplitude modulation ensures that the mixing angle θ given by $\tan(2\theta) = \Omega/\Delta$, where Ω, Δ are the two-photon Rabi frequency and detuning, smoothly ramps over $[0, \pi]$[2]. This is otherwise impossible, since in practice we cannot sweep

[2]If a geometric picture is preferred, θ defines the precession axis on the Bloch sphere describing the two-level system spanned by $|\downarrow\rangle, |\text{aux}\rangle$, which ideally starts at one pole and ends at the other in an adiabatic ramp.

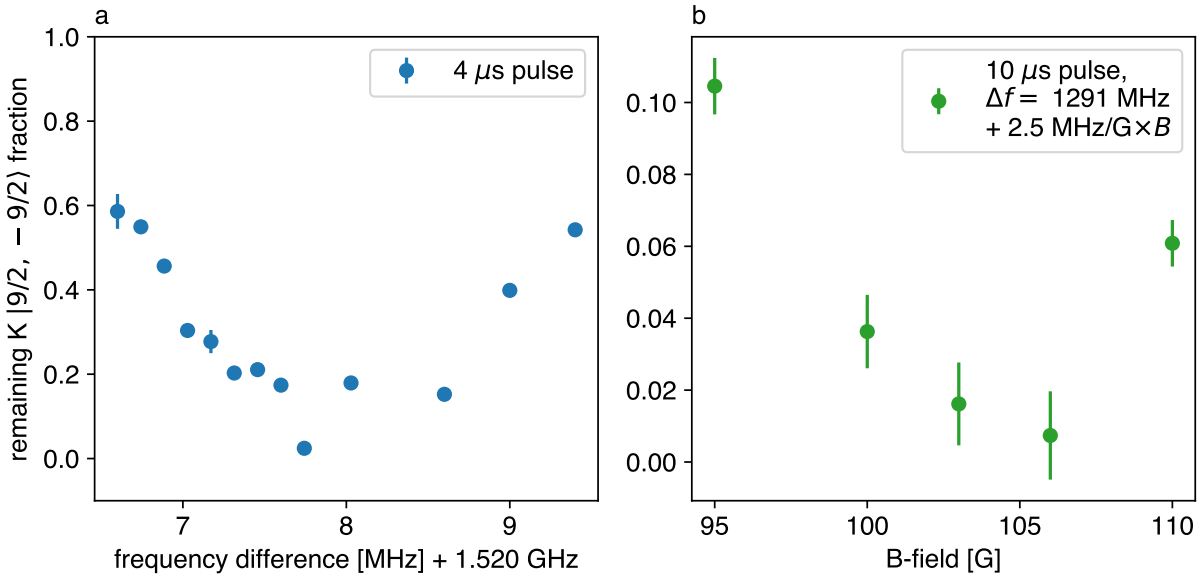

Figure 5.12: We apply a single adiabatic pulse with varying center frequency. Populations are normalized using a separate measurement without the pulse (not shown). (a) At $B = 95$ G, we find a a spectral feature with FWHM of ≈ 2 MHz, indicating the scale over which drifts in the two-photon resonance condition do not significantly impact the shelving fidelity. (b) We use the linear interpolation formula to set the difference frequency $\Delta f = 1291\text{MHz} + 2.5\text{MHz/G} \times B$ for B-fields between 95–110 G. We see an improvement in the fidelity at 95 G compared to (a) due to the longer pulse duration. The variation in fidelity observed is due to the frequency dependence of the diffraction efficiency of AOM1 and AOM2 (and thus the two-photon Rabi frequency and adiabaticity of the pulse), which were statically aligned to be maximal for the frequencies at 106 G.

the two-photon detuning starting/ending with $\delta = \pm\infty$. This is implemented as shown in figure 5.10.

This shelving procedure is robust to drifts of the two-photon resonance condition and provides fidelities of $\gtrapprox 90\%$ over a range of 15 G with a static alignment of the optics shown in figure 5.10. The measured fidelities are shown in 5.12.

Because the fidelity measured by a single pulse is sufficiently close to unity at $B = 106$ G, we perform a more precise measurement by repeated applications of the shelving pulses. We find $F = 99.2\%$, as shown in figure 5.13, by assuming that the state of the atoms after N pulses is modeled by the parity of a binomial random variable with N trials and success probability F. This model neglects the coherent nature of this process but serves as a reasonable first approximation.

5.5 Conclusion

Our study provides experimental observation of conceptually novel molecular states in a superposition of two- and three-body bound states, induced by coupling to a degenerate

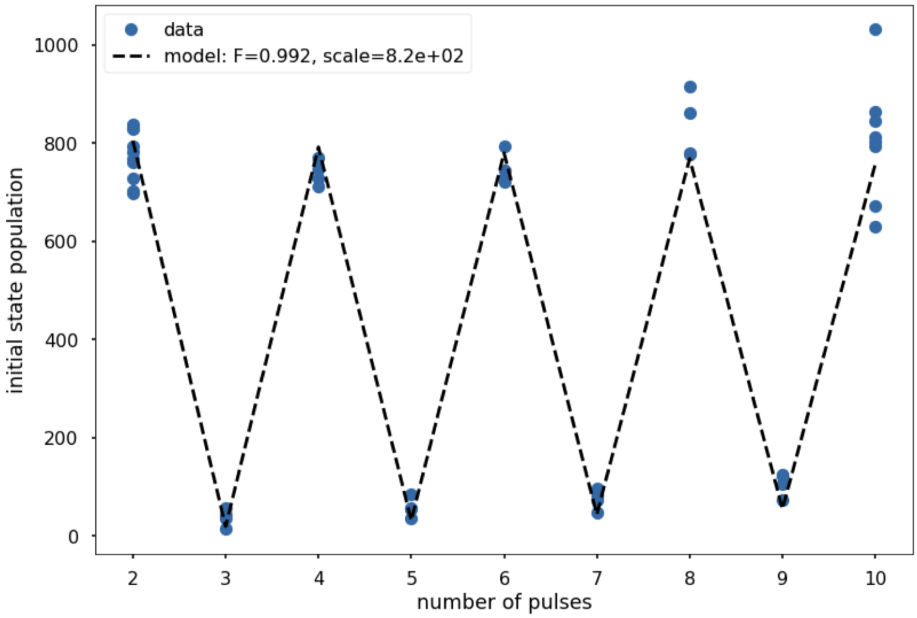

Figure 5.13: We measure the fidelity of the shelving pulse by repeated applications at 106 G. Vertical axis shown is in arbitrary units. For an ideal pulse, we expect unity revival of the initial population after even numbers of pulses, and zero population for odd. We infer a fidelity of $F = 99.2\%$.

bosonic bath. We find that the mixing induced by the background field causes strong level repulsion, setting one of the dominant energy scales in our spectra. We show that by preparing an initial metastable polaronic state, we are able to probe the unexplored crossover between few- and many-body physics of fermions immersed in a BEC within experimentally meaningful timescales. Furthermore, our measurements provide an excellent testing ground for both existing and developing theories of polaron systems.

Our work opens the door into several new directions, spanning from fundamental questions on the role of quantum coherence in polaron physics to the present challenges in ultracold atomic and molecular gases. There are conflicting theoretical results on the finite temperature properties of the Bose polaron [117]–[120], and it remains to be explored to which degree the coherence that accompanies the high density and low temperature of the bosonic bath is essential to observing the CKM-like hybridization effects. Such experiments could be implemented cleanly in homogeneous trapping potentials [121], where the spatial density is decoupled from temperature. We separately raise the experimental question of whether the existence and proximity of few-body bound states is a fundamentally limiting loss mechanism on the road to efficient creation and quantum degeneracy of molecular gases, when starting from degenerate atomic quantum mixtures near a Feshbach resonance [104], [122]. We shed light on this process with spectroscopic precision by revealing many-body correlations and finite final state lifetimes of impurities immersed in a quantum bath.

Chapter 6

The transition to labscript

For my first four years as a student in Fermi1, the daily operation of starting up the apparatus[1] and then taking and analyzing data was, to be frank, quite chaotic sometimes. This was in part because the various necessary tasks had been scattered across a multitude of tools, and there was not much of a unifying theme or architecture to guide our workflow. In this chapter, we will discuss the state of affairs using Cicero and the improvements upon migrating to labscript. Both Atticus/Cicero and organically-grown bespoke MATLAB code[2] written by Carsten Robens, Yiqi Ni, and myself were responsible for control of the lab hardware and storage of experimental logic. Data storage and retrieval was at first orchestrated largely manually (e.g., physical lab notepads or tables in manually populated Igor files). In the interim period before fully transitioning to the labscript-suite, it was handled by a bespoke client Eric Wolf and I wrote together, built on top of a Google Cloud SQL-based solution developed by Biswaroop Mukherjee for the Fermi3 lab and ported over to Fermi1.

The existing system enabled all of the wonderful science that had been done in Fermi1 during the pre-labscript era, including the work described in Chapter 5. It represents years of hard work from both my predecessors in Fermi1, as well as others, such as Aviv Keshet, who implemented many of the features in Cicero as requested by the CUA community, and we should appreciate the foundation it allowed us to build on. Some of the motivations and recommendations described in this chapter are strongly opinionated[3], and the presented arguments are meant to be constructive criticisms. This chapter is written to empower future lab members in their continued pursuit of scientific endeavors. As the experimental apparatuses in the field of AMO physics continue to scale and become increasingly complex, we must change the way that we think about how to operate such a lab.

I would have never successfully transitioned the Fermi1 lab to the labscript-suite without frequent discussions with Carter Turnbaugh, Matthew Peters, and Carsten Robens, as well as the generous and wonderful folks active on the labscript-suite Google mailing list. Much of this work was also heavily inspired by the work of Zak Vendeiro [123].

For newcomers to the Fermi1 experiment wanting to learn how the experiment operates, I highly recommend engaging with the codebase supporting the tests and experimental scripts

[1] which also frequently required some debugging

[2] basically patches for sophisticated functionality, such as nonlinearity compensation, that was not natively available in Cicero and nobody in our lab wanted to implement in C#.

[3] I have attempted to write in first-person rather than using the royal "we" when this is the case.

that are executed on a regular basis. This experience is as close as one can get to building a new experiment from scratch, without actually doing so. While there are certain aspects of operating the experiment that are not computer-controlled, e.g., manual reconfiguration or alignment of optics, maintenance of water cooling systems, etc., a large fraction is, and understanding it will be invaluable for maintenance and understanding what upgrades and experiments are possible with the existing apparatus.

In the best case, the code is well-documented, readable, and has a sensible structure, and it can serve as reference material to learn how all the moving parts of the experiment are connected and work together. In the worst case, it will have few to none of these qualities, but it will nonetheless contain the status quo functionality of the experiment, even if certain components, such as tests, are missing. It is most likely that the state of the code will be somewhere in between the former and the latter. Regardless, restructuring, documenting, and writing tests, even if they do not immediately introduce new scientific capabilities to the experiment, is much more engaging than simply reading through what exists and moreover is an excellent pedagogical opportunity to get to know the machine better and should be embraced.

6.1 The role of software development in experimental physics

The development of new software in the modern physics laboratory is a ubiquitous task, by the very experimental nature of the work. Even if one wanted to, gone are the days where one produces ultracold atomic gases by hand[4]. And judicious and targeted automation of standard tasks result in less guesswork in the future about what was done and what exactly was recorded, and it can allow for a more productive and directed use of both mental capacity and manpower[5]. Rather than simply being a chore that one must take on to do experiments as a prerequisite, my belief is that there are many parallels between the successful operation of a physics experiment and the practice of software development, even if the two tasks have dramatically different end goals. Furthermore, there are a great deal of tools and principles that we can borrow or be inspired by for improving how we run the lab.

Both software engineers and experimental physicists are tasked with technically complex endeavors requiring many intertwined parts working together. To achieve success, executing the correct logical steps is but only one stepping stone. Other challenges to be surmounted include storing the logic in an understandable way, clearly defining when maintenance, deprecation, or upgrades are needed, and dealing with the scaling of complexity when more components or dependencies are introduced. This knowledge needs to be also shared and communicated within the team operating the lab, and sometimes this can even be intergenerational, between colleagues that have never met each other. How we can effectively tackle these challenges are central to the discussion in this chapter.

[4]The tale has it that Professor Wolfgang Ketterle manually dialed in the frequency sweep, precisely timed with the experiment, during the first trials of rf evaporation.

[5]I quote a former professor of mine, "If I can use these cycles [pointing to laptop], then I can save these cycles [points to head] for something better."

6.2 Why choose labscript?

P. Starkey and others from Kris Helmerson's group are the original pioneers of the labscript-suite. Starkey's thesis, which describes the architecture and functionalities of labscript [124], has a thorough discussion of the generic software and hardware requirements for a typical AMO experimental apparatus. Chapter 2 of [124] also contains comparisons with existing systems, including Cicero Word Generator. Therefore, we refer the interested reader there, and only discuss additional details, some specific to Fermi1, here.

6.2.1 Some opinions about Python

Python is a general-purpose programming language that suits the nature of work in AMO laboratories quite well. It has a wide user base, packages for both data analysis and interfacing to instrumentation, and a structure that suits both simple one-off scripts and small to medium scale software projects (in both lines of code and number of developers typical of an AMO experiment). Despite its lackluster performance compared to some compiled languages, the tenet that "researcher time is more valuable than computation time" dictates that time spent rewriting code to be efficient (in a language with more overhead) during the constant evolution of the experiment is often not worthwhile.

Many modern introductory undergraduate programming courses are taught in Python, and even those unfamiliar with the language can usually guess and modify the functionality of Python code due to its mostly simple syntax and structures. The non-existence of licensing or subscription fees further lowers the barrier to entry, and it ensures that former team members can still re-run old analyses, if they so choose. All of these features make it an attractive choice, and it is fairly reasonable to expect on-boarding members of the group to either already be familiar or to familiarize themselves with Python.

One alternative language to consider is C#; Aviv Keshet used this to build Cicero and Atticus [125]. Going down this route would most likely have involved modifying the existing capabilities of the Cicero paradigm, similar to the work done in Will Lunden's thesis [126] and also BEC4 in Wolfgang Ketterle's group. This option was much less attractive to us due to the sparsity of C# expertise within the Zwierlein group and the greater overhead to both debug and "get things going" (e.g., recompiling solutions).

Furthermore, one of the great strengths of C# is that it comes from its extensive tools for building Windows GUIs. Having GUIs readily available is a fantastic choice for doing simple tasks. However, the tendency in our experiments to continually add more features to what exists usually results in an bloated interface where form and function can become tightly intertwined. For a simple experiment, such tight coupling can be an asset for quick debugging, as visual cues can allow the experimentalist to find errors efficiently. As the experiment scales, however, a text-based approach to defining experimental logic makes modularization, documentation, and scaling more feasible. Coupled with visualization tools, this approach can be equally or more effective than being forced to interact with the experiment only graphically.

These considerations prompted us to look for existing Python-based software solutions for upgrading our control stack. During the exploratory phase of this work, Xinyu Luo from the Munich NaK experiment generously shared with us their Python-based suite, maintained

by Christian Gross and Sebastian Blatt. But the open-source nature of the labscript-suite and the large and active community supporting it, as well as the dedicated work of the original developers to maintain the project, were a few of the factors that eventually swayed us towards labscript.

6.2.2 Software requirements

Modularization

The Fermi1 apparatus was designed to be a general purpose machine. This enabled a diverse range of experiments in the Fermi1 lab, including studies done on Feshbach and ground state molecules, Bose polarons, and thermal Bose-Fermi mixtures, each representing a new capability of our apparatus. The need to maintain this ever growing set of functionalities is motivated both by the scientific philosophy that we should be able to reproduce previous work and, on the practical side, the desire to innovate on top of old work when a new opportunity presents itself. Taking inspiration from software engineering, maintenance (and growth) becomes much more manageable when frequently used ideas/themes/functionalities are identified, modularized, and reused.

As an example, I will discuss a common thread among many of these experiments, the process to load and prepare the atomic mixture at ~ 100 nK. We regularly re-optimize this process, whether this is because we perform some hardware upgrades, find and fix a bug, re-tune some parameters due to some drifts in the lab, etc. This is done with the goal of reliably producing of samples of the atom number and temperatures desired. In the Cicero paradigm, there are two routes to reproducing previous works, which may have implemented the atomic mixture loading with slightly different parameters and logic appropriate for the state of the lab at that time.

1. Copy the archived .seq file, identify all the differences between the current loading procedure and the archived one, make the modifications as needed, and run. This process was done almost entirely manually and can involve comparing $\sim 20-30$ words, each possibly having $\sim 20-30$ digital and analog waveforms and GPIB/RS232 outputs. This process would have been improved with either automated tools to find differences[6] or a version control tracking system[7]. Due to the manual nature of the process, there were often inconsistencies as old files were updated that then made it difficult to establish a "single source of truth."

2. Maintain one monolithic .seq file with as many "seqModes" as functionalities of the experiment. The idea of "seqModes" is precisely that of modularizing the experiment's functionalities. In practice, a monolithic .seq file might consist of hundreds of "words" that are active or not, depending on which of the few dozen seqModes is selected, and a parameter list that scales proportionally as well. Both of these can be overwhelming to the experimentalist trying to understand what the .seq file is programmed to do, clean up the parameter list, etc.

[6] I implemented a basic prototype [127].

[7] We attempted to do this by tabulating screenshots of the relevant "word" in the Cicero .seq GUI along with its filepath, a tedious process that never caught on.

Neither of these solutions are satisfactory and stem from the constraints of Cicero.

With the script-based approach made possible by labscript, we can add a layer of *abstraction* by creating a module that we then import and call. I include as an example, at the risk of exhaustively explaining a rather simple programming concept, a fictitious example script (let us call it `exampleExperiment.py` here) for doing science.

```
# contents of exampleExperiment.py
# (a script that can be sent to runmanager to be compiled and executed)

from fermi1_apparatus.testSequences.utility_functions import na_load_mot

# set up ConnectionTable() ...
start()
t = 0
t = na_load_mot(t=t, ...)
# finish atom loading and do science ...
```

We then have a separate file, `utility_functions.py`, where the instructions of how the Na MOT is loaded are stored, e.g., the timing and settings of various AOM drivers.

This separation becomes incredibly useful when the *implementation* of the imported functions (e.g., `na_load_mot`) changes. This could be something mundane, e.g., re-optimizing certain laser powers, or it might be something more major, e.g., swapping out an analog AOM driver for a digital one. And the beauty of storing the detailed implementation into a separate module is that updating the atom loading for all scripts (e.g., `exampleExperiment.py`, `exampleExperiment1.py`, etc.) that import this function to the most recent version happens *automatically*! That is we do not have to go through every single file manually to update the implementation, as would be the case for separate Cicero .seq files.

At the moment, the primary trade-off in adding this layer of abstraction is that the current version of labscript does not save the imported code in the permanently stored .h5 shot files, only saving the script .py file itself. An example of when this might be detrimental is that hard-coded parameters in imported code are not stored permanently. This is partially mitigated by labscript's ability to save which snapshot of active repositories are being used to generate the low-level instructions[8]. It is certainly also possible to modify the labscript source code or the way we write scripts (e.g., through an appropriate use of Python decorators) to save imported code as well, however.

Scoping

An atomic physics experiment has many parameters that need to be tuned and set correctly to function. This naturally ties to the concept of variables in programming, and we will discuss some of the flaws of its implementation in Cicero, as well as some solutions (and new flaws) that are present in labscript.

One of the serious flaws in the storage of parameters in Cicero is that parameters and logic/timing are stored altogether in one file of the proprietary .seq format. This locked the

[8]But this is not actively used in Fermi1 at the time of writing, and would require an extremely frequent cadence of git commits.

experimentalist into interacting with the parameters only through the limited GUI interface, which did not obviously support basic functionality such as automatic sorting of variables by name, datatype, or user-defined categories. This meant that typically as new ideas were tried, the variable list monotonically grew into an unmanaged forest, as the pruning of variables tied to some part of the experimental logic, or worse to other variables, often led to cryptic error messages indicating that the variable contained some crucial part of the logic for compilation[9]. The global nature of these variables meant that they could be used anywhere (for instance, a variable `rfFreq1` could be presumably used in either rf evaporation, spin preparation, state shelving, or spectroscopy), and unless there was a pre-established naming convention to indicate its scope of functionality[10], untangling the variables list essentially boiled down to intuition and guesswork.

With the labscript approach, some of these woes are addressed. Parameters can be stored in "globals" .h5 files, and at compile time, runmanager will inject the parameters from the loaded globals file as variables into the global Python namespace. It is fairly easy to trace how global variables are tied into the experimental logic, by simply searching through the text of a script or its imported modules. Runmanager provides also the ability to organize the storage of parameters in groups within the globals .h5 file.

There are a few areas for future improvement using this approach. The global nature of these variables means that any experimentalist interacting with the code must take care not to introduce confusion. For instance, modifying its value halfway through a script would certainly be disastrous for record-keeping. To deal with this problem in Fermi1, we signify global variables by denoting them stylistically in snake-case `ALL_CAPS` so that we do not mistakenly overwrite them. (Perhaps this could be made explicit by injecting parameters with Python's `enum` class instead, but this would require modification of runmanger and introduce awkward syntax required to write new scripts, breaking backward compatibility.)

A second issue of concern is that global files, being of the .h5 format, result in `git diff` outputs that are not human-friendly when attempting to do version control. Because of this, I have generally been of the preference of minimizing the use of globals, instead storing parameters once optimized as human-readable default keyword arguments in their corresponding function, only binding them to global variables when re-optimizing or testing new functionality, and updating the default argument value when necessary. However, my suggested approach is inflexible in the sense that it assumes that our experiment has only one default setting, and furthermore it is not the established standard in Fermi1. Carter Turnbaugh (in Fermi2) takes an alternate approach in their custom fork of runmanger, where they instead store parameters also in .py format, which is extremely flexible at the cost of sacrificing the pre-existing structure built for .h5 files.

Readability and documentation

It is my belief that a key component of good scientific practice is the recording of not only the experiments carried out and how the data was interpreted and analyzed, but also the how and why of the implementation. The latter can be instrumental for future researchers in understanding what details of the experiment were crucial. Certainly, this is recorded in

[9] Frustratingly enough, the message seldom told us which part, though.

[10] There was no such convention in Fermi1.

lab books and PhD theses, but in the words of my colleague Eric Wolf, we should strive to document "as close to metal" as possible to make the jobs of our future selves and those who inherit the lab easier. With physical setups, we can certainly leave notes taped to the insides of electronics boxes or on optics breadboards. Attempts to do the analogue in a Cicero .seq file are surprisingly difficult, since there is only a single comments/notes box tucked squarely out of sight in the interface.

With a text-based approach, there are advantages at a few different levels. Starting from the lowest, it is easy to add *inline comments* next to lines that deserve some extra attention. By separating logically distinct capabilities of the apparatus into *functions*, we can expose the relevant experimental knobs as *input arguments*, and for sophisticated functions longer than a few lines, describe both the purpose of the function and the expectations for inputs in the function docstring. Finally, at the module level, docstrings can be added as headers to every .py file and readme's to every folder. Even the organization of the project files and folder structure can communicate relevant information. A myriad of tools for automatically generating "browse-able" (e.g., .html) documentation from properly formatted docstrings exist, and it is my belief that a constantly updated set of documentation is an invaluable asset to complement the more traditional media of the lab book and theses.

Whether the smorgasbord of thousands of cells in a Cicero .seq file or thousands of lines of text that support a labscript .py script alongside visual output from *runviewer* is more readable is in the eye of the beholder. One of the key features (and problems) with Cicero is that the experimentalist is shown precisely what is happening at every "word" of the sequence, and modifies the experiment through that same interface. This prevents the communication of what components are crucial to a particular Cicero "word", which components are simply holding their previous state, and which are being pre-triggered[11]. Cicero realizes some features with readability in mind, for example "sequenceModes", "timestep groups", "pulses", etc., but further changes would likely involve major changes to the GUI. As with many other text-based programming languages, Python allows the experimentalist to add layers of *abstraction* in the form of interconnected modules, functions, and classes, such that one can easily see the bird's eye view of an experimental sequence and zoom into the concrete implementation as necessary.

Version control

Having a tool for version control can be immensely useful in our laboratory for various reasons, and the binary format of .seq files along with the graphical-only interface of Cicero made it quite difficult to establish any standard workflow in this vein. In Fermi1, we adopted the industry-standard tools of git and GitHub, and so in this chapter we will use their associated vernacular. Continuing from our discussion about documentation, the existence of a *commit history* and *pull requests* with the regular use of these tools can help the experimentalist understand why the experiment is set up in its current configuration. For example, one can see the dates of when a file was edited, how/whether changes were tested and easily find corresponding notes in the lab book or the author of the code. This history is also useful for tracking and recording justification for features that are deprecated.

[11] In the text-based paradigm, each line of code is a command that signifies a deliberate change being made, which can help with interpret-ability.

The ability to easily test new changes on independent *branches* and check for *merge conflicts* empowers the experimentalist to prototype quickly. This could be implementing a bug-fix, replacing/upgrading hardware, or simply trying a new way of doing things.

Recommendations for how to use git and GitHub in the lab workflow is discussed in a later section.

Test-ability

It is certainly easy to tell when the experiment is broken. For example, the atoms or molecules do not show up the way you expect them to or their loading is inconsistent. But identifying which prerequisite component is broken is certainly not! The ever evolving requirements of the experiments we would like to perform inevitably comes with changes that are capable of breaking some of the many existing functionalities of the experiment. All of the existing parts that make the apparatus work have finite lifetimes as well. Having a list of such prerequisites that one knows the dependency structure of and can test as independently as possible is an invaluable tool when debugging. Moreover, it is critical that one discovers the broken component quickly, before a second one breaks and further complicates the debugging process.

Efficiently and painlessly keeping the machine running can be achieved by maintaining a standard set of test files. In the Cicero approach, this amounts to a whole new set of functionalities of the apparatus, which as discussed in section 6.2.2 requires a great deal of effort that is hard to motivate, until the machine is broken. Therefore, testing was usually done "on-the-fly", by modifying an existing and recently working .seq file. A drawback of this approach is that when the machine is broken, it can be unclear if the test one created does not yield the expected result because that functionality of the machine is broken, or if the test created does not actually carry out the intention as desired (i.e., programmer's fault).

The ability to modularize and abstract allowed us to create such a suite of tests, which largely build off the same set of base code[12]. The intention of these tests are to enumerate the known and testable functionalities of the experiment. They will hopefully also serve as a pedagogical resource for on-boarding new members of the lab, since these scripts are typically much simpler than a full-fledged experiment script for doing science.

Synchronized storage of experimental logic, acquired data, and analysis

An automated record of experimental parameters and data facilitates on-the-fly visualization and is a stepping stone to enable closed loop optimization. Cicero on its own keeps a record of what was executed on the apparatus through run logs, but the synchronization of this information with acquired data and corresponding analysis must be done separately. There are several bespoke solutions integrating with Cicero for this in the MIT CUA. Our solution in Fermi1 before migrating to labscript was built on *breadboard*, a package written by Biswaroop to run a Google Cloud SQL database for storing the run logs and subsequent data. My understanding is that the architecture there was never meant to support "live" plotting of data, as the synchronization was done indirectly by matching timestamps of data

[12] Admittedly, I do think we need to establish a regular procedure for maintaining them.

acquired independently, rather than through an explicit architecture (e.g., each shot requests certain data after execution). Therefore, reading/writing a row from the database could take up to $5-10$ seconds, and this meant that "off-by-one" errors had to be handled carefully and sometimes data would be taken but not matched to an experiment. Additionally, as we tried to bring more *breadboard* clients online (e.g., to store image filepaths, wavemeter readings, scope traces, "live" analysis, etc. each with its own responsible client), we found that the architecture was not robust to clients overriding each others requests and data would then be sometimes missing.

The labscript developers explicitly coordinate the storage of each of these components through the generation of a .h5 *shot file* that is appended to by the various components of labscript as a shot is compiled, executed, and analyzed. Briefly summarizing the architecture described in detail in [124], *runmanager* stores the .py script used to compile machine instructions and experimental parameters as specified in the loaded *globals* .h5 file, *BLACS workers* can collect data at the beginning or end of a shot's execution (using `transition_to_buffered(...)` or `transition_to_manual(...)`), and *lyse* runs single-shot analysis scripts that run at the individual shot level (e.g., how many atoms were in this particular repetition).

Porting from Cicero

Philosophically, it would have been ideal to migrate the lab from the Cicero framework to the labscript-suite, starting from a detailed, first-principles understanding of the experiment[13]. However, my lack of such a complete understanding was part of what had motivated us to pursue this migration in the first place. As discussed previously, the functionality of the experiment was previously stored in a collection .seq files, each with $\sim 10^3$ cells, and often it was unclear from first principles why various "words" were configured in their given state, the meaning of certain parameters in the "Variables" tab (especially "dummy"-variables), etc. As such, a manual translation of .seq files into .py scripts sometimes turned into blindly copying the behavior of various black-boxes, and this was quite often error prone due to a lack of understanding and the sheer volume of translation required.

To circumvent the tedious debugging of manually translated .seq files, we instead built a small program to export the relevant portions of binary .seq files into a human-readable format. We did this within the Cicero framework, and it generated .yaml files that could then be read, searched, and parsed with any tools desired [128]. We auto-generated about 95% of labscript .py scripts (and therefore eliminated about 95% of errors due to my finite human abilities), and from there it was possible to bring the machine online running labscript. We then manually aggregated, compared, reconciled, and grouped common parts of scripts into various importable modules.

6.3 Hardware requirements

There were few hardware changes required for migrating the Fermi1 software stack to labscript, and they did not pose a major hurdle. The first was to replace the existing pseudoclock

[13] Hats off to Carter Turnbaugh in the Fermi2 lab who did indeed make it work that way!

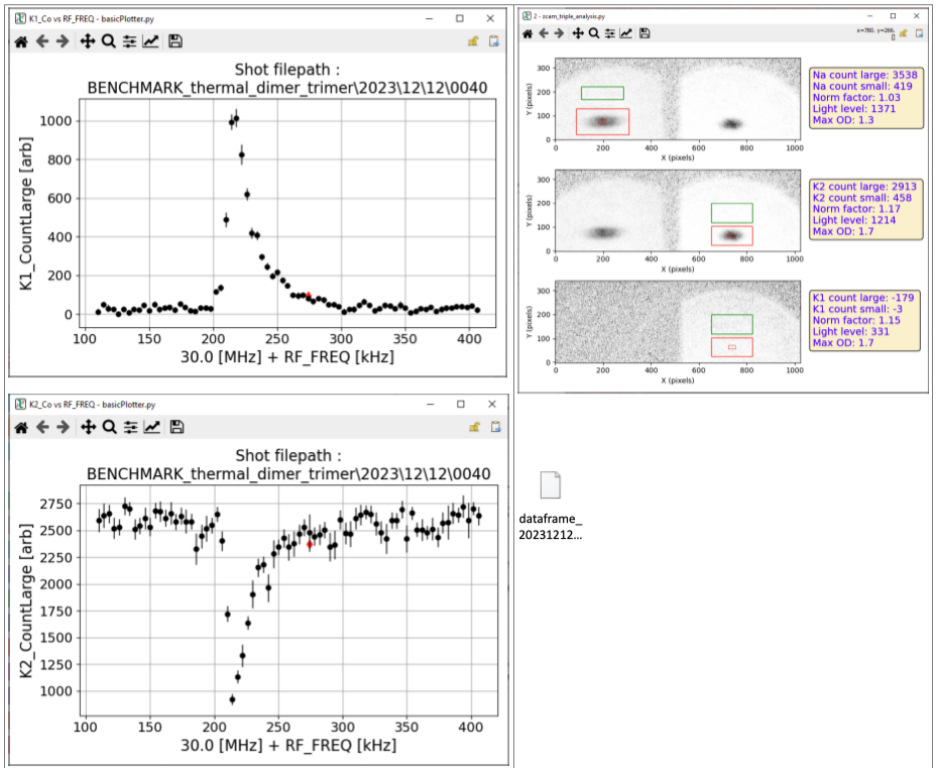

Figure 6.1: A screenshot demonstrating standard storage of plots, representative images, and the attached dataframe .pkl/.zip file in the lab OneNote.

with an inexpensive, labscript-supported Prawnblaster (a Raspberry Pi Pico based solution), for which Carter Turnbaugh has developed a PCB for as well. The latter was to implement software-timing for certain devices that cannot be preloaded with a buffer and need to be re-programmed within a shot, a functionality that is not natively supported by labscript. There are several workarounds for this discussed in the active Google group for labscript, so we will not elaborate here about its implementation.

6.4 Some general workflow guidelines

Here I will leave some suggestions on how labscript tools, git and GitHub can be integrated into the process of keeping the lab book, as well as making major changes to the lab/codebase. This is written partially in an aspirational manner, but we also include examples of where this is done.

Storage of data and plots in the lab book

As we show in figure 6.1, we follow this checklist when adding a plot to the lab book. The motivation here is to make it as easy as possible to reproduce and analyze these plots in further detail when the need arises.

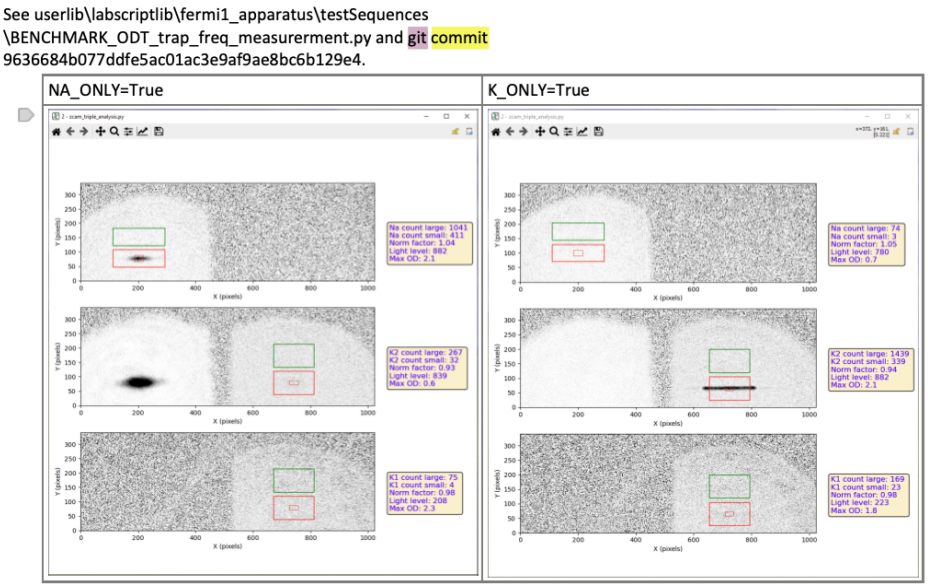

Figure 6.2: A screenshot from the lab notebook with images linked to a git commit by its hash.

- Take data by specifying a global parameter in runmanager. Remember to store the units!
- Paste in screenshots of plots. We have built functionality in `analysislib/basicPlotter.py` to use the stored unit and format the axes and units to be maximally readable (for instance, as shown in figure 6.1, data taken over 30.1 to 30.4 MHz is not shown as $(3.01 - 3.04) \times 10^7$ Hz, but rather 30 MHz + 100–400 kHz). Secondarily, the titles of plots also points to where their data is stored.
- Take a screenshot of visualizations, such as absorption images. This serves also as a sanity check. In such visualizations, we have built indicators to immediately alert us to simple mistakes, such as counting atoms with optical densities beyond what we can measure, indicated by bright red pixels.
- Attach the dataframe .pkl file exported from runmanager. This can later be downloaded and re-analyzed.

Git and GitHub

Git commits are an excellent way to communicate and record what changes have been made to code, therefore, we strive to make regular commits on a daily cadence[14]. However, git is primarily a text-based tool, and commit messages are almost never descriptive enough to show what we have accomplished in the lab. Therefore, to add additional documenting plots for example, we annotate the plot stored in the lab notebook with the corresponding git hash,

[14]I will emphasize that each logical unit of change deserves its own commit, and not to simply mass commit at the end of day, which partially defeats the purpose of version control.

as shown in figure 6.2. Future readers of the lab book wishing to understand how certain changes were implemented can then easily find the commit via the command `git show`, or alternatively those browsing the git commit history will have a supplementary record readily available in the lab book.

Our day-to-day operation using involves committing to the `main` branch, but for major changes, such as the introduction of a new hardware device or the reconfiguration of a laser table, the recommendation is to make a branch where changes under testing is clearly delineated. The additional process of then creating and merging a pull request is an opportunity to ask a colleague to review and catch possible bugs. Some relevant questions to ask are below[15].

- Is there a readme for example usage? Do complex functions with multiple input arguments have a clear docstring summarizing functionality and describing the expected inputs and outputs?
- Is your colleague able to understand what the code is doing, without you explaining?
- How can we verify that this code is working? (e.g., is there a plot it produces? Does it command a device that I can test on an oscilloscope?)
- Does it break other functionalities of the experiment? Are there any standard test scripts to run for checking this? Do any tests need updating?
- Is there any part of the implementation that is unconventional? Is this documented?

Answering these questions helps the experiment to continue running smoothly and gives all members of the team a chance to learn about the changes made, ensuring that there is no single point of failure due to the knowledge being internal only to the team member implementing the change.

6.5 Future recommendations

6.5.1 Advantages of a distributed architecture for control signal delivery

The architecture for delivering analog and digital control signals for the Fermi1 apparatus is highly centralized and is built around the Atticus constraint that all National Instruments (NI) cards are jointly synchronized by one pseudoclock-line. This, along with a proposed alternative, is shown in figure 6.3 and has not been changed significantly with the migration to labscript. One advantage of this architecture, compared to the alternative, is its conceptual simplicity and the initial cost-savings, requiring only one computer and a single set of NI hardware. It suffers several flaws, however, which can be mitigated.

The control signals begin as digital information, generated by a computer, and are ultimately translated and delivered to devices at each optical table through the analog channels

[15] Some of these questions certainly can apply to non-software projects as well!

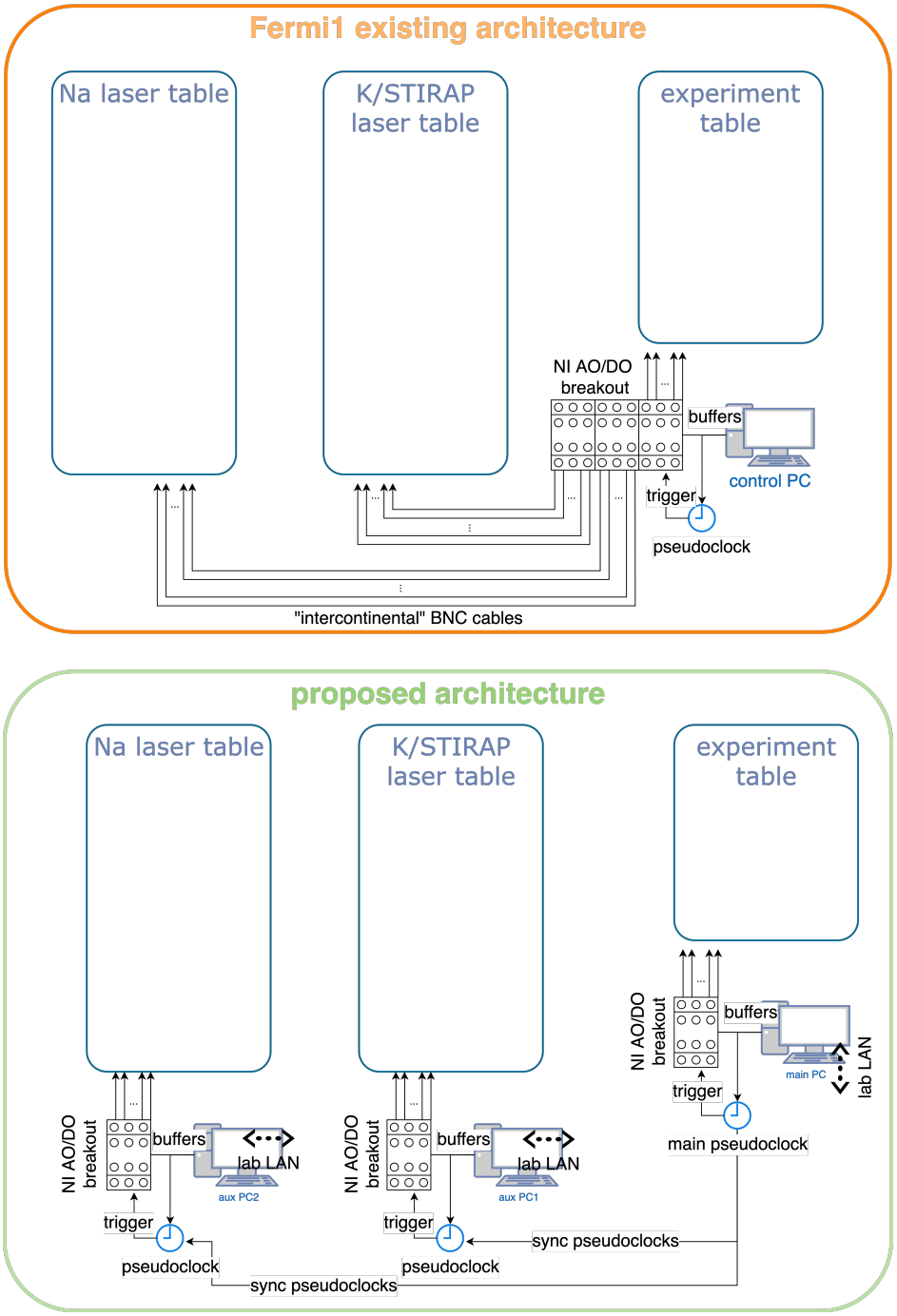

Figure 6.3: A diagram of architectures for delivering analog and digital control signals across the laboratory.

of BNC cables, whether the signal is digital or analog in nature. Since this information being sent along BNC cables is not protected by any kind of classical error correction that is possible with digital channels, signal integrity must be protected by ensuring that the physical length of the cables is as short as possible and does not pass through unnecessary components (e.g. BNC T-connectors, noisy amplifiers, etc.). Practically speaking, this can decrease the probability of errors (e.g., missed triggers) of an experimental shot failing to execute properly.

Since labscript supports distributed buffering of NI cards across computers on the same local area network and sharing a common network drive, it is possible to eliminate large portions of the "intercontinental" BNC cables (as we affectionately termed) physically spanning across the lab to bridge the gaps between optical tables and the centralized control hardware. By placing a computer connected to the LAN and set of NI hardware at each physical module of the lab (e.g., near each laser table), the relevant control signals can be protected in a digital medium for as long as possible. In its implementation, one can view this as replacing the "intercontinental" portion of the BNC cables with single ethernet cables, which additionally makes the lab infrastructure easier to maintain.

In the compilation of low-level instructions, the single pseudoclock-line limitation of Atticus presents many inefficiencies. As an example, we consider the ODT evaporation stage of the experiment, where the only components that need to be updated are those controlling the optical powers of the ODT delivered to the atoms. However, since every output channel is being triggered by the shared pseudoclock to output an updated value, they each have to be buffered with their static values over the entire duration of the evaporation as well. For sufficiently long processes such as evaporation, this can actually have a significant impact on the time and space required to compile a shot, and again, forcing conceptually unnecessary updates increases the probability of botched execution.

Labscript has no such limitation with its support of multiple pseudoclock-lines and can thus be much more efficient. Furthermore, the physical layout of the proposed architecture encourages one to control devices from the same module from outputs sharing the same pseudoclock-line. Thus, in this scheme, one will naturally connect devices and pseudoclock-lines in such a way to ensure efficient compilations.

6.5.2 Taking advantage of the *runmanager* API

One great advantage of adopting the labscript framework is the existence of a *runmanager* API that allows generation and execution of shots by not only a human through the graphical interface, but also with programmable logic as specified in a Python script. Two areas where this can greatly improve productivity include the automation of routine benchmarking and closed-loop optimization when certain benchmarks are not met.

A typical day in the lab begins with a seemingly simple start-up routine, including the measurement of various laser powers and the execution and inspection of benchmarking shots, e.g. whether a Na BEC of a specific size can be loaded with a pre-specified script. However, as the experimental apparatus becomes more sophisticated, the number of such measurements in the routine scales accordingly, leaving less and less time in the workday available for exploring new scientific goals. This actively disincentivizes adherence to a thorough and regular start-up routine, especially since many of these tasks are tedious, requiring manual

data entry, inspections, etc., but such a routine is extremely beneficial for identifying and rectifying weak points in the lab. Creating such a script that calls the runmanager API to run a standard set of benchmarks can clearly define the start-up routine[16] and encourage the automation of the most tedious steps.

M-LOOP is a machine-learning interface that has been integrated with labscript through the *lyse* and *runmanager* APIs. It has been used with success to optimize atomic physics experiments, such as accelerating the production of BECs [129], with minimal human intervention. Such optimization routines are not explicitly limited by human intuition, patience, or biases and can even help rediscover ideas that turn out to be beneficial in a particular setup[17]. Some potential applications of this in Fermi1 would include (but are certainly not limited to) finding a more robust routine to prepare atomic samples, choosing laser pulse parameters and servo loop settings for STIRAP, and in the future perhaps even finding the optimal parameters for microwave shielding and evaporation of ground-state molecules.

[16] One might also consider automated logging to a centralized database that can be visualized with live dashboard tools such as Grafana.

[17] For instance, in Professor Vuletic's group, M-LOOP unintentionally implemented grey molasses cooling.

Chapter 7

Outlook

In this chapter, we discuss several proposed follow-up experiments on the work presented in Chapters 4, 5. We also briefly review ongoing technical upgrades within the near future and the variety of new techniques investigated in other ultracold molecule experiments around the world.

7.1 Experimental proposals with parallels to quantum optics

7.1.1 Quantum interference in loss pathways

Losses can strongly alter the dynamics of a quantum system. For example, a suppression of molecule losses in an optical lattice via the quantum Zeno effect has been observed experimentally [130]. In our system, we can rf-associate dimers and trimers that both undergo three-body loss due to relaxation, as shown in figure 7.1. We speculate that (an idealized system with two Na atoms and one K atom, all at zero temperature) they are both ejected from the trap into the same continuum, where we have a deeply bound NaK molecule and Na atom recoiling and escaping the trap. Under this assumption, we can ask, is there a rf resonance condition where losses are completely suppressed due to quantum interference? There are two paths, with intermediate states involving the creation of a dimer or a trimer, and is it possible that these amplitudes interfere and cancel when the rf frequency is tuned in between the two loss resonances to give the amplitudes opposite sign? This is in analogy to the concept of electromagnetically-induced transparency (EIT), where photon scattering can be suppressed due to a similar interference mechanism.

It remains to be explored how technically feasible such an experiment to see such a transparency window would be, for instance, the requirements on coherence times, temperatures, technical heating rates, and preparation of a highly imbalanced and dilute sample.

7.1.2 An analogy to vacuum Rabi oscillations

In Chapter 5, we described the energy scales we observed as due to the BEC acting as a coherent reservoir of particles dressing and forming superpositions of dimers and trimers

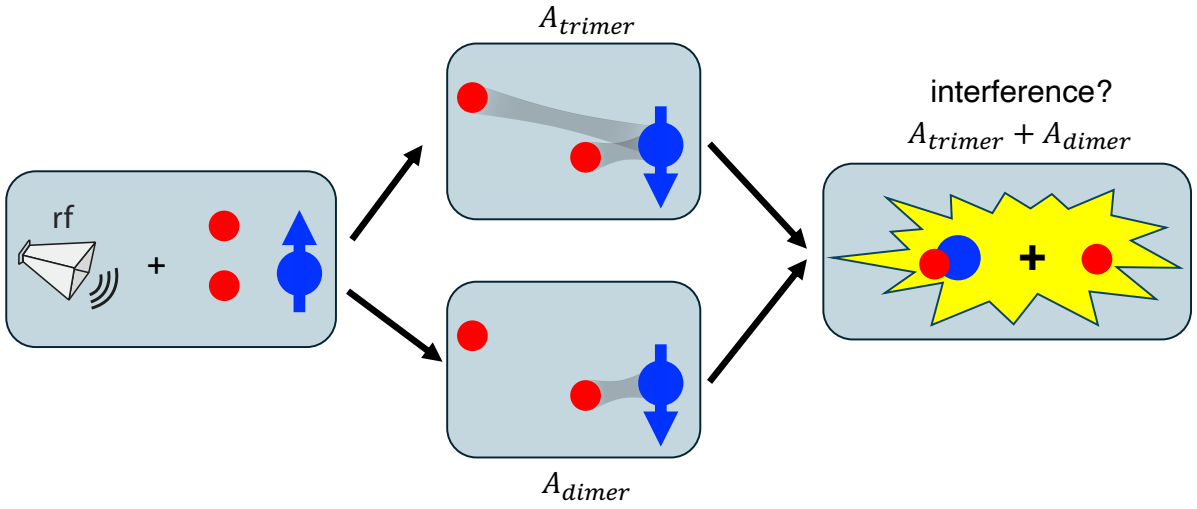

Figure 7.1: A quantum two-slit interference experiment where the slits are defined by molecular bound states with different binding energy and number of atoms.

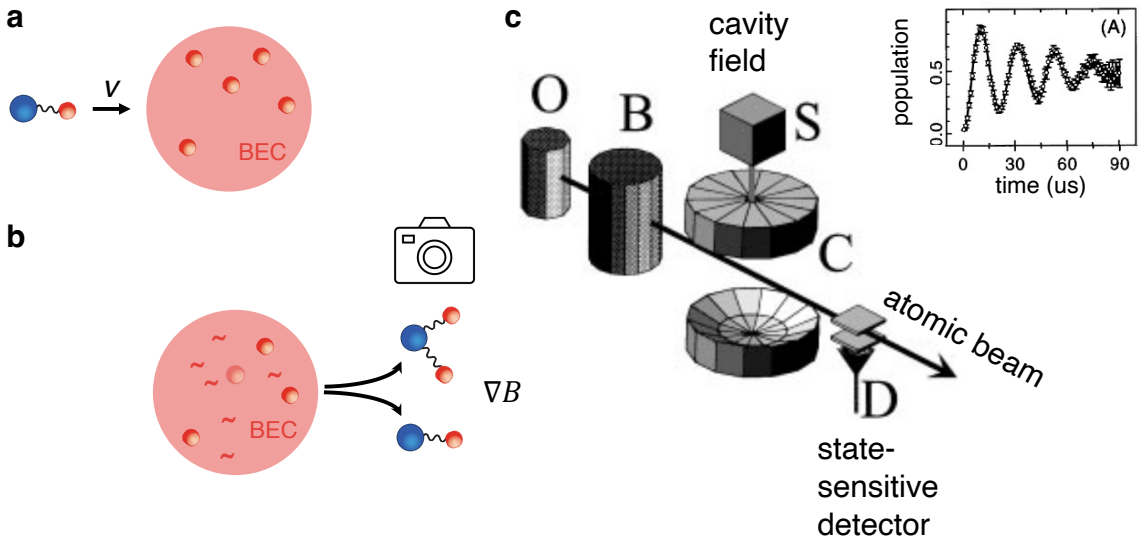

Figure 7.2: We propose an analogue (a, b) to vacuum Rabi oscillations (c) with halo dimers and trimers interacting with a BEC. (a) A dimer is prepared and launched with velocity v through a BEC, a coherent reservoir of particles. (b) After interaction within the BEC, where the eigenstates are conceptually dressed dimer-trimer superpositions, we speculate that the initial dimer state may undergo oscillations and emerge as a dimer or trimer, depending on the interaction time. State-selective detection may be performed with the presence of a magnetic field gradient, ∇B. (c) Sketch of an experimental apparatus to measure Rabi oscillations of Rydberg atoms interacting with a coherent electromagnetic field. Adapted from [131].

exhibiting level repulsion. Furthermore, since the energy difference due to level repulsion is much greater than the inverse lifetime of these superposition states, we can test the coherent nature of these superpositions by probing for oscillatory phenomena. Here we propose an experiment analogous to the cavity QED experiment from Serge Haroche's group [131]. In the cavity experiment, Rydberg atoms of with principal quantum number $n = 51$ are launched through a cavity and undergo Rabi oscillations to and from the $n = 50$ state, due to strong coupling to a coherently populated cavity electromagnetic field. Equivalently, these oscillations can be described as a beating between the dressed atomic-cavity states, split apart in energy by the Rabi frequency, where the excitation is exchanged between the atom and the cavity. Their total interaction time with the EM-field is determined by their velocity and the cavity mode-volume, and upon exiting, they are detected in a state-sensitive manner. In analogy, we propose to launch a Feshbach dimer into a BEC, where we can test if the eigenstates are dressed superposition states. Here, we might investigate if they undergo oscillatory dynamics, as in the case of cavity QED, or if the continuous nature of a BEC's excitation spectrum, e.g., phonons at low frequency, causes dephasing, prevents us from observing coherent oscillations, as suggested by the continuous nature of the spectra we measured. Another interesting avenue to explore is to see if Landau's superfluid criterion (i.e., a particle moving through a BEC below the speed of sound not being able to shed phonons) plays a role in this problem.

7.2 Towards a degenerate gas of dipolar molecules in Fermi1

Several technical advances well within reach can power the next generation of experiments done in Fermi1, by enabling the production of larger and more degenerate samples of ground state molecules. Two such projects are already underway. First, we have already seen preliminary success in achieving higher Feshbach molecule conversion efficiencies (relative to the minority population, K) by switching from rf association to the adiabatic magnetic ramp technique[1]. The endpoint of the ramp can be set to create more deeply bound Feshbach molecules (several MHz as opposed to 10s of kHz), enhancing the Franck-Condon factor connecting the Feshbach and intermediate molecular states and allowing us to achieve stronger coupling for the same laser power [32]. Second, a second-generation STIRAP laser system will soon come online, and we have high hopes that this system can be more reliable in the everyday production of molecules. Finally, we remark that the production of larger and more degenerate Bose-Fermi atomic mixtures will almost certainly give us a better starting point for producing molecules, whether that is through improvements on laser cooling [132] or the mode matching between magnetic and optical traps [36]. Implementing more sophisticated laser cooling techniques such as gray molasses, especially in ^{40}K due to its poorly resolved excited state structure, could be potentially quite fruitful (for example, the JILA KRb experiment reported a factor of five increase in ^{40}K atoms trapped [132]). We stand to benefit from this, since we do not use an enriched source of ^{40}K, and our existing procedure for laser

[1]This has an additional benefit of protecting against the typical $\sim$ 10 mG long-term drifts that shift the rf association resonance by several kHz.

cooling K only consists of loading and compressing a bright MOT.

The future of ultracold dipolar molecules as a platform for quantum simulation is bright. For many years, lossy inelastic molecular collisions, even for molecules that are chemically stable, stood as a barrier to quantum degeneracy via evaporative cooling in such systems[2], and even now, it is unclear what the exact mechanism for this loss is[3]. Recent advances in shielding techniques with both DC [134], [135] and AC fields [136] have proven to be quite successful in mitigating these losses, and this has led to the success of evaporative cooling methods in both bosonic and fermionic systems [135], [137], [138] and even Bose-Einstein condensation of NaCs using the microwave double-shielding technique [139]. The fine-tuning of scattering processes via external fields such as atom-molecule and molecule-molecule Feshbach resonances [140], [141] and field-linked resonances [142] has also been experimentally demonstrated. In principle, many of these techniques can be straightforwardly applied to the Fermi1 experiment, and this promises the tantalizing prospect of realizing exotic phases of matter in our system.

[2]For instance, even in the dark, loss still occurs at the universal rate, where every colliding pair reaching short range is lost [32].

[3]For example, see [133] on NaK-NaK collisions in the presence of light.

Appendix A

Characterization of optical components

Since there are future plans to install a high-NA microscope objective outside of the vacuum chamber, the first optic of the imaging system will be the vacuum window. Here, we discuss how to characterize its thickness and surface profile to ensure that the custom-designed objective will harmoniously with the vacuum window.

We use a phase-shifting, white-light interferometer for this purpose[1]. The advantages and principles[2] of the phase shifting scheme are discussed in [143]. Using light of a short coherence length ensures that interference patterns between surfaces in the measurement setup can be recorded selectively, and allows us to precisely measure the thickness of an optic[3]. The implementation is contained in figures A.1 and A.2.

We report several measurements in the tables A.1, A.2. The measured wedge angle of the top bucket window is 3.4×10^{-3} degrees. The variations[4] of the surface profile over 1" diameter subregions of the bucket windows ranges from 1σ of 60 – 130 nm[5], and since the profiles consist largely of low-spatial frequency variations, we can realistically expect to compensate their aberrations, with either phase corrector plates or a spatial light modulator, if necessary. For possible future replication of this work, we have purchased a 3" diameter optical flat from Edmund Optics (part no. 43-428) to ease the alignment of the reference flat for characterizing a 1" diameter region.

[1] Thanks to Jinggang Xiang for introducing me to this method.

[2] In short, the idea is similar to that of a lock-in measurement.

[3] much like in optical coherence tomography (OCT)

[4] I believe this could even be an overestimate, due to uncharacterized imaging artifacts. I suspect the imperfect large waist "Gaussian" beam in the Fizeau interferometer, generated by launching a single-mode fiber into a single $f \approx 100$ mm spherical lens, or the demagnification imaging lens in front of the camera.

[5] depending on which region is measured

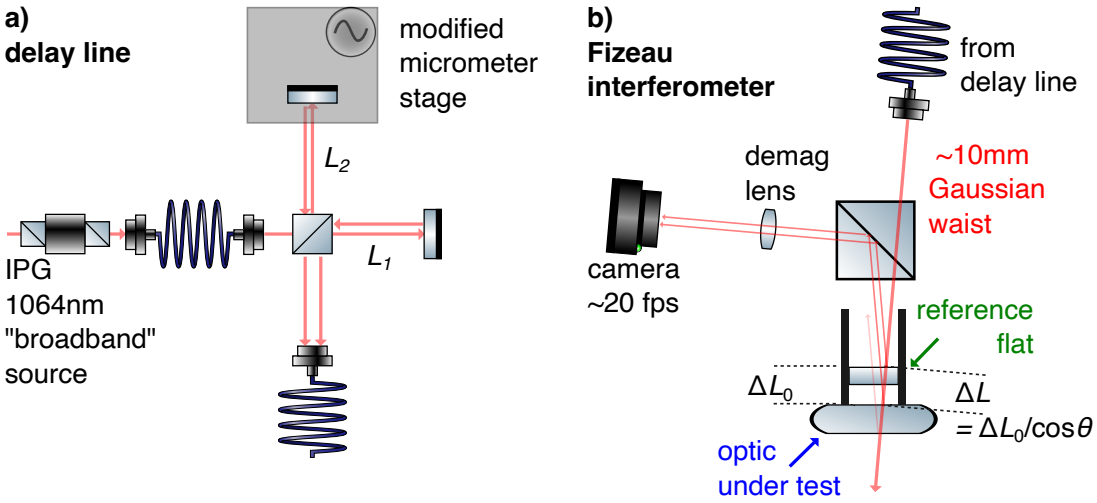

Figure A.1: (a) We generate "white" light with a superposition of terms that traverse different optical path lengths. We use a 1064 nm IPG source with 3 nm bandwidth to feed a Michelson interferometer. One arm can be manually lengthened with micrometer precision using the micrometer screw, and phase shifts can be driven at $\sim$ 0.5 Hz (chosen to be well below the framerate of the camera) using the inserted piezo stack. (b) We measure interference patterns between the reference flat (green) and optic under test (blue, top bucket vacuum window) in a Fizeau interferometer using a large $\sim$ 10 mm waist Gaussian beam. The rest of the vacuum chamber and bottom bucket window are not shown, for clarity. Contrast is maximized when the delay line matches the optical path length difference between surfaces in the Fizeau interferometer, $|L_2 - L_1| = |\Delta L|$. The reference flat is mounted in a lens tube and directly contacted to the optic under test to ensure mechanical stability between the interfering surfaces. For precise measurements of the thickness of the optic under test, $\cos\theta$ errors in both (a, b) must be accounted for.

	reflectivity at 1064 nm (%)
top bucket (atmosphere-side)	0.7
top bucket (vacuum-side)	0.5
bottom bucket (atmosphere-side)	0.5
bottom bucket (vacuum-side)	0.6

Table A.1: Inferred from fringe contrast measurements by assuming the reflectivity of the reference flat is that of UVFS, 6.6%.

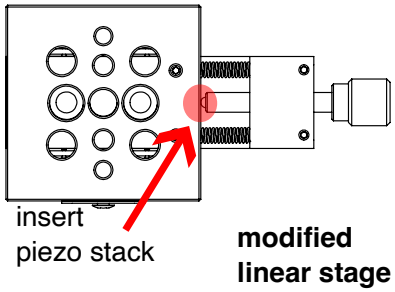

Figure A.2: We modify a linear translation stage for controlling the uniform translation of a mirror to ~ 10 nm precision. This is done by inserting a piezo stack between the spring-loaded contact point of the micrometer screw actuating the motion and the platform. We place the piezo stack within the stage, rather than gluing between the mirror and its mount, to minimize unwanted tilting of the mirror while actuating translations, due to possible off-center placement of the piezo. This sub-micron precision can also be achieved with Thorlabs stock parts, e.g., part no. NF15AP25. Drawing modified from the Thorlabs CAD file for part no. MS-1, Translation Stage with End-Mounted Adjuster Screw.

	physical thickness (mm)
bottom bucket	8.06 (assuming n)
top bucket	8.05 ± 0.0031 (assuming n)
between vacuum-side of top and bottom buckets	24.73

Table A.2: We measure optical path length difference by varying the length of the delay line. Index of refraction $n = 1.4496$ assumed for UV fused silica. Errors from $\cos\theta$ are calibrated by an independent measurement of the reference plate using calipers.

Appendix B

Development of a ∼kHz linewidth diode laser

External cavity diode lasers (ECDLs) are extremely common in AMO laboratories, as often they are a low-cost light source that can be narrowed to a small fraction of the typical atomic transition linewidth through a combination of passive and active feedback [144], [145]. The external cavity provides optical feedback by reflecting a fraction of the diode laser's output back into itself, which can narrow the laser if a suitable proportion is reflected and the cavity is sufficiently long. Typically ECDLs are constructed such that they operate in regime V as defined in [144]. The intuition for this phenomena is that a narrow linewidth laser has a long phase coherence time, and one can stimulate the laser to "remember" what its phase was earlier by using a cavity.

There are several common geometries for implementing an external cavity. This includes the Littrow and Littman-Metcalf configurations, which employ a grating simultaneously providing frequency selectivity and partial reflection, and the cat-eye, which employs a combination of a partially reflective mirror and an angle-sensitive interference filter for wavelength selection. The two main drawbacks of both of these geometries is the inability to easily tune the reflectivity of the external cavity without swapping components and the technical impracticality of constructing and maintaining free-space alignment of the cavity spanning an optical path length of beyond ~ 10 cm.

The project described in this section attempts to circumvent these problems with a new configuration, modified from [146]. The frequency selectivity is achieved by using a DFB/DBR diode as the source, which has a microfabricated structure providing frequency selectivity down to ~ 1 MHz. (This choice, of course limits the wavelength tuning range to < 1 nm.) The cavity is constructed by using a waveplate, polarizing beam-splitter (PBS) and a 1 m retro-reflecting fiber (Thorlabs part no P1-780PMR-P01-1)[1]. The waveplate and PBS allow for a variable fraction of light to be sent into the fiber, and guiding the light in the cavity inside a fiber allows us to construct a cavity much longer than in the typical ECDL, as pointing instability is entirely eliminated. A block diagram of the layout as well

[1]Coupling light into a fiber with no output ports is facilitated by the use of a PBS and waveplate in the optical path. The light reflected back out of the fiber can be directed into a different spatial mode than the light source itself by adjustment of the waveplate. However, the reflection off the fiber facet while the alignment is poor can often obscure the desired signal, so beware!

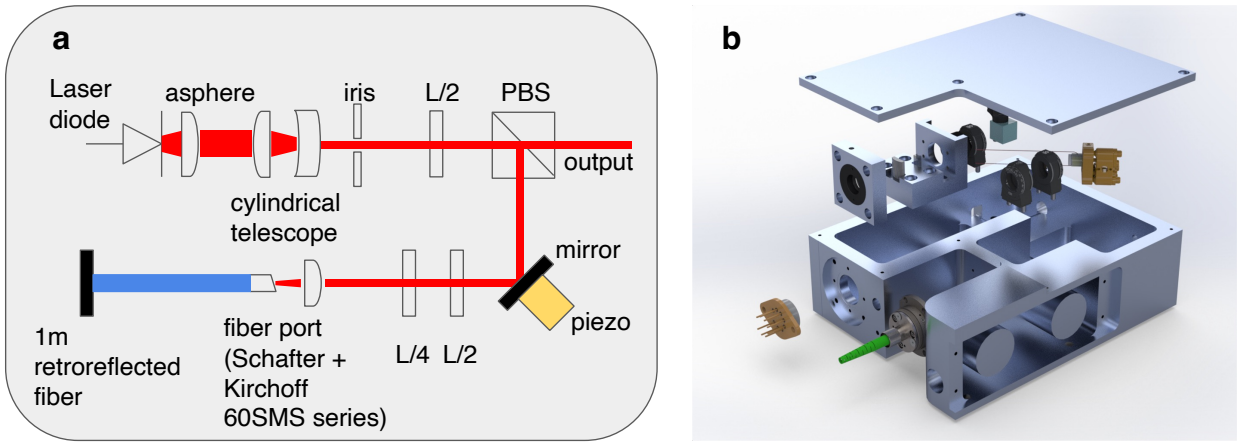

Figure B.1: (a) A block diagram of the laser design described in this section. The elements' flat surfaces have been tilted a few degrees away from the optical propagation axis to avoid spurious reflections (not shown). (b) A CAD rendering of an early version of this design. The cylindrical telescope mount has been replaced with a rail system for simpler adjustment of spacing between lenses.

as a CAD rendering of this system is shown in figure B.1.

A pair of lasers following this design was constructed using DFB diodes (part no. EYP-DFB-0767-00050-1500-TOC03-0005, discontinued) from Eagleyard. We then characterized their amplitude (see figure B.2a) and frequency noise, as well as their frequency modulation transfer function. Since frequency fluctuations of ∼MHz are not directly detectable on a photodiode, and in fact there is no industry standard for measuring linewidth [147], we outline in the next paragraph our methodology for the latter set of measurements. The work covered here is supplemented by presentation slides circulated internally within the Zwierlein group, which also detail some of the intricacies of assembling this system.

In essence, what we would like is a setup that can convert small changes in an optical frequency into a voltage. In principle, this can be done with a self-(homo)heterodyne measurement using an interferometer with imbalanced arm lengths (longer than the coherence length of the laser under test), by beating against a reference laser of known (narrow) linewidth, or monitoring the transmission through a length-adjustable high-finesse cavity. These methods are prohibitive, as the former requires $\sim$ 100 km of path length (fiber) to measure linewidths of $\sim$ 10 kHz (which is achievable with free-running ECDLs), while the latter requires a state-of-the-art stabilized laser/cavity system to be already be operational. We instead measured fluctuations of transmission through a low-finesse (and therefore high-bandwidth) cavity, while the cavity length is tuned such that the transmission is maximally sensitive to small variations in frequency. This is schematically shown in figure 1 of [146]. The power spectrum of this signal allows us to estimate the free-running linewidth of this laser [148], as shown in figure B.2. Using the same setup, we then also modulate the current supplied to the diode over several different frequencies, and measure the frequency modulation response, see figure B.3.

As stabilizing a laser to an optical reference is also a common use case, we also demonstrate a relative phase lock between two lasers of this design, with one as the reference and

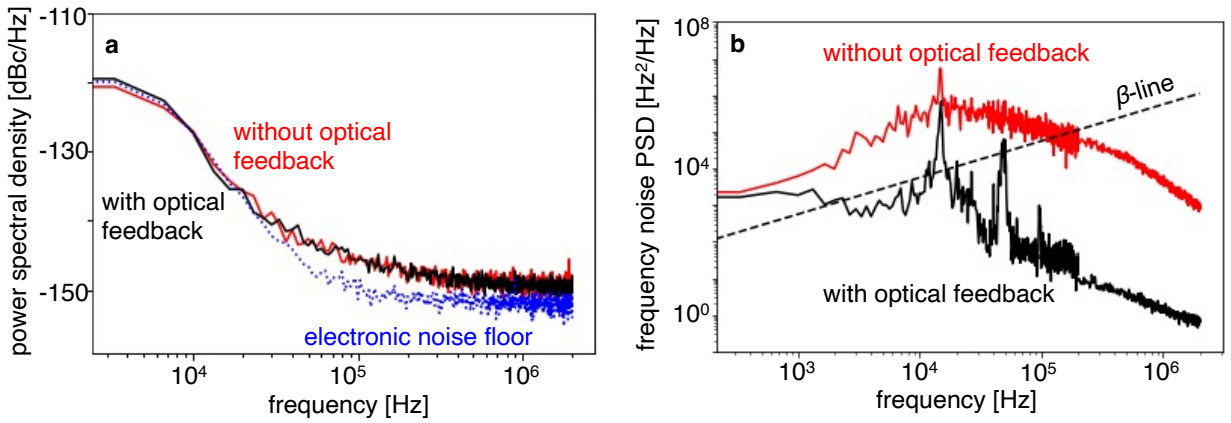

Figure B.2: Two separate ECDL noise measurements with (black traces) and without (red traces) optical feedback from the cavity formed by the retroreflecting fiber. (a) A relative noise intensity measurement, taken with simply a photodiode at the laser output, shows no obvious difference between the two configurations. This data was taken by Elisa Soave. (b) A frequency noise measurement, taken using a low-finesse optical cavity, shows that with optical feedback, the linewidth of the laser is reduced by an order of magnitude, as indicated by the intersection with the β-line. Strong peaks in the black trace at $\sim 1, 3$ kHz are likely due to the slow servo (keeping the cavity on the transmission flank) bandwidth and the natural mechanical resonance frequency of the cavity.

the second as the follower by applying closed-loop feedback to its current source. The phase difference between the lasers is converted into a voltage (linearly proportional to the phase) by taking their optical beat signal on a photodiode and using a phase-frequency discriminator circuit (PFD). In this project we use a PFD circuit design adapted from Professor Guglielmo Maria Tino's group at LENS[2]. As shown in figure B.3, by enabling the closed-loop feedback, the optical beat signal becomes more coherent, as we see a large portion of its power transferred to the carrier. Secondarily, the optical beat signal without feedback can be used also to estimate the linewidth of these lasers, assuming that their frequency fluctuations are independent and identical (in a statistical sense).

We have yet to deploy this pair of lasers in an experiment or monitor its long-term performance, and therefore we cannot attest if this design is stable against long-term drifts. While the temperature-stabilized uni-body housing and the use of fasteners rather than glue for most optical components is intended to preserve the free-space alignment over time, one major flaw we failed to consider is the temperature/humidity sensitivity of the index of refraction of the fiber forming the majority of the cavity. For a typical drift of 1 degree Celsius in the laboratory and a 1 m fiber, we will correspondingly get a drift in the optical path length of $\sim 10\mu$m, or approximately ten times the free spectral range of the external cavity [151]. This places demanding requirements on the frequency tuning range needed and actuated by either the piezoelectric or current feedback. We speculate that for stable operation, this laser will have to be placed in a stringent climate-controlled environment. Furthermore, in terms of free-running frequency noise characteristics, it fails to significantly

[2]My colleague Yiming Zhang has also recently tested his own design, modified from [150].

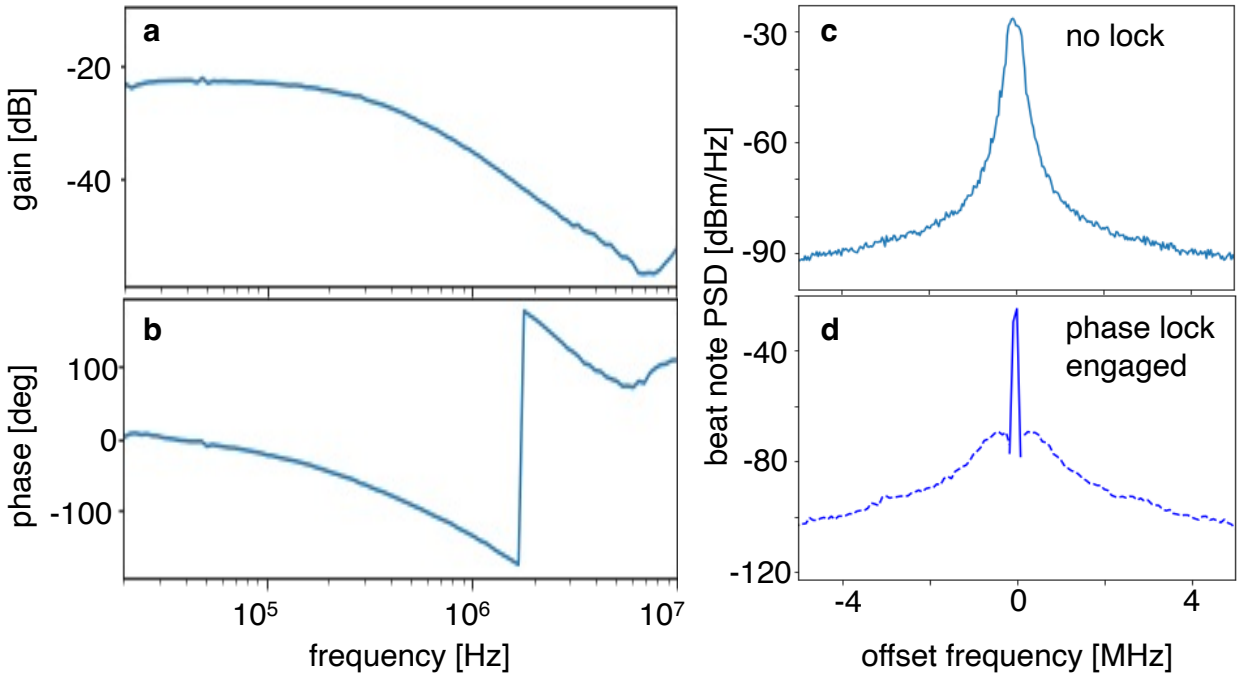

Figure B.3: (a, b) The FM response function is measured using a vector network analyzer by modulating the current source driving the diode and recording the transmission signal through a low-finesse optical cavity. (The gain is normalized to arbitrary units.) This shows the low-pass filter behavior expected from the thermal mechanism of the frequency modulation [149]. (c, d) The spectrum of the beat note, showing the effect of the phase lock. In (d), two different bandwidth settings (dashed, solid curves) are used to measure the spectrum far (near) from the carrier.

outperform the interference filter laser design from our former postdoc Carsten Robens, which has been iterated through almost ten development cycles and has most recently been measured by my colleague Eric Wolf for an 804 nm ECDL to have ∼10 kHz linewidth. Therefore, we cannot at this moment recommend this laser system over more traditional designs, but we note that during the completion of this project, similar work incorporating an EOM in the feedback path was performed as well [152].

Appendix C

Development of a resonant 1.7GHz free-space EOM

Here we will describe modifications to the method for constructing free-space electro-optic modulators operating in the GHz range, as described in the internal document "Electrooptic Phase Modulators for Na Beam Repumping" by Chandra Raman and the thesis [153]. The original design has historically been used in the Ketterle and Zwierlein labs at MIT. The method described should work equally well for other wavelengths, provided the crystal used has the appropriate anti-reflection coating.

The motivation for this work stems from some flaws of the original design. They include

- a lack of both mechanical and thermal stability, due to construction from a thin copper foil,
- an ensuing warm-up/cool-down behavior of the resonator's natural frequency that causes the generated sideband amplitude to fluctuate over time, potentially causing problems with atom loading,
- a lack of design intent for active thermal stabilization, i.e., no features for mounting a temperature probe or thermo-electric cooling cell, with a small fan mounted nearby being the only method of passive temperature control[1],
- polarization fluctuations of the output due to birefringence of the crystal and coupled to its temperature,
- overheating leading to melting and flowing of the indium foil used to make contact between the crystal and the resonator, which can short the resonator or damage the crystal,
- a resonator Q that will vary significantly between constructions due to finite hand-precision,
- a bespoke and delicate assembly procedure that requires an amount of training and scrapping unusable resonators that is unfavorable for low-volume production, as is commonly the case in our labs.

[1] Adding fans to optics setups is undesirable as they can generate turbulent flow near the optical path.

The new design presents a low-cost alternative to industry-standard, commercially-available solutions (for example, part no. PM9-VIS from Qubig) which also address these issues, albeit with superior specifications to even the updated home-built design.

The original design, in which the LC resonator is formed mostly by hand from copper foil, is shown schematically in figure C.1a. The new design consists of solid copper parts in a "split-ring" geometry that can be manufactured on any standard milling machine, e.g. in the Edgerton machine shop. Some machining is needed for both designs, since the original requires precision "molds" that act as negatives for shaping the copper foil. The new design takes full advantage of machining. This leads to several benefits, including

- the precision of the part being determined finally by the quality of machining, not the final hand-assembly step,
- a smooth surface finish for electrical contact that can be achieved through standard manufacturing processes, such as setting a particular speed and feed on the machine, rather than sanding,
- large flat surfaces where a TEC and thermistor can easily be accomodated,
- lips in the flat portion of the resonator that prevent the crystal from slipping around during assembly.

This design has been tested on the bench, as shown in figure C.1c. The sideband amplitude decreases by a factor of two across a 23 MHz FWHM range, centered around a peak sideband generation efficiency at 1.53GHz. This gives us an estimate for the system's quality factor $Q \approx 70$[2]. This figure should be interpreted remembering that the resonator is not an isolated system, and its coupling to the microwave antenna delivering the drive power can depend on the placement and construction of the antenna. The resonance frequency can be increased by at least 200 MHz by inserting a metallic rod[3] into the "keyhole" to reduce its volume, at the expense of reducing Q by approximately a factor of 2. The need for tuning can be entirely avoided by making small modifications to the dimensions of the resonator[4].

This design has yet to be integrated into an experiment, and further improvement in the efficiency of sideband generation is possible by improved design of the microwave antenna as well.

[2]For comparison, the modulators from Qubig have a $Q \approx 300$.

[3]coated with shrink wrap to prevent slipping

[4]A smaller keyhole radius will give a higher resonance frequency. Therefore, we would recommend slightly underestimating the required dimensions and increasing the radius until the desired resonance frequency is achieved.

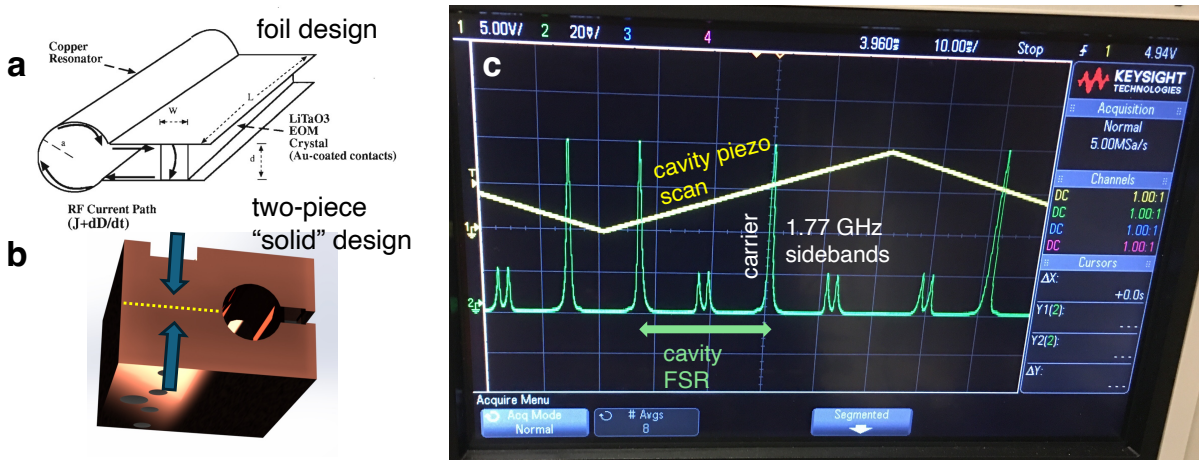

Figure C.1: (a) Reproduced from Chandra Raman's internal document. (b) CAD rendering of new design. The groove housing the crystal is designed to be 1–2 mm wider than the crystal itself, so that indium foil can be used to ensure good electrical contact. Pressure can be adjusted using fasteners along the axis indicated by the blue arrows. (c) Prototype of new design imprints 1.77 GHz sidebands with $\sim 25\%$ power relative to the carrier when driven with a 1 W loop antenna placed near the cylindrical cavity of the resonator, as verified with 589 nm laser light and scanning Fabry-Perot cavity.

References

[1] R. P. Feynman, "Simulating physics with computers," *International Journal of Theoretical Physics*, 1982. DOI: 10.1007/BF02650179.

[2] E. Altman, K. R. Brown, G. Carleo, *et al.*, "Quantum simulators: Architectures and opportunities," *PRX Quantum*, vol. 2, p. 017 003, 1 Feb. 2021. DOI: 10.1103/PRXQuantum.2.017003. [Online]. Available: https://link.aps.org/doi/10.1103/PRXQuantum.2.017003.

[3] A. D. Ludlow, M. M. Boyd, J. Ye, E. Peik, and P. O. Schmidt, "Optical atomic clocks," *Reviews of Modern Physics*, vol. 87, pp. 637–701, 2 Jun. 2015, ISSN: 0034-6861. DOI: 10.1103/RevModPhys.87.637. [Online]. Available: https://link.aps.org/doi/10.1103/RevModPhys.87.637.

[4] C. L. Degen, F. Reinhard, and P. Cappellaro, "Quantum sensing," *Reviews of Modern Physics*, vol. 89, p. 035 002, 3 Jul. 2017, ISSN: 0034-6861. DOI: 10.1103/RevModPhys.89.035002. [Online]. Available: http://link.aps.org/doi/10.1103/RevModPhys.89.035002.

[5] D. S. Weiss and M. Saffman, *Quantum computing with neutral atoms*, Jul. 2017. DOI: 10.1063/PT.3.3626.

[6] C. Monroe, W. C. Campbell, L. M. Duan, *et al.*, "Programmable quantum simulations of spin systems with trapped ions," *Reviews of Modern Physics*, vol. 93, 2 Apr. 2021, ISSN: 15390756. DOI: 10.1103/RevModPhys.93.025001.

[7] M. Safronova, D. Budker, D. DeMille, D. F. J. Kimball, A. Derevianko, and C. W. Clark, "Search for new physics with atoms and molecules," *Reviews of Modern Physics*, vol. 90, p. 025 008, 2 Jun. 2018, ISSN: 0034-6861. DOI: 10.1103/RevModPhys.90.025008. [Online]. Available: https://link.aps.org/doi/10.1103/RevModPhys.90.025008.

[8] C. Regal, "Experimental realization of bcs-bec crossover physics with a fermi gas of atoms," Ph.D. dissertation, University of Colorado, Boulder, 2001.

[9] K.-K. Ni, "A quantum gas of polar molecules," Ph.D. dissertation, University of Colorado, Boulder, 2009.

[10] W. C. Campbell and J. M. Doyle, *Cooling, trap loading, and beam production using a cryogenic helium buffer gas*, 2008.

[11] E. S. Shuman, J. F. Barry, and D. Demille, "Laser cooling of a diatomic molecule," *Nature*, vol. 467, pp. 820–823, 7317 Oct. 2010, ISSN: 00280836. DOI: 10.1038/nature09443.

[12] C. J. Yu, S. V. Kugelgen, D. W. Laorenza, and D. E. Freedman, "A molecular approach to quantum sensing," *ACS Central Science*, vol. 7, pp. 712–723, 5 May 2021, ISSN: 23747951. DOI: 10.1021/acscentsci.0c00737.

[13] D. DeMille, N. R. Hutzler, A. M. Rey, and T. Zelevinsky, *Quantum sensing and metrology for fundamental physics with molecules*, May 2024. DOI: 10.1038/s41567-024-02499-9.

[14] S. L. Cornish, M. R. Tarbutt, and K. R. Hazzard, *Quantum computation and quantum simulation with ultracold molecules*, May 2024. DOI: 10.1038/s41567-024-02453-9.

[15] B. Sundar, B. Gadway, and K. R. Hazzard, "Synthetic dimensions in ultracold polar molecules," *Scientific Reports*, vol. 8, 1 Dec. 2018, ISSN: 20452322. DOI: 10.1038/s41598-018-21699-x.

[16] P. Scholl, M. Schuler, H. J. Williams, *et al.*, "Quantum simulation of 2d antiferromagnets with hundreds of rydberg atoms," *Nature*, vol. 595, pp. 233–238, 7866 Jul. 2021, ISSN: 0028-0836. DOI: 10.1038/s41586-021-03585-1. [Online]. Available: https://www.nature.com/articles/s41586-021-03585-1.

[17] A. Frisch, "Dipolar quantum gases of erbium," Ph.D. dissertation, University of Innsbruck, 2014.

[18] E. G. V. Loon, M. I. Katsnelson, and M. Lemeshko, "Ultralong-range order in the fermi-hubbard model with long-range interactions," *Physical Review B - Condensed Matter and Materials Physics*, vol. 92, 8 Aug. 2015, ISSN: 1550235X. DOI: 10.1103/PhysRevB.92.081106.

[19] S. A. Will, J. W. Park, Z. Z. Yan, H. Loh, and M. W. Zwierlein, "Coherent microwave control of ultracold $^{23}Na^{40}K$ molecules," *Phys. Rev. Lett.*, vol. 116, p. 225 306, 22 Jun. 2016. DOI: 10.1103/PhysRevLett.116.225306. [Online]. Available: https://link.aps.org/doi/10.1103/PhysRevLett.116.225306.

[20] R. R. Wang and J. L. Bohn, "Viscous dynamics of a quenched trapped dipolar fermi gas," *Physical Review A*, vol. 108, 1 Jul. 2023, ISSN: 24699934. DOI: 10.1103/PhysRevA.108.013322.

[21] J. R. Li, K. Matsuda, C. Miller, A. N. Carroll, W. G. Tobias, J. S. Higgins, and J. Ye, "Tunable itinerant spin dynamics with polar molecules," *Nature*, vol. 614, pp. 70–74, 7946 Feb. 2023, ISSN: 14764687. DOI: 10.1038/s41586-022-05479-2.

[22] J. S. Rosenberg, L. Christakis, E. Guardado-Sanchez, Z. Z. Yan, and W. S. Bakr, "Observation of the hanbury brown–twiss effect with ultracold molecules," *Nature Physics*, vol. 18, pp. 1062–1066, 9 Sep. 2022, ISSN: 17452481. DOI: 10.1038/s41567-022-01695-9.

[23] L. Christakis, J. S. Rosenberg, R. Raj, S. Chi, A. Morningstar, D. A. Huse, Z. Z. Yan, and W. S. Bakr, "Probing site-resolved correlations in a spin system of ultracold molecules," *Nature*, vol. 614, pp. 64–69, 7946 Feb. 2023, ISSN: 14764687. DOI: 10.1038/s41586-022-05558-4.

[24] N. R. Cooper and G. V. Shlyapnikov, "Stable topological superfluid phase of ultracold polar fermionic molecules," *Physical Review Letters*, vol. 103, 15 Oct. 2009, ISSN: 00319007. DOI: 10.1103/PhysRevLett.103.155302.

[25] F. Deng, X. Y. Chen, X. Y. Luo, W. Zhang, S. Yi, and T. Shi, "Effective potential and superfluidity of microwave-shielded polar molecules," *Physical Review Letters*, vol. 130, 18 May 2023, ISSN: 10797114. DOI: 10.1103/PhysRevLett.130.183001.

[26] M. C. Gutzwiller, J. Kanamori, J. B. Hubbard, Jördens, and H. Esslinger, "The hubbard model at half a century," *Nature Physics*, vol. 9, pp. 523–523, 2013. [Online]. Available: https://api.semanticscholar.org/CorpusID:256712926.

[27] X.-Y. Chen, "Microwave-shielded ultracold polar molecules," Ph.D. dissertation, Ludwig Maximilian University of Munich, 2023.

[28] C.-H. Wu, "Strongly interacting quantum mixtures of ultracold atoms," Ph.D. dissertation, MASSACHUSETTS INSTITUTE OF TECHNOLOGY, 2013.

[29] J. W. Park, S. A. Will, and M. W. Zwierlein, "Ultracold dipolar gas of fermionic na23k40 molecules in their absolute ground state," *Physical Review Letters*, vol. 114, 20 May 2015, ISSN: 10797114. DOI: 10.1103/PhysRevLett.114.205302.

[30] B. P. Maddox, J. M. Mortlock, T. R. Hepworth, A. P. Raghuram, P. D. Gregory, A. Guttridge, and S. L. Cornish, "Enhanced quantum state transfer via feedforward cancellation of optical phase noise," *ArXiv preprint*, Jul. 2024. [Online]. Available: http://arxiv.org/abs/2407.09119.

[31] C. Warner, N. Bigagli, A. Z. Lam, W. Yuan, S. Zhang, I. Stevenson, and S. Will, "Efficient pathway to nacs ground state molecules," *New Journal of Physics*, vol. 25, 5 May 2023, ISSN: 13672630. DOI: 10.1088/1367-2630/acd411.

[32] R. Bause, A. Kamijo, X. Y. Chen, M. Duda, A. Schindewolf, I. Bloch, and X. Y. Luo, "Efficient conversion of closed-channel-dominated feshbach molecules of to their absolute ground state," *Physical Review A*, vol. 104, 4 Oct. 2021, ISSN: 24699934. DOI: 10.1103/PhysRevA.104.043321.

[33] C.-H. Wu, J. W. Park, P. Ahmadi, S. Will, and M. W. Zwierlein, "Ultracold fermionic feshbach molecules of {23}na{40}k," *Physical Review Letters*, Jun. 2012. DOI: 10.1103/PhysRevLett.109.085301. [Online]. Available: http://arxiv.org/abs/1206.5023%20http://dx.doi.org/10.1103/PhysRevLett.109.085301.

[34] A. G. Truscott, K. E. Strecker, W. I. McAlexander, G. B. Partridge, and R. G. Hulet, "Observation of fermi pressure in a gas of trapped atoms," *Science*, vol. 291, pp. 2570–2572, 5513 Mar. 2001, ISSN: 00368075. DOI: 10.1126/science.1059318.

[35] L. D. Marco, G. Valtolina, K. Matsuda, W. G. Tobias, J. P. Covey, and J. Ye, "A degenerate fermi gas of polar molecules," *Science*, vol. 363, pp. 853–856, 6429 Feb. 2019, ISSN: 0036-8075. DOI: 10.1126/science.aau7230. [Online]. Available: https://www.science.org/doi/10.1126/science.aau7230.

[36] J. Cao, H. Yang, Z. Su, X.-Y. Wang, J. Rui, B. Zhao, and J.-W. Pan, "Preparation of a quantum degenerate mixture of ^{23}Na^{40}K molecules and ^{40}K atoms," *Phys. Rev. A*, vol. 107, p. 013 307, 1 Jan. 2023. DOI: 10.1103/PhysRevA.107.013307. [Online]. Available: https://link.aps.org/doi/10.1103/PhysRevA.107.013307.

[37] M. Duda, X. Y. Chen, A. Schindewolf, R. Bause, J. von Milczewski, R. Schmidt, I. Bloch, and X. Y. Luo, "Transition from a polaronic condensate to a degenerate fermi gas of heteronuclear molecules," *Nature Physics*, vol. 19, pp. 720–725, 5 May 2023, ISSN: 17452481. DOI: 10.1038/s41567-023-01948-1.

[38] Z. Z. Yan, Y. Ni, C. Robens, and M. W. Zwierlein, "Bose polarons near quantum criticality," *Science*, vol. 368, pp. 190–194, 6487 Apr. 2020, ISSN: 0036-8075. DOI: 10.1126/science.aax5850. [Online]. Available: https://www.science.org/doi/10.1126/science.aax5850.

[39] L. D. Landau, "Electron motion in crystal lattices," *Phys. Z. Sowjet.*, vol. 3, p. 664, 1933.

[40] S. Pekar, "Autolocalization of the electron in an inertially polarizable dielectric medium," *Zh. Eksp. Teor. Fiz*, vol. 16, p. 335, 1946.

[41] Y. Ni, "Atoms and molecules immersed in a bose-einstein condensate," Ph.D. dissertation, MIT, 2023.

[42] C. E. Klauss, X. Xie, C. Lopez-Abadia, J. P. D'Incao, Z. Hadzibabic, D. S. Jin, and E. A. Cornell, "Observation of efimov molecules created from a resonantly interacting bose gas," *Phys. Rev. Lett.*, vol. 119, p. 143 401, 14 Oct. 2017. DOI: 10.1103/PhysRevLett.119.143401. [Online]. Available: https://link.aps.org/doi/10.1103/PhysRevLett.119.143401.

[43] A. S. Jensen, K. Riisager, D. V. Fedorov, and E. Garrido, "Structure and reactions of quantum halos," *Reviews of Modern Physics*, vol. 76, pp. 215–261, 1 Feb. 2004, ISSN: 0034-6861. DOI: 10.1103/RevModPhys.76.215. [Online]. Available: https://link.aps.org/doi/10.1103/RevModPhys.76.215.

[44] V. Efimov, "Energy levels arising from resonant two-body forces in a three-body system," *Phys. Lett. B*, vol. 33, no. 8, pp. 563–564, 1970, ISSN: 0370-2693. DOI: https://doi.org/10.1016/0370-2693(70)90349-7. [Online]. Available: http://www.sciencedirect.com/science/article/pii/0370269370903497.

[45] T. Kraemer, M. Mark, P. Waldburger, *et al.*, "Evidence for efimov quantum states in an ultracold gas of caesium atoms," *Nature*, vol. 440, pp. 315–318, 7082 Mar. 2006, ISSN: 14764687. DOI: 10.1038/nature04626.

[46] B. Huang, L. A. Sidorenkov, R. Grimm, and J. M. Hutson, "Observation of the second triatomic resonance in efimov's scenario," *Physical Review Letters*, Feb. 2014. DOI: 10.1103/PhysRevLett.112.190401. [Online]. Available: http://arxiv.org/abs/1402.6161%20http://dx.doi.org/10.1103/PhysRevLett.112.190401.

[47] R. Pires, J. Ulmanis, S. Häfner, M. Repp, A. Arias, E. D. Kuhnle, and M. Weidemüller, "Observation of efimov resonances in a mixture with extreme mass imbalance," *Physical Review Letters*, Mar. 2014. DOI: 10.1103/PhysRevLett.112.250404. [Online]. Available: http://arxiv.org/abs/1403.7246%20http://dx.doi.org/10.1103/PhysRevLett.112.250404.

[48] S.-K. Tung, K. Jimenez-Garcia, J. Johansen, C. V. Parker, and C. Chin, "Geometric scaling of efimov states in a ${}^{6}\{Li\}$-${}^{133}\{Cs\}$ mixture," *Physical Review Letters*, Feb. 2014. DOI: 10.1103/PhysRevLett.113.240402. [Online]. Available: http://arxiv.org/abs/1402.5943%20http://dx.doi.org/10.1103/PhysRevLett.113.240402.

[49] M. Kunitski, S. Zeller, J. Voigtsberger, *et al.*, "Observation of the efimov state of the helium trimer," *Science*, vol. 348, pp. 551–555, 6234 May 2015, ISSN: 0036-8075. DOI: 10.1126/science.aaa5601. [Online]. Available: https://www.science.org/doi/10.1126/science.aaa5601.

[50] P. Naidon and S. Endo, "Efimov physics: A review," *Reports on Progress in Physics*, vol. 80, p. 056 001, 5 May 2017, ISSN: 0034-4885. DOI: 10.1088/1361-6633/aa50e8. [Online]. Available: https://iopscience.iop.org/article/10.1088/1361-6633/aa50e8.

[51] W. Ketterle and M. W. Zwierlein, "Making, probing and understanding ultracold fermi gases," *La Rivista del Nuovo Cimento*, vol. 31, no. 506, pp. 247–422, Jul. 2008, ISSN: 0393697X, 0393697X. DOI: 10.1393/ncr/i2008-10033-1. [Online]. Available: https://doi.org/10.1393/ncr/i2008-10033-1.

[52] C. Chin, R. Grimm, P. Julienne, and E. Tiesinga, "Feshbach resonances in ultracold gases," *Reviews of Modern Physics*, vol. 82, pp. 1225–1286, 2 Apr. 2010, ISSN: 0034-6861. DOI: 10.1103/RevModPhys.82.1225. [Online]. Available: https://link.aps.org/doi/10.1103/RevModPhys.82.1225.

[53] C. Kuhlenkamp, M. Knap, M. Wagner, R. Schmidt, and A. Imamoğlu, "Tunable feshbach resonances and their spectral signatures in bilayer semiconductors," *Physical Review Letters*, vol. 129, 3 Jul. 2022, ISSN: 10797114. DOI: 10.1103/PhysRevLett.129.037401.

[54] E. Braaten and H.-W. Hammer, "Universality in few-body systems with large scattering length," *Physics Reports*, vol. 428, no. 5, pp. 259–390, 2006, ISSN: 0370-1573. DOI: https://doi.org/10.1016/j.physrep.2006.03.001. [Online]. Available: https://www.sciencedirect.com/science/article/pii/S0370157306000822.

[55] R. K. Bhaduri, A. Chatterjee, and B. P. van Zyl, "An elementary exposition of the Efimov effect," *American Journal of Physics*, vol. 79, no. 3, pp. 274–281, Mar. 2011, ISSN: 0002-9505. DOI: 10.1119/1.3533428. eprint: https://pubs.aip.org/aapt/ajp/article-pdf/79/3/274/13092418/274_1_online.pdf. [Online]. Available: https://doi.org/10.1119/1.3533428.

[56] L. H. Thomas, "The interaction between a neutron and a proton and the structure of H^3," *Phys. Rev.*, vol. 47, pp. 903–909, 12 Jun. 1935. DOI: 10.1103/PhysRev.47.903. [Online]. Available: https://link.aps.org/doi/10.1103/PhysRev.47.903.

[57] A. Christianen, "Chemistry in a quantum medium," Ph.D. dissertation, TUM School of Natural Sciences, 2023.

[58] J. van de Kraats, D. J. M. Ahmed-Braun, J.-L. Li, and S. J. J. M. F. Kokkelmans, "Efimovian three-body potential from broad to narrow feshbach resonances," *Phys. Rev. A*, vol. 107, p. 023 301, 2 Feb. 2023. DOI: 10.1103/PhysRevA.107.023301. [Online]. Available: https://link.aps.org/doi/10.1103/PhysRevA.107.023301.

[59] Y. E. Shchadilova, R. Schmidt, F. Grusdt, and E. Demler, "Quantum dynamics of ultracold bose polarons," *Phys. Rev. Lett.*, vol. 117, p. 113 002, 11 Sep. 2016. DOI: 10.1103/PhysRevLett.117.113002. [Online]. Available: https://link.aps.org/doi/10.1103/PhysRevLett.117.113002.

[60] F. Chevy, "Universal phase diagram of a strongly interacting fermi gas with unbalanced spin populations," *Phys. Rev. A*, vol. 74, p. 063 628, 6 Dec. 2006. DOI: 10.1103/PhysRevA.74.063628. [Online]. Available: https://link.aps.org/doi/10.1103/PhysRevA.74.063628.

[61] N.-E. Guenther, P. Massignan, M. Lewenstein, and G. M. Bruun, "Bose polarons at finite temperature and strong coupling," *Phys. Rev. Lett.*, vol. 120, p. 050 405, 5 Feb. 2018. DOI: 10.1103/PhysRevLett.120.050405. [Online]. Available: https://link.aps.org/doi/10.1103/PhysRevLett.120.050405.

[62] B. Field, J. Levinsen, and M. M. Parish, "Fate of the bose polaron at finite temperature," *Phys. Rev. A*, vol. 101, p. 013 623, 1 Jan. 2020. DOI: 10.1103/PhysRevA.101.013623. [Online]. Available: https://link.aps.org/doi/10.1103/PhysRevA.101.013623.

[63] J. W. Park, "An ultracold gas of dipolar fermionic 23na40k molecules," Ph.D. dissertation, MASSACHUSETTS INSTITUTE OF TECHNOLOGY, 2016.

[64] Z. Z. Yan, "From strongly-interacting bose-fermi mixtures to ultracold molecules," Ph.D. dissertation, MASSACHUSETTS INSTITUTE OF TECHNOLOGY, 2020.

[65] Z. Z. Yan, Y. Ni, A. Chuang, P. E. Dolgirev, K. Seetharam, E. Demler, C. Robens, and M. Zwierlein, "Collective flow of fermionic impurities immersed in a bose–einstein condensate," *Nature Physics*, Jun. 2024, ISSN: 1745-2473. DOI: 10.1038/s41567-024-02541-w. [Online]. Available: https://www.nature.com/articles/s41567-024-02541-w.

[66] L. D. Landau and E. M. Lifshitz, *Mechanics, Third Edition: Volume 1 (Course of Theoretical Physics)*, 3rd ed. Butterworth-Heinemann, 1976, ISBN: 0750628960.

[67] S. Gupta, Z. Hadzibabic, M. W. Zwierlein, C. A. Stan, K. Dieckmann, C. H. Schunck, E. G. M. van Kempen, B. J. Verhaar, and W. Ketterle, "Radio-frequency spectroscopy of ultracold fermions," *Science*, vol. 300, no. 5626, pp. 1723–1726, 2003. DOI: 10.1126/science.1085335. eprint: https://www.science.org/doi/pdf/10.1126/science.1085335. [Online]. Available: https://www.science.org/doi/abs/10.1126/science.1085335.

[68] L. Pauling, "The application of the quantum mechanics to the structure of the hydrogen molecule and hydrogen molecule-ion and to related problems.," *Chemical Reviews*, vol. 5, no. 2, pp. 173–213, 1928.

[69] A. Carrington, I. R. McNab, and C. A. Montgomerie, "Spectroscopy of the hydrogen molecular ion," *Journal of Physics B: Atomic, Molecular and Optical Physics*, vol. 22, no. 22, p. 3551, 1989.

[70] H. Collard, R. Hofstadter, E. B. Hughes, A. Johansson, M. R. Yearian, R. B. Day, and R. T. Wagner, "Elastic electron scattering from tritium and helium-3," *Phys. Rev.*, vol. 138, B57–B65, 1B Apr. 1965. DOI: 10.1103/PhysRev.138.B57. [Online]. Available: https://link.aps.org/doi/10.1103/PhysRev.138.B57.

[71] R. Cruz-Torres, D. Nguyen, F. Hauenstein, A. Schmidt, S. Li, D. Abrams, H. Albataineh, S. Alsalmi, D. Androic, K. Aniol, *et al.*, "Probing few-body nuclear dynamics via h 3 and he 3 (e, e p) pn cross-section measurements," *Physical review letters*, vol. 124, no. 21, p. 212 501, 2020.

[72] W. Schöllkopf and J. P. Toennies, "The nondestructive detection of the helium dimer and trimer," *The Journal of chemical physics*, vol. 104, no. 3, pp. 1155–1158, 1996.

[73] M. Kunitski, S. Zeller, J. Voigtsberger, A. Kalinin, L. P. H. Schmidt, M. Schöffler, A. Czasch, W. Schöllkopf, R. E. Grisenti, T. Jahnke, *et al.*, "Observation of the efimov state of the helium trimer," *Science*, vol. 348, no. 6234, pp. 551–555, 2015.

[74] L. H. Thomas, "The interaction between a neutron and a proton and the structure of H^3," *Phys. Rev.*, vol. 47, pp. 903–909, 12 Jun. 1935. DOI: 10.1103/PhysRev.47.903. [Online]. Available: https://link.aps.org/doi/10.1103/PhysRev.47.903.

[75] P. Naidon and S. Endo, "Efimov physics: A review," *Reports on Progress in Physics*, vol. 80, no. 5, p. 056 001, 2017.

[76] T. Kraemer, M. Mark, P. Waldburger, J. G. Danzl, C. Chin, B. Engeser, A. D. Lange, K. Pilch, A. Jaakkola, H.-C. Nägerl, *et al.*, "Evidence for efimov quantum states in an ultracold gas of caesium atoms," *Nature*, vol. 440, no. 7082, pp. 315–318, 2006.

[77] M. Zaccanti, B. Deissler, C. D'Errico, M. Fattori, M. Jona-Lasinio, S. Müller, G. Roati, M. Inguscio, and G. Modugno, "Observation of an efimov spectrum in an atomic system," *Nature Physics*, vol. 5, no. 8, pp. 586–591, 2009.

[78] B. Huang, L. A. Sidorenkov, R. Grimm, and J. M. Hutson, "Observation of the second triatomic resonance in efimov's scenario," *Physical review letters*, vol. 112, no. 19, p. 190 401, 2014.

[79] S.-K. Tung, K. Jimenez-Garcia, J. Johansen, C. V. Parker, and C. Chin, "Geometric scaling of efimov states in a {6}{Li}-{133}{Cs} mixture," *Physical Review Letters*, Feb. 2014. DOI: 10.1103/PhysRevLett.113.240402. [Online]. Available: http://arxiv.org/abs/1402.5943%20http://dx.doi.org/10.1103/PhysRevLett.113.240402.

[80] R. Pires, J. Ulmanis, S. Haefner, M. Repp, A. Arias, E. D. Kuhnle, and M. Weidemueller, "Observation of Efimov Resonances in a Mixture with Extreme Mass Imbalance," *Phys. Rev. Lett.*, vol. 112, p. 250 404, 25 Jun. 2014. DOI: 10.1103/PhysRevLett.112.250404. [Online]. Available: https://link.aps.org/doi/10.1103/PhysRevLett.112.250404.

[81] T. Lompe, T. B. Ottenstein, F. Serwane, A. N. Wenz, G. Zürn, and S. Jochim, "Radio-frequency association of efimov trimers," *Science*, vol. 330, no. 6006, pp. 940–944, 2010.

[82] S. Nakajima, M. Horikoshi, T. Mukaiyama, P. Naidon, and M. Ueda, "Measurement of an efimov trimer binding energy in a three-component mixture of li 6," *Physical review letters*, vol. 106, no. 14, p. 143 201, 2011.

[83] E. Nielsen, D. Fedorov, and A. Jensen, "The structure of the atomic helium trimers: Halos and efimov states," *Journal of Physics B: Atomic, Molecular and Optical Physics*, vol. 31, no. 18, p. 4085, 1998.

[84] S. Knoop, T. Schuster, R. Scelle, A. Trautmann, J. Appmeier, M. K. Oberthaler, E. Tiesinga, and E. Tiemann, "Feshbach spectroscopy and analysis of the interaction potentials of ultracold sodium," *Phys. Rev. A*, vol. 83, p. 042 704, 4 Apr. 2011. DOI: 10.1103/PhysRevA.83.042704. [Online]. Available: https://link.aps.org/doi/10.1103/PhysRevA.83.042704.

[85] Z.-Y. Shi, S. M. Yoshida, M. M. Parish, and J. Levinsen, "Impurity-induced multibody resonances in a bose gas," *Phys. Rev. Lett.*, vol. 121, p. 243 401, 24 Dec. 2018. DOI: 10.1103/PhysRevLett.121.243401. [Online]. Available: https://link.aps.org/doi/10.1103/PhysRevLett.121.243401.

[86] S. M. Yoshida, Z.-Y. Shi, J. Levinsen, and M. M. Parish, "Few-body states of bosons interacting with a heavy quantum impurity," *Phys. Rev. A*, vol. 98, p. 062 705, 6 Dec. 2018. DOI: 10.1103/PhysRevA.98.062705. [Online]. Available: https://link.aps.org/doi/10.1103/PhysRevA.98.062705.

[87] T. Hartmann, T. A. Schulze, K. K. Voges, P. Gersema, M. W. Gempel, E. Tiemann, A. Zenesini, and S. Ospelkaus, "Feshbach resonances in ^{23}Na + ^{39}K mixtures and refined molecular potentials for the nak molecule," *Phys. Rev. A*, vol. 99, p. 032 711, 3 Mar. 2019. DOI: 10.1103/PhysRevA.99.032711. [Online]. Available: https://link.aps.org/doi/10.1103/PhysRevA.99.032711.

[88] C. Chin and P. S. Julienne, "Radio-frequency transitions on weakly bound ultracold molecules," *Phys. Rev. A*, vol. 71, p. 012 713, 1 Jan. 2005. DOI: 10.1103/PhysRevA.71.012713. [Online]. Available: https://link.aps.org/doi/10.1103/PhysRevA.71.012713.

[89] T. Tscherbul and S. T. Rittenhouse, "Three-body radio-frequency association of efimov trimers," *Physical Review A—Atomic, Molecular, and Optical Physics*, vol. 84, no. 6, p. 062 706, 2011.

[90] D. J. M. Ahmed-Braun, J. van de Kraats, and A. Christianen, *in preparation*.

[91] C. Klempt, T. Henninger, O. Topic, M. Scherer, L. Kattner, E. Tiemann, W. Ertmer, and J. J. Arlt, "Radio-frequency association of heteronuclear feshbach molecules," *Phys. Rev. A*, vol. 78, p. 061 602, 6 Dec. 2008. DOI: 10.1103/PhysRevA.78.061602. [Online]. Available: https://link.aps.org/doi/10.1103/PhysRevA.78.061602.

[92] T. Weber, J. Herbig, M. Mark, H.-C. Nägerl, and R. Grimm, "Three-body recombination at large scattering lengths in an ultracold atomic gas," *Physical Review Letters*, vol. 91, p. 123 201, 12 Sep. 2003, ISSN: 0031-9007. DOI: 10.1103/PhysRevLett.91.123201. [Online]. Available: https://link.aps.org/doi/10.1103/PhysRevLett.91.123201.

[93] L. Wacker, N. Jørgensen, D. Birkmose, N. Winter, M. Mikkelsen, J. Sherson, N. Zinner, and J. Arlt, "Universal three-body physics in ultracold krb mixtures," *Physical Review Letters*, vol. 117, p. 163 201, 16 Oct. 2016, ISSN: 0031-9007. DOI: 10.1103/PhysRevLett.117.163201. [Online]. Available: https://link.aps.org/doi/10.1103/PhysRevLett.117.163201.

[94] T. Lompe, T. B. Ottenstein, F. Serwane, A. N. Wenz, G. Zürn, and S. Jochim, "Radio-frequency association of efimov trimers," *Science*, vol. 330, pp. 940–944, 6006 Nov. 2010, ISSN: 0036-8075. DOI: 10.1126/science.1193148. [Online]. Available: https://www.science.org/doi/10.1126/science.1193148.

[95] O. Machtey, Z. Shotan, N. Gross, and L. Khaykovich, "Association of efimov trimers from a three-atom continuum," *Phys. Rev. Lett.*, vol. 108, p. 210 406, 21 May 2012. DOI: 10.1103/PhysRevLett.108.210406. [Online]. Available: https://link.aps.org/doi/10.1103/PhysRevLett.108.210406.

[96] Y. Yudkin, R. Elbaz, P. Giannakeas, C. H. Greene, and L. Khaykovich, "Coherent superposition of feshbach dimers and efimov trimers," *Phys. Rev. Lett.*, vol. 122, p. 200 402, 20 May 2019. DOI: 10.1103/PhysRevLett.122.200402. [Online]. Available: https://link.aps.org/doi/10.1103/PhysRevLett.122.200402.

[97] Y. Yudkin, R. Elbaz, J. P. D'Incao, P. S. Julienne, and L. Khaykovich, "Reshaped three-body interactions and the observation of an efimov state in the continuum," *Nature Communications*, vol. 15, no. 1, p. 2127, 2024.

[98] J. Ulmanis, S. Häfner, R. Pires, F. Werner, D. S. Petrov, E. D. Kuhnle, and M. Weidemüller, "Universal three-body recombination and efimov resonances in an ultracold li-cs mixture," *Phys. Rev. A*, vol. 93, p. 022 707, 2 Feb. 2016. DOI: 10.1103/PhysRevA.93.022707. [Online]. Available: https://link.aps.org/doi/10.1103/PhysRevA.93.022707.

[99] R. S. Bloom, M. G. Hu, T. D. Cumby, and D. S. Jin, "Tests of universal three-body physics in an ultracold bose-fermi mixture," *Physical Review Letters*, vol. 111, 10 Sep. 2013, ISSN: 00319007. DOI: 10.1103/PhysRevLett.111.105301.

[100] G. Barontini, C. Weber, F. Rabatti, J. Catani, G. Thalhammer, M. Inguscio, and F. Minardi, "Observation of heteronuclear atomic efimov resonances," *Phys. Rev. Lett.*, vol. 103, p. 043 201, 4 Jul. 2009. DOI: 10.1103/PhysRevLett.103.043201. [Online]. Available: https://link.aps.org/doi/10.1103/PhysRevLett.103.043201.

[101] S. E. Pollack, D. Dries, and R. G. Hulet, "Universality in three- and four-body bound states of ultracold atoms," *Science*, vol. 326, no. 5960, pp. 1683–1685, 2009. DOI: 10.1126/science.1182840. eprint: https://www.science.org/doi/pdf/10.1126/science.1182840. [Online]. Available: https://www.science.org/doi/abs/10.1126/science.1182840.

[102] L. Happ, P. Naidon, and E. Hiyama, "Mass ratio dependence of three-body resonance lifetimes in 1d and 3d," *Few-Body Systems*, vol. 65, no. 2, pp. 1–11, 2024.

[103] X.-Y. Chen, M. Duda, A. Schindewolf, R. Bause, I. Bloch, and X.-Y. Luo, "Suppression of unitary three-body loss in a degenerate bose-fermi mixture," *Phys. Rev. Lett.*, vol. 128, p. 153 401, 15 Apr. 2022. DOI: 10.1103/PhysRevLett.128.153401. [Online]. Available: https://link.aps.org/doi/10.1103/PhysRevLett.128.153401.

[104] M. Duda, X.-Y. Chen, A. Schindewolf, R. Bause, J. von Milczewski, R. Schmidt, I. Bloch, and X.-Y. Luo, "Transition from a polaronic condensate to a degenerate fermi gas of heteronuclear molecules," *Nature Physics*, vol. 19, no. 5, pp. 720–725, 2023.

[105] S. M. Yoshida, S. Endo, J. Levinsen, and M. M. Parish, "Universality of an impurity in a bose-einstein condensate," *Physical Review X*, vol. 8, no. 1, p. 011 024, 2018.

[106] J. Levinsen, L. A. P. Ardila, S. M. Yoshida, and M. M. Parish, "Quantum behavior of a heavy impurity strongly coupled to a bose gas," *Phys. Rev. Lett.*, vol. 127, p. 033 401, 3 Jul. 2021. DOI: 10.1103/PhysRevLett.127.033401. [Online]. Available: https://link.aps.org/doi/10.1103/PhysRevLett.127.033401.

[107] A. Christianen, J. I. Cirac, and R. Schmidt, "Phase diagram for strong-coupling bose polarons," *SciPost Physics*, vol. 16, no. 3, p. 067, 2024.

[108] Y. Levinson and E. Rashba, "Electron-phonon and exciton-phonon bound states," *Reports on Progress in Physics*, vol. 36, no. 12, p. 1499, 1973.

[109] A. Christianen, "Chemistry in a quantum medium," Ph.D. dissertation, Technische Universität München, 2023, p. 188. [Online]. Available: https://mediatum.ub.tum.de/1720019.

[110] C. Chin and P. S. Julienne, "Radio-frequency transitions on weakly bound ultracold molecules," *Physical Review A*, vol. 71, p. 012 713, 1 Jan. 2005, ISSN: 1050-2947. DOI: 10.1103/PhysRevA.71.012713. [Online]. Available: https://link.aps.org/doi/10.1103/PhysRevA.71.012713.

[111] J. Levinsen, M. M. Parish, and G. M. Bruun, "Impurity in a bose-einstein condensate and the efimov effect," *Physical Review Letters*, vol. 115, p. 125 302, 12 Sep. 2015, ISSN: 0031-9007. DOI: 10.1103/PhysRevLett.115.125302. [Online]. Available: https://link.aps.org/doi/10.1103/PhysRevLett.115.125302.

[112] T. Rentrop, A. Trautmann, F. Olivares, F. Jendrzejewski, A. Komnik, and M. Oberthaler, "Observation of the phononic lamb shift with a synthetic vacuum," *Physical Review X*, vol. 6, p. 041 041, 4 Nov. 2016, ISSN: 2160-3308. DOI: 10.1103/PhysRevX.6.041041. [Online]. Available: https://link.aps.org/doi/10.1103/PhysRevX.6.041041.

[113] A. M. Morgen, S. S. Balling, K. K. Nielsen, T. Pohl, G. M. Bruun, and J. J. Arlt, "Quantum beat spectroscopy of repulsive bose polarons," *ArXiV preprint*, Oct. 2023. [Online]. Available: http://arxiv.org/abs/2310.18183.

[114] J. Etrych, G. Martirosyan, A. Cao, C. J. Ho, Z. Hadzibabic, and C. Eigen, "Universal quantum dynamics of bose polarons," *ArXiv preprint*, Feb. 2024. [Online]. Available: http://arxiv.org/abs/2402.14816.

[115] M.-G. Hu, M. J. V. de Graaff, D. Kedar, J. P. Corson, E. A. Cornell, and D. S. Jin, "Bose polarons in the strongly interacting regime," *Physical Review Letters*, vol. 117, p. 055 301, 5 Jul. 2016, ISSN: 0031-9007. DOI: 10.1103/PhysRevLett.117.055301. [Online]. Available: https://link.aps.org/doi/10.1103/PhysRevLett.117.055301.

[116] I. R. Solá, V. S. Malinovsky, B. Y. Chang, J. Santamaria, and K. Bergmann, "Coherent population transfer in three-level Λ systems by chirped laser pulses: Minimization of the intermediate-level population," *Phys. Rev. A*, vol. 59, pp. 4494–4501, 6 Jun. 1999. DOI: 10.1103/PhysRevA.59.4494. [Online]. Available: https://link.aps.org/doi/10.1103/PhysRevA.59.4494.

[117] N.-E. Guenther, P. Massignan, M. Lewenstein, and G. M. Bruun, "Bose Polarons at Finite Temperature and Strong Coupling," *Phys. Rev. Lett.*, vol. 120, p. 050 405, 5 Feb. 2018. DOI: 10.1103/PhysRevLett.120.050405. [Online]. Available: https://link.aps.org/doi/10.1103/PhysRevLett.120.050405.

[118] B. Field, J. Levinsen, and M. M. Parish, "Fate of the Bose polaron at finite temperature," *Phys. Rev. A*, vol. 101, p. 013 623, 1 Jan. 2020. DOI: 10.1103/PhysRevA.101.013623. [Online]. Available: https://link.aps.org/doi/10.1103/PhysRevA.101.013623.

[119] D. Dzsotjan, R. Schmidt, and M. Fleischhauer, "Dynamical Variational Approach to Bose Polarons at Finite Temperatures," *Phys. Rev. Lett.*, vol. 124, p. 223 401, 22 Jun. 2020. DOI: 10.1103/PhysRevLett.124.223401. [Online]. Available: https://link.aps.org/doi/10.1103/PhysRevLett.124.223401.

[120] G. Pascual and J. Boronat, "Quasiparticle Nature of the Bose Polaron at Finite Temperature," *Phys. Rev. Lett.*, vol. 127, p. 205 301, 20 Nov. 2021. DOI: 10.1103/PhysRevLett.127.205301. [Online]. Available: https://link.aps.org/doi/10.1103/PhysRevLett.127.205301.

[121] N. Navon, R. P. Smith, and Z. Hadzibabic, "Quantum gases in optical boxes," *Nature Physics*, vol. 17, no. 12, pp. 1334–1341, 2021. DOI: 10.1038/s41567-021-01403-z.

[122] L. De Marco, G. Valtolina, K. Matsuda, W. G. Tobias, J. P. Covey, and J. Ye, "A degenerate fermi gas of polar molecules," *Science*, vol. 363, no. 6429, pp. 853–856, 2019. DOI: 10.1038/s41567-021-01403-z.

[123] Z. Vendeiro, "Raman cooling to high phase space density," Ph.D. dissertation, MIT, 2021.

[124] P. T. Starkey, "A software framework for control and automation of precisely timed experiments," Ph.D. dissertation, Monash University, 2019.

[125] A. Keshet and W. Ketterle, "A distributed, graphical user interface based, computer control system for atomic physics experiments," *Review of Scientific Instruments*, vol. 84, no. 1, p. 015 105, Jan. 2013, ISSN: 0034-6748. DOI: 10.1063/1.4773536. eprint: https://pubs.aip.org/aip/rsi/article-pdf/doi/10.1063/1.4773536/14701602/015105_1_online.pdf. [Online]. Available: https://doi.org/10.1063/1.4773536.

[126] W. Lunden, "Development of a new dy quantum gas experiment," Ph.D. dissertation, MIT, 2020.

[127] A. Chuang. "Autogenerate labscript code snippets from cicero .seq files," GitHub. (Aug. 2024), [Online]. Available: https://github.com/achuang2718/seq2py (visited on 08/05/2024).

[128] A. Chuang. "Translate cicero .seq binaries into human readable .yaml," GitHub. (Aug. 2024), [Online]. Available: https://github.com/achuang2718/ciceroSeq2Yaml (visited on 08/05/2024).

[129] Z. Vendeiro, J. Ramette, A. Rudelis, M. Chong, J. Sinclair, L. Stewart, A. Urvoy, and V. Vuleti ć, "Machine-learning-accelerated bose-einstein condensation," *Phys. Rev. Res.*, vol. 4, p. 043 216, 4 Dec. 2022. DOI: 10.1103/PhysRevResearch.4.043216. [Online]. Available: https://link.aps.org/doi/10.1103/PhysRevResearch.4.043216.

[130] B. Zhu, B. Gadway, M. Foss-Feig, *et al.*, "Suppressing the loss of ultracold molecules via the continuous quantum zeno effect," *Physical Review Letters*, vol. 112, p. 070 404, 7 Feb. 2014, ISSN: 0031-9007. DOI: 10.1103/PhysRevLett.112.070404. [Online]. Available: https://link.aps.org/doi/10.1103/PhysRevLett.112.070404.

[131] M. Brune, F. Schmidt-Kaler, A. Maali, J. Dreyer, E. Hagley, J. M. Raimond, and S. Haroche, "Quantum rabi oscillation: A direct test of field quantization in a cavity," *Phys. Rev. Lett.*, vol. 76, pp. 1800–1803, 11 Mar. 1996. DOI: 10.1103/PhysRevLett.76.1800. [Online]. Available: https://link.aps.org/doi/10.1103/PhysRevLett.76.1800.

[132] W. G. Tobias, "Degenerate polar molecules with controlled interactions and reactivity," Ph.D. dissertation, University of Colorado, Boulder, 2019.

[133] A. Christianen, M. W. Zwierlein, G. C. Groenenboom, and T. Karman, "Photoinduced two-body loss of ultracold molecules," *Phys. Rev. Lett.*, vol. 123, p. 123 402, 12 Sep. 2019. DOI: 10.1103/PhysRevLett.123.123402. [Online]. Available: https://link.aps.org/doi/10.1103/PhysRevLett.123.123402.

[134] K. Matsuda, L. D. Marco, J.-R. Li, W. G. Tobias, G. Valtolina, G. Quéméner, and J. Ye, "Resonant collisional shielding of reactive molecules using electric fields," *Science*, vol. 370, pp. 1324–1327, 6522 Dec. 2020, ISSN: 0036-8075. DOI: 10.1126/science.abe7370. [Online]. Available: https://www.science.org/doi/10.1126/science.abe7370.

[135] J.-R. Li, W. G. Tobias, K. Matsuda, *et al.*, "Tuning of dipolar interactions and evaporative cooling in a three-dimensional molecular quantum gas," *Nature Physics*, vol. 17, pp. 1144–1148, 10 Oct. 2021, ISSN: 1745-2473. DOI: 10.1038/s41567-021-01329-6. [Online]. Available: https://www.nature.com/articles/s41567-021-01329-6.

[136] L. Anderegg, S. Burchesky, Y. Bao, S. S. Yu, T. Karman, E. Chae, K.-K. Ni, W. Ketterle, and J. M. Doyle, "Observation of microwave shielding of ultracold molecules," *Science*, vol. 373, no. 6556, pp. 779–782, 2021. DOI: 10.1126/science.abg9502. eprint: https://www.science.org/doi/pdf/10.1126/science.abg9502. [Online]. Available: https://www.science.org/doi/abs/10.1126/science.abg9502.

[137] A. Schindewolf, R. Bause, X.-Y. Chen, M. Duda, T. Karman, I. Bloch, and X.-Y. Luo, "Evaporation of microwave-shielded polar molecules to quantum degeneracy," *Nature*, vol. 607, pp. 677–681, 7920 Jul. 2022, ISSN: 0028-0836. DOI: 10.1038/s41586-022-04900-0. [Online]. Available: https://www.nature.com/articles/s41586-022-04900-0.

[138] N. Bigagli, C. Warner, W. Yuan, S. Zhang, I. Stevenson, T. Karman, and S. Will, "Collisionally stable gas of bosonic dipolar ground-state molecules," *Nature Physics*, vol. 19, pp. 1579–1584, 11 Nov. 2023, ISSN: 17452481. DOI: 10.1038/s41567-023-02200-6.

[139] N. Bigagli, W. Yuan, S. Zhang, B. Bulatovic, T. Karman, I. Stevenson, and S. Will, "Observation of bose–einstein condensation of dipolar molecules," *Nature*, vol. 631, pp. 289–293, 8020 Jul. 2024, ISSN: 0028-0836. DOI: 10.1038/s41586-024-07492-z. [Online]. Available: https://www.nature.com/articles/s41586-024-07492-z.

[140] J. J. Park, H. Son, Y.-K. Lu, T. Karman, M. Gronowski, M. Tomza, A. O. Jamison, and W. Ketterle, "Spectrum of feshbach resonances in NaLi + Na collisions," *Phys. Rev. X*, vol. 13, p. 031 018, 3 Aug. 2023. DOI: 10.1103/PhysRevX.13.031018. [Online]. Available: https://link.aps.org/doi/10.1103/PhysRevX.13.031018.

[141] J. J. Park, Y. K. Lu, A. O. Jamison, T. V. Tscherbul, and W. Ketterle, "A feshbach resonance in collisions between triplet ground-state molecules," *Nature*, vol. 614, pp. 54–58, 7946 Feb. 2023, ISSN: 14764687. DOI: 10.1038/s41586-022-05635-8.

[142] X.-Y. Chen, S. Biswas, S. Eppelt, A. Schindewolf, F. Deng, T. Shi, S. Yi, T. A. Hilker, I. Bloch, and X.-Y. Luo, "Ultracold field-linked tetratomic molecules," *Nature*, vol. 626, pp. 283–287, 7998 Feb. 2024, ISSN: 0028-0836. DOI: 10.1038/s41586-023-06986-6. [Online]. Available: https://www.nature.com/articles/s41586-023-06986-6.

[143] H. Schreiber and J. H. Bruning, *Optical Shop Testing, Third Edition. Chapter 14, Phase Shifting Interferometry*. Wiley, 2006.

[144] R. Tkach and A. Chraplyvy, "Regimes of feedback effects in 1.5-µm distributed feedback lasers," *Journal of Lightwave Technology*, vol. 4, pp. 1655–1661, 11 1986, ISSN: 0733-8724. DOI: 10.1109/JLT.1986.1074666. [Online]. Available: http://ieeexplore.ieee.org/document/1074666/.

[145] C. E. Wieman and L. Hollberg, "Using diode lasers for atomic physics," *Review of Scientific Instruments*, vol. 62, pp. 1–20, 1 Jan. 1991, ISSN: 0034-6748. DOI: 10.1063/1.1142305. [Online]. Available: https://pubs.aip.org/rsi/article/62/1/1/324556/Using-diode-lasers-for-atomic-physicsDiode-lasers.

[146] Q. Lin, M. A. V. Camp, H. Zhang, B. Jelenković, and V. Vuletić, "Long-external-cavity distributed bragg reflector laser with subkilohertz intrinsic linewidth," *Optics Letters*, vol. 37, p. 1989, 11 Jun. 2012, ISSN: 0146-9592. DOI: 10.1364/OL.37.001989. [Online]. Available: https://opg.optica.org/abstract.cfm?URI=ol-37-11-1989.

[147] *Principle of operation of oewaves laser noise analyzer*, OEWaves. [Online]. Available: https://www.oewaves.com/_files/ugd/d39cf0_40b713a3e11c4c6c8d919ace3696572d.pdf.

[148] G. D. Domenico, S. Schilt, and P. Thomann, "Simple approach to the relation between laser frequency noise and laser line shape," *Applied Optics*, vol. 49, p. 4801, 25 Sep. 2010, ISSN: 0003-6935. DOI: 10.1364/AO.49.004801. [Online]. Available: https://opg.optica.org/abstract.cfm?URI=ao-49-25-4801.

[149] G. Pandian and S. Dilwali, "On the thermal fm response of a semiconductor laser diode," *IEEE Photonics Technology Letters*, vol. 4, no. 2, pp. 130–133, 1992. DOI: 10.1109/68.122338.

[150] L. Li, W. Huie, N. Chen, B. DeMarco, and J. P. Covey, "Active cancellation of servo-induced noise on stabilized lasers via feedforward," *Phys. Rev. Appl.*, vol. 18, p. 064 005, 6 Dec. 2022. DOI: 10.1103/PhysRevApplied.18.064005. [Online]. Available: https://link.aps.org/doi/10.1103/PhysRevApplied.18.064005.

[151] R. Slavík, G. Marra, E. N. Fokoua, N. Baddela, N. V. Wheeler, M. Petrovich, F. Poletti, and D. J. Richardson, "Ultralow thermal sensitivity of phase and propagation delay in hollow core optical fibres," *Scientific Reports*, vol. 5, p. 15 447, 1 Oct. 2015, ISSN: 2045-2322. DOI: 10.1038/srep15447. [Online]. Available: https://www.nature.com/articles/srep15447.

[152] M. Yamoah, B. Braverman, E. Pedrozo-Peñafiel, A. Kawasaki, B. Zlatković, and V. Vuletić, "Robust khz-linewidth distributed bragg reflector laser with optoelectronic feedback," *Opt. Express*, vol. 27, no. 26, pp. 37 714–37 720, Dec. 2019. DOI: 10.1364/OE.27.037714. [Online]. Available: https://opg.optica.org/oe/abstract.cfm?URI=oe-27-26-37714.

[153] C. Wilson, "Geometric squeezing of a degenerate fermi gas," Ph.D. dissertation, MIT, 2023.